DRUG-FREE MACROMOLECULAR THERAPEUTICS

FOR TREATMENT OF B-CELL MALIGNANCIES

by

Te-Wei Chu

A dissertation submitted to the faculty of
The University of Utah
in partial fulfillment of the requirements for the degree of

Doctor of Philosophy

Department of Pharmaceutics and Pharmaceutical Chemistry

The University of Utah

August 2015

Copyright © Te-Wei Chu 2015

All Rights Reserved

The University of Utah Graduate School

STATEMENT OF DISSERTATION APPROVAL

The dissertation of **Te-Wei Chu**

has been approved by the following supervisory committee members:

Jindřich Kopeček	, Chair	**May 26, 2015** Date Approved
David W. Grainger	, Member	**May 26, 2015** Date Approved
Carol Lim	, Member	**May 26, 2015** Date Approved
Jiyuan Yang	, Member	**May 26, 2015** Date Approved
Glenn D. Prestwich	, Member	**May 11, 2015** Date Approved

and by **David W. Grainger** , Chair of

the Department of **Pharmaceutics and Pharmaceutical Chemistry**

and by David B. Kieda, Dean of The Graduate School.

ABSTRACT

Hybrid nanomaterials composed of synthetic and biological building blocks possess high potential for the design of nanomedicines. We propose a new therapeutic approach that mimics the mechanism of immune effector cells to crosslink surface receptors of target cells and induce apoptosis. The receptor crosslinking is mediated by biorecognition of high-fidelity natural binding motifs (antibody fragments or oligonucleotides) that are grafted to the side chains of synthetic polymers. This approach features the absence of low-molecular-weight cytotoxic compounds. Thus, we name it "drug-free macromolecular therapeutics."

This dissertation describes the development and preclinical evaluation of two drug-free macromolecular therapeutic platforms. The designed therapeutics were tested against B-cell malignancies that highly express the surface antigen CD20.

In the first design, a multivalent conjugate comprising high-molecular-weight, linear copolymer of *N*-(2-hydroxypropyl)methacrylamide (HPMA) grafted with multiple Fab' fragments of an anti-CD20 antibody was synthesized. Exposure of human non-Hodgkin lymphoma (NHL) Raji B-cells to the multivalent construct resulted in crosslinking of CD20 receptors and commencement of apoptosis.

In the second design, two hybrid conjugates were produced: (1) an anti-CD20 Fab' attached to an oligonucleotide1, and (2) a linear HPMA copolymer grafted with multiple complementary oligonucleotide2. We showed that the two conjugates self-

assembled *via* oligonucleotide hybridization at the surface of $CD20^+$ B-cells, which crosslinked CD20 antigens and initiated apoptosis. When tested in a mouse xenograft model, the two conjugates, either administered consecutively or as a premixture, eradicated Raji cells and produced long-term survivors.

The consecutive administration approach was chosen for further studies where a two-step pretargeting strategy was employed. We showed that the time lag between administering the two conjugates can be optimized based on pharmacokinetics and biodistribution of the Fab'-oligonucleotide1 conjugate. Using the optimized treatment regimen, the designed nanomedicine achieved superior anti-lymphoma efficacy to rituximab, a clinically used drug for NHL. We also evaluated the nanomedicine in patient mantle cell lymphoma and chronic lymphocytic leukemia cells. The treatment demonstrated potent apoptosis-inducing activity.

In summary, we have developed novel nanotherapeutics that may constitute potent treatments for NHL and other B-cell malignancies. The verified concept can be applied to crosslink receptors other than CD20 and potentially treat different diseases.

Dedicated to the little stranger who will soon enter my life.

This dissertation might not exist if you come sooner…

TABLE OF CONTENTS

LIST OF FIGURES

LIST OF TABLES

LIST OF ABBREVIATIONS

ADCC	antibody-dependent cellular cytotoxicity
APC	allophycocyanin
APMA	*N*-(3-aminopropyl)methacrylamide hydrochloride
BCA	bicinchoninic acid
BM	bone marrow
BSA	bovine serum albumin
CD	circular dichroism
CDC	complement-dependent cytotoxicity
CLL	chronic lymphocytic leukemia
CPDB	4-cyanopentanoic acid dithiobenzoate
CTA	chain transfer agent
DLS	dynamic light scattering
EPR	enhanced permeability and retention
Fab	fragment antigen-binding
Fc	fragment crystallizable
FcR	Fc receptor
FMT	fluorescence molecular tomography
GAM	goat antimouse
GFP	green fluorescence protein
H&E	hematoxylin and eosin
HPMA	*N*-(2-hydroxypropyl)methacrylamide
IACUC	Institutional Animal Care and Use Committee
mAb	monoclonal antibody
MA-FITC	*N*-methacryloylaminopropyl fluorescein thiourea
MA-GG-TT	*N*-methacryloylglycylglycine thiazolidine-2-thione

MCL	mantle cell lymphoma
MicroCT	microcomputed tomography
Mn	number average molecular weight
MORF	phosphorodiamidate morpholino
MPA	3-mercaptopropionic acid
MRI	magnetic resonance imaging
MW	molecular weight
Mw	weight average molecular weight
NHL	non-Hodgkin lymphoma
OD	optical density
OPA	o-phthalic dicarboxaldehyde
PBS	phosphate buffered saline
PE	R-phycoerythrin
PI	propidium iodide
PK	Pharmacokinetic(s)
PML	progressive multifocal leukoencephalopathy
PNA	peptide nucleic acid
RAFT	reversible addition-fragmentation chain transfer
RHO	rhodamine
scFv	single-chain variable fragment
SD	standard deviation
SEC	size-exclusion chromatography
SMCC	succinimidyl-4-(*N*-maleimidomethyl)cyclohexane-1-carboxylate
TCEP	tris(2-carboxyethyl)phosphine
TEA	triethylamine
Tm	melting temperature
TNFα	tumor necrosis factor-α
TUNEL	terminal deoxynucleotide mediated-dUTP nick-end labeling

ACKNOWLEDGMENTS

I would like to express my deepest gratitude to my advisor, Dr. Jindřich Kopeček. I have learned immensely from your continued guidance, support and encouragement during this Ph.D. research. You are a true mentor as well as an inspiration to me, not only in science but also in life. I would like to thank my dissertation committee members, Drs. David Grainger, Carol Lim, Jiyuan Yang, and Glenn Prestwich. Without your exceptional insights, this dissertation would not be completed. I would also like to thank Dr. Paul Shami for providing clinical perspectives on my research. The presented work was supported by NIH grant GM95606 from the National Institute of General Medical Sciences and the University of Utah Research Foundation.

I am grateful to my labmates, colleagues and friends at the University of Utah. My sincere appreciation is extended to the past and present members of the Kopeček Lab, especially Jane, Rui, Pavla, Moni, Zoe, Stew, Jon, Chris, Joy, and Dalynn. Thank you for making the lab such a pleasant place. I am very fortunate to have your help and company.

My Utah experience has been a challenging and exciting journey. I am extremely thankful to those who have helped and accompanied me to achieve this degree and will forever treasure this invaluable, once-in-a-lifetime opportunity. Finally, my greatest thanks go to my family – my parents, and my wife, Yu-Chan, for your love, patience and support, and for being such a wonderful companion and my best friend in life. Without you, this degree would never have been possible.

CHAPTER 1

INTRODUCTION[1]

Macromolecular therapeutics, also referred to as polymeric nanomedicines, are a diverse group of drugs characterized by their large molecular weight (MW), including polymer-drug conjugates, polymeric micelles, polymer-modified liposomes, *etc*. The advantages of macromolecular therapeutics when compared to low-molecular-weight compounds are reviewed elsewhere.[1–3] In particular, water-soluble polymeric drugs (MW > 40 kDa) attain prolonged plasma half-lives and achieve tumoritropic accumulation due to the enhanced permeability and retention (EPR) effect.[4,5] Conventional polymeric nanomedicines utilize polymers as delivery vehicles to carry anticancer therapeutic agents. Many of these approaches are under clinical development.[6–12] Increasingly the role of nanomedicine is not only to deliver a given drug to diseased tissues efficiently but also to trigger or improve therapeutic effects through innate biological responses.[13,14] The design of macromolecular therapeutics has extended towards a unique paradigm where biomimetic strategies are employed to incite or control specific cellular activities.[15–17] For instance, receptor coupling (or clustering) can be used to sensitize diseased tissues to a therapeutic agent.[18–21] In this dissertation, we describe a novel paradigm in the

[1]This chapter is adapted from the following publication: T.-W. Chu and J. Kopeček. Drug-free macromolecular therapeutics – a new paradigm in polymeric nanomedicines. *Biomater Sci.* 2015; 3(7): 908–922. Adapted by permission of The Royal Society of Chemistry.

nanomedicine research area – drug-free macromolecular therapeutics. This approach was firstly proposed by our laboratory in 2010.[21] The basic idea is to induce apoptosis by crosslinking of cell-surface noninternalizing receptors mediated by the biorecognition of high-fidelity natural binding motifs, such as antiparallel coiled-coil peptides or complementary oligonucleotides. The general design concept of drug-free macromolecular therapeutics is shown in Figure 1.1. An important feature of these designs is the absence of low-molecular-weight cytotoxic compounds (thus named "drug-free"). This chapter introduces recent developments in this exciting new area, which mainly includes research performed in our laboratory using B-cell malignancies as a disease model and the CD20 receptor as a pharmacological target, as well as relevant approaches reported by other researchers.

1.1 B-Cell Lymphoma and CD20

Non-Hodgkin's lymphoma (NHL) is a prevalent cancer with over a half-million individuals having a history in the United States and an estimated 70,800 new cases diagnosed in 2014.[22] Over the past 3 decades, the incidence of NHL has continuously increased (doubled since 1980). NHL has a high mortality rate; from 2006 to 2010, there were 18,990 deaths for every 100,000 patients in the U.S.[22] The disease is comprised of a diverse and heterogeneous group of lymphatic malignancies, which makes the treatment challenging. About 85% of NHLs are cancers originating from B-cells; the remaining diseases are mostly of T-cell origin.[23] This dissertation focuses mainly on designs and developments of novel therapeutics against B-cell lymphomas (or B-NHLs), including Burkitt's, diffuse large B-cell, follicular, immunoblastic large cell, precursor B-

lymphoblastic, and mantle cell lymphomas. These malignancies are generally classified as either indolent or aggressive, which then dictates the type of therapy the patient may receive.[23,24] Besides conventional chemotherapy and radiotherapy, which are usually accompanied by severe adverse reactions, monoclonal antibodies (mAbs) targeted to the B-cell surface antigen CD20 have become common treatments.[25] Such "immunotherapies" have revolutionized the field. The current standard of B-NHL treatment is rituximab (the most commonly used anti-CD20 mAb) in combination with chemotherapy.[26,27] However, large populations of patients exist who do not respond or develop resistance to these therapies. For example, the overall response rates for the treatment of relapsed/refractory low-grade or follicular NHL typically ranged from 40 to 50% (complete response 6, 3, 17, 3, and 14%; overall response 48, 46, 47, 39, and 43% in five different clinical trials).[28] The nonresponsiveness and/or resistance have been attributed to the inability of immune effector cells (*e.g.*, macrophages, natural killer cells) to hypercrosslink ligated mAbs,[29,30] and Fc receptor (FcR)-mediated endocytosis[31] or "trogocytosis"[32] of CD20 antigens. These clinical obstacles create the need for new, improved therapeutic strategies.

CD20 is a 35–37 kDa integral membrane protein highly expressed on more than 95% of B-cell lymphomas.[33,34] Free CD20 antigen is not present in serum, and there is no known natural ligand of CD20. When bound by antibodies, CD20 has a very low intracellular internalization rate;[35,36] it is often considered a noninternalizing receptor. Studies suggest that CD20 functions as a store-operated calcium channel and a cell cycle regulator.[37–39] It is one of the most reliable biomarkers of B-lymphocytes, thus providing an ideal target for treatment of B-NHL.[23,24] CD20 is also expressed on normal B-cells;

however, it is not expressed on stem cells or progenitor cells and mature or activated plasma cells.[33] Therefore, the "B-cell depletion" therapeutic approach is considered safe; normal numbers of B-cells can be restored after treatment.[25–27] The therapeutic efficacy of anti-CD20 mAbs is ascribed to three cellular events: antibody-dependent cellular cytotoxicity (ADCC), complement-dependent cytotoxicity (CDC), and CD20-mediated apoptosis.[40–42] All of these mechanisms require immune effector cells to function.[41] In contrast, drug-free macromolecular therapeutics trigger direct and specific apoptosis of B-cell lymphomas without the help of effector cells. This is achieved by the design of synthetic effectors that reproduce the function of immune effector cells. The advantages of such an approach will be further discussed in this dissertation.

1.2 Receptor Crosslinking and Apoptosis

Cell receptor clustering (crosslinking) is a natural process and driving force for numerous biological responses. For instance, the following cellular events have been reported to result from receptor clustering: hormone uptake,[43] cell adhesion,[44] cell activation[45] and apoptosis.[42,46] In particular, crosslinking of the surface antigen CD20 induces apoptosis of B-cells. Research has shown that when CD20-bound antibodies are hypercrosslinked by FcR-expressing immune effector cells (or polyclonal secondary antibodies), CD20 receptors tend to cluster as dimers or tetramers, redistribute and become localized into lipid rafts.[47] Such events mediate the interaction between clustered CD20 and Src-family kinases (which are also located in lipid rafts), and trigger apoptotic signaling.[48,49] Without the hypercrosslinking, apoptosis initiated by ligated mAbs is limited.[50–52] These mechanistic studies warranted various earlier designs of multivalent

mAb constructs. For example, Ghetie *et al.* synthesized a homodimer of rituximab by using a heterobifunctional crosslinker and showed that the mAb dimer potentiated apoptosis in human B-cell lymphomas, which synergized with a chemotherapeutic agent and an immunotoxin.[51] Rossi *et al.* produced a hexavalent anti-CD20 antibody by covalently assembling 6 Fab' to 1 Fc.[53] Anti-lymphoma efficacy of this hexavalent construct in mouse xenografts was comparable to that of the monovalent mAb, but it was independent of effector mechanisms such as CDC. Stein *et al.* used a monomeric Ab that lacks effector cell functions hypercrosslinked by a secondary Ab to specifically facilitate apoptosis.[54] These previous research studies showed that approaches aimed at direct apoptosis induction *via* cell surface receptor clustering are becoming attractive.

1.3 Origin of Drug-Free Macromolecular Therapeutics

The initial design of drug-free macromolecular therapeutics was inspired by our previous work on hybrid hydrogels self-assembled from synthetic polymers and coiled-coil protein domains. We developed "smart" biomaterials composed of *N*-(2-hydroxypropyl)methacrylamide (HPMA) copolymers grafted with biorecognition domains.[55–58] The biorecognition of complementary grafts resulted in physical crosslinking of polymer chains and formation of 3D networks (hydrogels). In particular, a pair of oppositely charged pentaheptad peptides (CCE and CCK) that form antiparallel coiled-coil heterodimers were designed (Figure 1.2). Multiple copies of CCE or CCK were grafted to the HPMA polymer (P) backbones to produce P-$(CCE)_x$ and P-$(CCK)_y$, respectively. Equimolar mixtures of P-$(CCE)_x$ and P-$(CCK)_y$ solutions self-assembled into hydrogels where the coiled-coil peptides served as macromolecular physical

crosslinkers.[58,59] The excellent CCE/CCK biorecognition was also employed by Lv *et al.* for the development of tandem modular protein-based hydrogels.[60] On the other hand, our laboratory pioneered the design of HPMA copolymers as anticancer drug carriers,[61,62] which led to the development of PK1 (HPMA copolymer–doxorubicin conjugate), the first polymeric drug that entered clinical trials.[63] HPMA copolymers are water-soluble, biocompatible, and long circulating in the bloodstream.[3,64] They have flexible (random-coil) conformation in aqueous solutions; thus, targeting moieties or biorecognition motifs that are grafted to the side chains can be effectively presented.[65] Based on these studies[58,59] and the above-mentioned mechanism of receptor clustering mediated apoptosis, we hypothesized that the unique biorecognition of the CCE/CCK peptide motifs could be used to crosslink not only polymer chains but also cell surface receptors (*e.g.*, CD20) to induce apoptosis of target cells (*e.g.*, B-cell). Such an application of hybrid materials to biological systems to mediate specific cellular events (*i.e.*, apoptosis) provides a bridge between the designs of functional biomaterials and novel nanomedicines.

Due to the specific intermolecular interactions and the high degree of structural control based on primary sequences, coiled-coil peptides have become attractive as a building block for nanomedicine design.[66–68] Our laboratory pioneered the development of drug-free macromolecular therapeutics, which employed the coiled-coil forming peptides CCE and CCK as the biorecognition motif.[21] Two macromolecular conjugates were synthesized: (1) CCE tethered to a Fab' fragment of an anti-CD20 mAb (Fab'-CCE); (2) an HPMA copolymer grafted with multiple CCK peptides (P-$(CCK)_y$). Exposure of a $CD20^+$ human B-NHL cell line (Raji) to the Fab'-CCE conjugate first decorated the cell

surfaces with CCE. Further treatment of the decorated cells with P-$(CCK)_y$ resulted in formation of antiparallel coiled-coils at cell surfaces, which crosslinked CD20 receptors and induced apoptosis. This concept has been successfully proven by Wu *et al*.[21,69] *In vitro* apoptosis induction of Raji B-cells was achieved after co-treatment with Fab'-CCE and P-$(CCK)_y$, either consecutively or as a premixture.[21] *In vivo* anticancer efficacy was evaluated in mice bearing systemically disseminated B-cell NHL.[69] Both the consecutive and the premixed treatments were able to eradicate lymphoma cells in the blood and in the bone marrow, which produced long-term survivors.

The biorecognition of the coiled-coil forming oligopeptides, CCE and CCK, in the "drug-free" system functioned well to induce cell apoptosis. However, to achieve a strong anticancer effect (produce tumor-free long-term survivors), we used a 1:25 molar ratio of CCE equivalent (in Fab'-CCE) to CCK equivalent (in P-$(CCK)_9$).[69] This is because the individual peptide sequences (CCE and CCK) do not have a pronounced secondary structure at pH 7 and are in a random coil conformation.[58] Binding of oligopeptides to macromolecules increases their secondary structure only slightly.[58,70] Consequently, Fab'-CCE and P-$(CCK)_y$ interact first *via* hydrophobic and electrostatic interactions, and then the oligopeptides fold into a strong antiparallel coiled-coil heterodimer. Such relatively complex binding pattern likely results in inadequate interaction of polymer conjugates with Fab' conjugates when administered at the 1:1 molar ratio condition. Therefore, in order to design improved therapeutic systems, it is essential to identify a biorecognition pair that possess a more direct and efficient binding pattern. Oligonucleotide hybridization was chosen for the further studies.

1.4 Nucleic Acid Hybridization and Morpholino Oligonucleotide

Nucleic acid hybridization is a crucial biorecognition event in life. A DNA double helix is composed of Watson-Crick base paring, *i.e.*, hydrogen bonding of A/T and C/G, between two single-stranded polynucleotides with complementary sequences. The conformation is further stabilized by base stacking, *i.e.*, π-π interaction of neighboring bases on the same strand. Such a self-recognition property plays the central role for coding, storing and transferring of genetic information; it possesses a high fidelity feature. Since early 1980s, DNA has been used as building blocks for biomaterials design,[71,72] and more recently, functional nanostructures for drug delivery.[73,74] In particular, hybrid materials comprising oligonucleotides and synthetic polymers can be utilized to fabricate nanoconstructs with precise geometry and versatile functionality.[75–77]

Over the years, a variety of artificial oligonucleotides with chemically modified backbones have been synthesized.[78] These nonphosphodiester backbones are nuclease resistant and stable in the body; thus, they are suitable for biopharmaceutical applications. We decided to pursue phosphorodiamidate morpholino (MORF) oligomers as the biorecognition motifs for the second-generation "drug-free" therapeutic design. The MORF oligos are charge neutral, resulting in significantly stronger binding than natural DNA and RNA.[79] Hybridization of MORF pairs has well-defined binding specificity, which prevents potential off-target effects.[80,81] In addition, MORF oligos have good aqueous solubility and favorable pharmacokinetics.[82,83] Their base sequence can be designed to achieve optimal binding efficiency and minimal off-targets with human and murine mRNA, and to prevent self-complementarity.[79]

1.5 References

1. K. Greish, J. Fang, T. Inutsuka, A. Nagamitsu and P. H. Maeda, Macromolecular therapeutics, *Clin. Pharmacokinet.*, 2003, **42**, 1089–1105.

2. J. Kopeček, The potential of water-soluble polymeric carriers in targeted and site-specific drug delivery, *J. Control. Release*, 1990, **11**, 279–290.

3. J. Yang and J. Kopeček, Macromolecular therapeutics, *J. Control. Release*, 2014, **190**, 288–303.

4. Y. Matsumura and H. Maeda, A new concept for macromolecular therapeutics in cancer chemotherapy: mechanism of tumoritropic accumulation of proteins and the antitumor agent SMANCS, *Cancer Res.*, 1986, **46**, 6387–6392.

5. J. Kopeček, Polymer-drug conjugates: origins, progress to date and future directions, *Adv. Drug Deliv. Rev.*, 2013, **65**, 49–59.

6. L. W. Seymour, *et al.*, Phase II studies of polymer-doxorubicin (PK1, FCE28068) in the treatment of breast, lung and colorectal cancer, *Int. J. Oncol.*, 2009, **34**, 1629–1636.

7. G. Pasut and F. M. Veronese, PEG conjugates in clinical development or use as anticancer agents: an overview, *Adv. Drug Deliv. Rev.*, 2009, **61**, 1177–1188.

8. D. P. Nowotnik and E. Cvitkovic, ProLindac (AP5346): a review of the development of an HPMA DACH platinum polymer therapeutic, *Adv. Drug Deliv. Rev.*, 2009, **61**, 1214–1219.

9. S. D. Chipman, F. B. Oldham, G. Pezzoni and J. W. Singer, Biological and clinical characterization of paclitaxel poliglumex (PPX, CT-2103), a macromolecular polymer-drug conjugate, *Int. J. Nanomedicine*, 2006, **1**, 375–383.

10. G. J. Weiss, *et al.*, First-in-human phase 1/2a trial of CRLX101, a cyclodextrin-containing polymer-camptothecin nanopharmaceutical in patients with advanced solid tumor malignancies, *Invest. New Drugs*, 2013, **31**, 986–1000.

11. A. V. Yurkovetskiy and R. J. Fram, XMT-1001, a novel polymeric camptothecin pro-drug in clinical development for patients with advanced cancer, *Adv. Drug Deliv. Rev.*, 2009, **61**, 1193–1202.

12. J. E. Zuckerman, *et al.*, Correlating animal and human phase Ia/Ib clinical data with CALAA-01, a targeted, polymer-based nanoparticle containing siRNA, *Proc. Natl. Acad. Sci. U. S. A.*, 2014, **111**, 11449–11454.

13. P. Couvreur and C. Vauthier, Nanotechnology: intelligent design to treat complex disease, *Pharm. Res.*, 2006, **23**, 1417–1450.

14. M. J. Vicent, H. Ringsdorf and R. Duncan, Polymer therapeutics: clinical applications and challenges for development, *Adv. Drug Deliv. Rev.*, 2009, **61**, 1117–1120.

15. C. Kellner, *et al.*, Mimicking an induced self phenotype by coating lymphomas with the NKp30 ligand B7-H6 promotes NK cell cytotoxicity, *J. Immunol.*, 2012, **189**, 5037–5046.

16. D. Destouches, *et al.*, A simple approach to cancer therapy afforded by multivalent pseudopeptides that target cell-surface nucleoproteins, *Cancer Res.*, 2011, **71**, 3296–3305.

17. Z. Zhang, *et al.*, DNA-scaffolded multivalent ligands to modulate cell function, *Chembiochem*, 2014, **15**, 1268–1273.

18. L. L. Kiessling, J. E. Gestwicki and L. E. Strong, Synthetic multivalent ligands in the exploration of cell-surface interactions, *Curr. Opin. Chem. Biol.*, 2000, **4**, 696–703.

19. C. R. Bollinger, V. Teichgräber and E. Gulbins, Ceramide-enriched membrane domains, *Biochim. Biophys. Acta*, 2005, **1746**, 284–294.

20. B. Stephens and T. M. Handel, Chemokine receptor oligomerization and allostery, *Prog. Mol. Biol. Transl. Sci.*, 2013, **115**, 375–420.

21. K. Wu, J. Liu, R. N. Johnson, J. Yang and J. Kopeček, Drug-free macromolecular therapeutics: induction of apoptosis by coiled-coil-mediated cross-linking of antigens on the cell surface, *Angew. Chem. Int. Ed.*, 2010, **49**, 1451–1455.

22. R. Siegel, J. Ma, Z. Zou and A. Jemal, Cancer statistics, 2014, *CA Cancer J. Clin.*, 2014, **64**, 9–29.

23. J. O. Armitage and D. D. Weisenburger, New approach to classifying non-Hodgkin's lymphomas: clinical features of the major histologic subtypes. Non-Hodgkin's Lymphoma Classification Project, *J. Clin. Oncol.*, 1998, **16**, 2780–2795.

24. A. D. Zelenetz, *et al.*, Non-Hodgkin's lymphomas, version 4.2014, *J. Natl. Compr. Cancer Netw.*, 2014, **12**, 1282–1303.

25. B. D. Cheson and J. P. Leonard, Monoclonal antibody therapy for B-cell non-Hodgkin's lymphoma, *N. Engl. J. Med.*, 2008, **359**, 613–626.

26. D. G. Maloney, *et al.*, IDEC-C2B8 (rituximab) anti-CD20 monoclonal antibody therapy in patients with relapsed low-grade non-Hodgkin's lymphoma, *Blood*, 1997, **90**, 2188–2195.

27. D. G. Maloney, Anti-CD20 antibody therapy for B-cell lymphomas, *N. Engl. J. Med.*, 2012, **366**, 2008–2016.

28. A. Molina, A decade of rituximab: improving survival outcomes in non-Hodgkin's lymphoma, *Annu. Rev. Med.*, 2008, **59**, 237–250.

29. G. Cartron, *et al.*, Therapeutic activity of humanized anti-CD20 monoclonal antibody and polymorphism in IgG Fc receptor FcγRIIIa gene, *Blood*, 2002, **99**, 754–758.

30. M. R. Smith, Rituximab (monoclonal anti-CD20 antibody): mechanisms of action and resistance, *Oncogene*, 2003, **22**, 7359–7368.

31. I. Dransfield, Inhibitory FcγRIIb and CD20 internalization, *Blood*, 2014, **123**, 606–607.

32. T. Pham, P. Mero and J. W. Booth, Dynamics of macrophage trogocytosis of rituximab-coated B cells, *PloS One*, 2011, **6**, e14498.

33. P. Stashenko, L. M. Nadler, R. Hardy and S. F. Schlossman, Characterization of a human B lymphocyte-specific antigen, *J. Immunol.*, 1980, **125**, 1678–1685.

34. K. C. Anderson, *et al.*, Expression of human B cell-associated antigens on leukemias and lymphomas: a model of human B cell differentiation, *Blood*, 1984, **63**, 1424–1433.

35. O. W. Press, A. G. Farr, K. I. Borroz, S. K. Anderson and P. J. Martin, Endocytosis and degradation of monoclonal antibodies targeting human B-cell malignancies, *Cancer Res.*, 1989, **49**, 4906–4912.

36. R. B. Michel and M. J. Mattes, Intracellular accumulation of the anti-CD20 antibody 1F5 in B-lymphoma cells, *Clin. Cancer Res.*, 2002, **8**, 2701–2713.

37. J. K. Bubien, L. J. Zhou, P. D. Bell, R. A. Frizzell and T. F. Tedder, Transfection of the CD20 cell surface molecule into ectopic cell types generates a Ca^{2+} conductance found constitutively in B lymphocytes, *J. Cell Biol.*, 1993, **121**, 1121–1132.

38. T. F. Tedder and P. Engel, CD20: a regulator of cell-cycle progression of B lymphocytes, *Immunol. Today*, 1994, **15**, 450–454.

39. E. Janas, R. Priest and R. Malhotra, Functional role of lipid rafts in CD20 activity? *Biochem. Soc. Symp.*, 2005, pp 165–175.

40. P. Boross and J. H. W. Leusen, Mechanisms of action of CD20 antibodies, *Am. J. Cancer Res.*, 2012, **2**, 676–690.

41. M. Okroj, A. Österborg and A. M. Blom, Effector mechanisms of anti-CD20 monoclonal antibodies in B cell malignancies, *Cancer Treat. Rev.*, 2013, **39**, 632–639.

42. D. Shan, J. A. Ledbetter and O. W. Press, Apoptosis of malignant human B cells by ligation of CD20 with monoclonal antibodies, *Blood*, 1998, **91**, 1644–1652.

43. C. R. Kahn, K. L. Baird, D. B. Jarrett and J. S. Flier, Direct demonstration that receptor crosslinking or aggregation is important in insulin action, *Proc. Natl. Acad. Sci. U. S. A.*, 1978, **75**, 4209–4213.

44. Y. Shimizu, *et al.*, Crosslinking of the T cell-specific accessory molecules CD7 and CD28 modulates T cell adhesion, *J. Exp. Med.*, 1992, **175**, 577–582.

45. M. Fourcin, *et al.*, gp130 transducing receptor cross-linking is sufficient to induce interleukin-6 type responses, *J. Biol. Chem.*, 1996, **271**, 11756–11760.

46. L. D. Vallat, Y. Park, C. Li and J. G. Gribben, Temporal genetic program following B-cell receptor cross-linking: altered balance between proliferation and death in healthy and malignant B cells, *Blood*, 2007, **109**, 3989–3997.

47. J. P. Deans, H. Li and M. J. Polyak, CD20-mediated apoptosis: signalling through lipid rafts, *Immunology*, 2002, **107**, 176–182.

48. J. K. Hofmeister, D. Cooney and K. M. Coggeshall, Clustered CD20 induced apoptosis: src-family kinase, the proximal regulator of tyrosine phosphorylation, calcium influx, and caspase 3-dependent apoptosis, *Blood Cells. Mol. Dis.*, 2000, **26**, 133–143.

49. T. L. Unruh, *et al.*, Cholesterol depletion inhibits src family kinase-dependent calcium mobilization and apoptosis induced by rituximab crosslinking, *Immunology*, 2005, **116**, 223–232.

50. M.-A. Ghetie, *et al.*, Homodimerization of tumor-reactive monoclonal antibodies markedly increases their ability to induce growth arrest or apoptosis of tumor cells, *Proc. Natl. Acad. Sci. U. S. A.*, 1997, **94**, 7509–7514.

51. M.-A. Ghetie, H. Bright and E. S. Vitetta, Homodimers but not monomers of Rituxan (chimeric anti-CD20) induce apoptosis in human B-lymphoma cells and synergize with a chemotherapeutic agent and an immunotoxin, *Blood*, 2001, **97**, 1392–1398.

52. M. J. Polyak and J. P. Deans, Alanine-170 and proline-172 are critical determinants for extracellular CD20 epitopes; heterogeneity in the fine specificity of CD20 monoclonal antibodies is defined by additional requirements imposed by both amino acid sequence and quaternary structure, *Blood*, 2002, **99**, 3256–3262.

53. E. A. Rossi, *et al.*, Novel designs of multivalent anti-CD20 humanized antibodies as improved lymphoma therapeutics, *Cancer Res.*, 2008, **68**, 8384–8392.

54. R. Stein, *et al.*, Characterization of a humanized IgG4 anti-HLA-DR monoclonal antibody that lacks effector cell functions but retains direct antilymphoma activity and increases the potency of rituximab, *Blood*, 2006, **108**, 2736–2744.

55. C. Wang, R. J. Stewart and J. Kopeček, Hybrid hydrogels assembled from synthetic polymers and coiled-coil protein domains, *Nature*, 1999, **397**, 417–420.

56. J. Kopeček, Hydrogel biomaterials: a smart future? *Biomaterials*, 2007, **28**, 5185–5192.

57. J. Kopeček and J. Yang, Smart self-assembled hybrid hydrogel biomaterials, *Angew. Chem. Int. Ed.*, 2012, **51**, 7396–7417.

58. J. Yang, C. Xu, C. Wang and J. Kopeček, Refolding hydrogels self-assembled from *N*-(2-hydroxypropyl)methacrylamide graft copolymers by antiparallel coiled-coil formation, *Biomacromolecules*, 2006, **7**, 1187–1195.

59. J. Yang, K. Wu, Č. Koňák and J. Kopeček, Dynamic light scattering study of self-assembly of HPMA hybrid graft copolymers, *Biomacromolecules*, 2008, **9**, 510–517.

60. S. Lv, Y. Cao and H. Li, Tandem modular protein-based hydrogels constructed using a novel two-component approach, *Langmuir*, 2012, **28**, 2269–2274.

61. J. Kopeček, Soluble biomedical polymers, *Polim. Med.*, 1997, **7**, 191–221.

62. J. Kopeček, Controlled biodegradability of polymers – a key to drug delivery systems, *Biomaterials*, 1984, **5**, 19–25.

63. P. A. Vasey, *et al.*, Phase I clinical and pharmacokinetic study of PK1 [*N*-(2-hydroxypropyl)methacrylamide copolymer doxorubicin]: first member of a new class of chemotherapeutic agents-drug-polymer conjugates. Cancer Research Campaign Phase I/II Committee, *Clin. Cancer Res.*, 1999, **5**, 83–94.

64. J. Kopeček and P. Kopečková, HPMA copolymers: origins, early developments, present, and future, *Adv. Drug Deliv. Rev.*, 2010, **62**, 122–149.

65. K. Ulbrich and V. Šubr, Structural and chemical aspects of HPMA copolymers as drug carriers, *Adv. Drug Deliv. Rev.*, 2010, **62**, 150–166.

66. Y. B. Yu, Coiled-coils: stability, specificity, and drug delivery potential, *Adv. Drug Deliv. Rev.*, 2002, **54**, 1113–1129.

67. M. Pechar, *et al.*, Coiled coil peptides as universal linkers for the attachment of recombinant proteins to polymer therapeutics, *Biomacromolecules*, 2011, **12**, 3645–3655.

68. M. Pechar, *et al.*, Coiled coil peptides and polymer-peptide conjugates: synthesis, self-assembly, characterization and potential in drug delivery systems, *Biomacromolecules*, 2014, **15**, 2590–2599.

69. K. Wu, J. Yang, J. Liu and J. Kopeček, Coiled-coil based drug-free macromolecular therapeutics: *in vivo* efficacy, *J. Control. Release*, 2012, **157**, 126–131.

70. M. Pechar, P. Kopečková, L. Joss and J. Kopeček, Associative diblock copolymers of poly(ethylene glycol) and coiled-coil peptides, *Macromol. Biosci.*, 2002, **2**, 199–206.

71. N. C. Seeman, Nucleic acid junctions and lattices, *J. Theor. Biol.*, 1982, **99**, 237–247.

72. N. C. Seeman, DNA in a material world, *Nature*, 2003, **421**, 427–431.

73. Z.-G. Wang and B. Ding, DNA-based self-assembly for functional nanomaterials, *Adv. Mater.*, 2013, **25**, 3905–3914.

74. J. Li, C. Fan, H. Pei, J. Shi and Q. Huang, Smart drug delivery nanocarriers with self-assembled DNA nanostructures, *Adv. Mater.*, 2013, **25**, 4386–4396.

75. S. Nagahara and T. Matsuda, Hydrogel formation via hybridization of oligonucleotides derivatized in water-soluble vinyl polymers, *Polym. Gels Netw.*, 1996, **4**, 111–127.

76. K. Ding, F. E. Alemdaroglu, M. Börsch, R. Berger and A. Herrmann, Engineering the structural properties of DNA block copolymer micelles by molecular recognition, *Angew. Chem. Int. Ed.*, 2007, **46**, 1172–1175.

77. P. Pan, *et al.*, Thermoresponsive micellization and micellar stability of poly(*N*-isopropylacrylamide)-*b*-DNA diblock and miktoarm star polymers, *Langmuir*, 2012, **28**, 14347–14356.

78. P. E. Nielsen, DNA analogues with nonphosphodiester backbones, *Annu. Rev. Biophys. Biomol. Struct.*, 1995, **24**, 167–183.

79. J. Summerton and D. Weller, Morpholino antisense oligomers: design, preparation, and properties, *Antisense Nucleic Acid Drug Dev.*, 1997, **7**, 187–195.

80. J. E. Summerton, Morpholino, siRNA, and S-DNA compared: impact of structure and mechanism of action on off-target effects and sequence specificity, *Curr. Top. Med. Chem.*, 2007, **7,** 651–660.

81. D. Stein, E. Foster, S. B. Huang, D. Weller and J. Summerton, A specificity comparison of four antisense types: morpholino, 2'-*O*-methyl RNA, DNA, and phosphorothioate DNA, *Antisense Nucleic Acid Drug Dev.*, 1997, **7**, 151–157.

82. P. L. Iversen, Phosphorodiamidate morpholino oligomers: favorable properties for sequence-specific gene inactivation, *Curr. Opin. Mol. Ther.*, 2001, **3**, 235–238.

83. A. Amantana and P. L. Iversen, Pharmacokinetics and biodistribution of phosphorodiamidate morpholino antisense oligomers, *Curr. Opin. Pharmacol.*, 2005, **5**, 550–555.

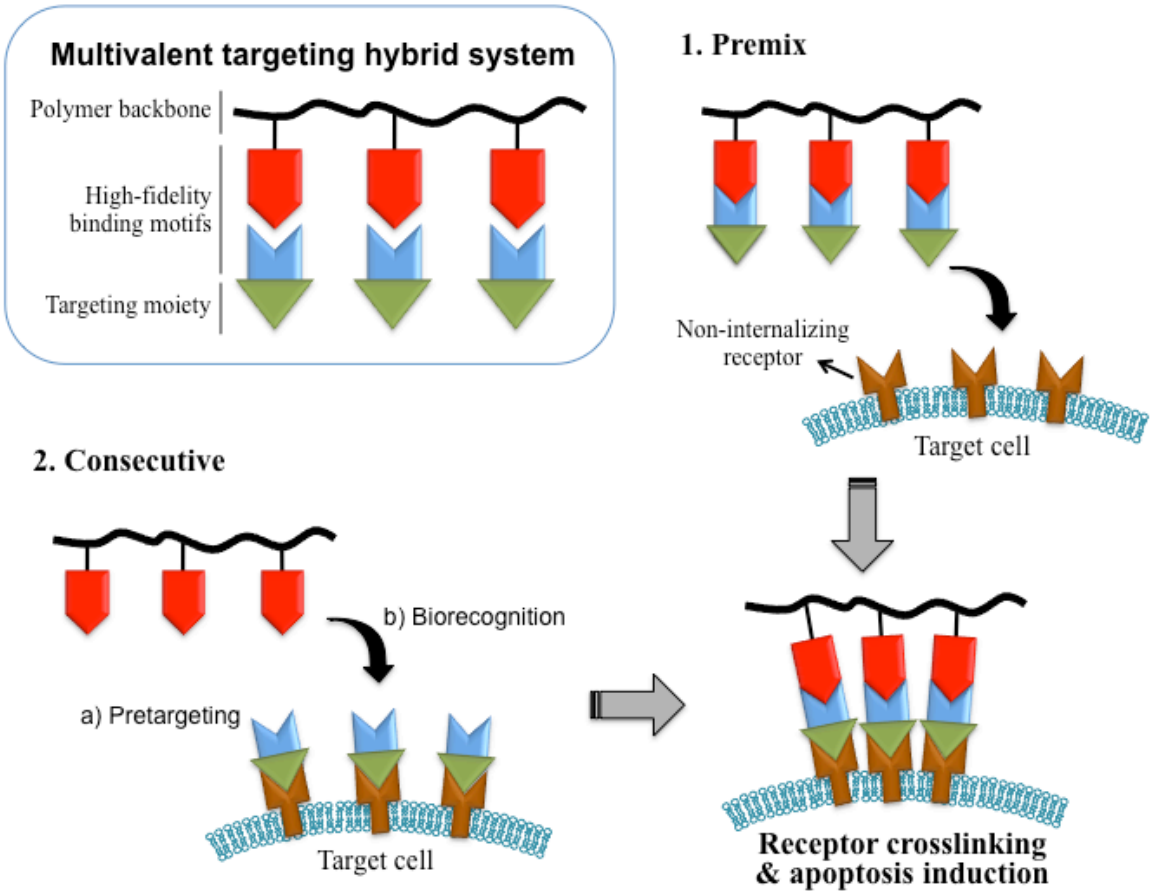

Figure 1.1 Drug-free macromolecular therapeutics for apoptosis induction. Crosslinking of cell surface noninternalizing receptors is mediated by the biorecognition of natural binding motifs. Two hybrid conjugates can be administered consecutively as pretargeting and crosslinking doses, or premixed to form a multivalent construct and used as a single dose.

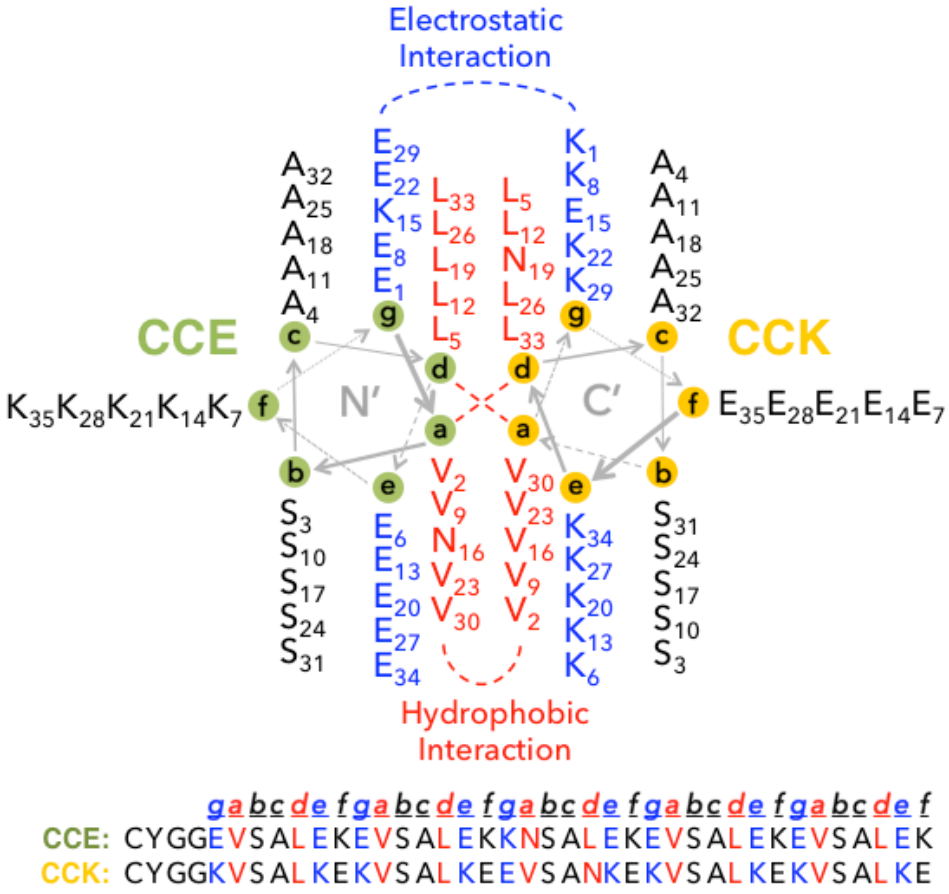

Figure 1.2 Helical wheel diagram of the CCE/CCK coiled-coil antiparallel heterodimer. The heptad repeat of each peptide is labeled *a–f*. Both CCE and CCK were modified with a YGG peptide spacer (to prevent steric hindrance of binding after grafted to polymer chains) and functionalized with a cysteine (for conjugation).

CHAPTER 2

ANTI-CD20 MULTIVALENT HPMA COPOLYMER – FAB' CONJUGATES FOR THE DIRECT INDUCTION OF APOPTOSIS[1]

In this chapter, a hybrid biomimetic system comprising high-molecular-weight, linear copolymer of *N*-(2-hydroxypropyl)methacrylamide (HPMA) grafted with multiple Fab' fragments of anti-CD20 monoclonal antibody (mAb) was synthesized by reversible addition-fragmentation chain transfer (RAFT) polymerization followed by attachment of Fab' fragments *via* thioether bonds. Exposure of human non-Hodgkin's lymphoma (NHL) Raji B-cells to the multivalent conjugates resulted in crosslinking of CD20 receptors and commencement of apoptosis. Five conjugates with varying molecular weight and valence (amount of Fab' per polymer chain) were synthesized. One of the copolymers contained enzyme degradable peptide sequences (GFLG) in the backbone. The multivalency led to higher avidity and apoptosis induction compared to unconjugated whole mAb. Time-dependent studies showed that the cytotoxicity of conjugates exhibited a slower onset at shorter exposure times than mAb hyper-crosslinked with a secondary Ab; however, at longer time intervals the HPMA copolymer conjugates achieved significantly higher

[1]This chapter is adapted from the following publication: T.-W. Chu, J. Yang and J. Kopeček. Anti-CD20 multivalent HPMA copolymer – Fab' conjugates for the direct induction of apoptosis. *Biomaterials*. 2012; 33(29): 7174–7181. Elsevier.

biological efficacies. In addition, study of the relationship between the structure of conjugates and Raji B-cell apoptosis revealed that both valency and polymer molecular weight influenced biological activities, while insertion of peptide sequences into the backbone was not a factor *in vitro*.

2.1 Background

The use of hybrid biomaterials composed of synthetic and biological macromolecules to design "smart" nanomedicines is an emerging field.[1,2] The goals include precise targeting to diseased sites, enhancing therapeutic efficiency, reducing adverse effects, and minimizing drug resistance. In particular, water-soluble HPMA copolymers are extensively used as delivery vehicles to conjugate anticancer therapeutic agents (*e.g.*, small molecule drugs) and targeting moieties (*e.g.*, antibodies).[3] HPMA polymer and copolymers have favorable physicochemical and pharmacokinetic properties to provide a well-defined safety profile, increase circulation half-life of therapeutics, and provide a flexible (random coil) conformation of the polymer backbone in solution.[4] The design of macromolecular therapeutics has extended towards a unique paradigm where biomimetic strategies are used to trigger specific responses or facilitate therapeutic efficiency through innate biological processes.[1,3,5,6] For instance, an HPMA-based hybrid system has been used as a "drug-free" macromolecular platform to induce apoptosis *via* biorecognition and receptor crosslinking at the cell surface; a clinically relevant therapeutic efficacy was demonstrated *in vitro*[6] and *in vivo*[7].

Non-Hodgkin's lymphoma (NHL) is a prevalent cancer in the United States with a history of over a half-million incidences and projected 70,130 new cases diagnosed in

2012.[8] Because about 85% of NHL is of B-cell origin and more than 95% of B-lymphomas bear the CD20 surface antigen,[9] immunotherapies using anti-CD20 monoclonal antibodies (mAb) have revolutionized the treatment of NHL.[10] However, the overall response levels to clinically used mAb, mainly rituximab (Rituxan®), for treatments of relapsed/refractory low-grade or follicular NHLs are less than 50%.[11] Rare but lethal side effects such as progressive multifocal leukoencephalopathy (PML) and lung injuries observed in patients treated with rituximab or other anti-CD20 mAb also raised biocompatibility concerns.[12–15] Therefore, new therapeutic strategies are needed.

The clinical nonresponsiveness and adverse effects of rituximab or other therapeutic mAb has been partly attributed to Fc fragment-related biological events.[14,16–18] The inactivity of effector cells to hyper-crosslink bound rituximab on B-cell surface *via* Fc results in failure of antibody-dependent cellular cytotoxicity (ADCC) and complement-dependent cytotoxicity (CDC), the main thrusts of anti-CD20 mAb's therapeutic effect.[16,18–20] In addition, Fc-mediated cellular events such as complement activation or the surge release of tumor necrosis factor-α (TNFα) upon mAb infusion are related to the severe side effects.[12,14,17] Consequently, approaches aiming at direct apoptosis induction through cell surface receptor clustering are becoming attractive.[21–25] In these previous studies, either multimeric Abs covalently linked to each other,[24,25] bound to dextran,[22] to lipid nanoparticles,[23] or monomeric Ab lacking effector cell functions hyper-crosslinked by a secondary Ab[21] were used to specifically enhance apoptosis. In particular, Rossi *et al.* developed a hexavalent anti-CD20 Ab by covalently assembling 6 Fab' to 1 Fc, and demonstrated that its antitumor efficacy in a murine model was comparable to mAb monomer (Veltuzumab), but without any sign of CDC.[25]

We have reported a hybrid biomimetic system composed of branched HPMA copolymer and multiple Fab' fragments of the anti-CD20 mAb (1F5), which targets and crosslinks CD20 on the surface of B-cells.[26,27] We hypothesized that the crosslinking would lead to clustering of (noninternalizing) CD20 antigens and induction of apoptosis *via* CD20-mediated signaling pathways. The design features the absence of Fc fragment and multimeric interactions with targets. Superior binding affinity[26] and apoptosis induction[27] when compared to unconjugated mAb were observed in several B-cell lines. Here, we aimed at improving this system using high-molecular-weight linear HPMA copolymers synthesized by controlled radical polymerization. This provided tailor-made multivalent conjugates with narrow molecular weight distribution, precise control of valences (Fab' content per polymer chain), well-defined and reproducible architectures, and potentially longer circulating half-lives. The improved design permitted the study of the relationship between the structure of conjugates and their biological activities, which facilitated the understanding of processes involved in CD20-crosslinking mediated apoptosis induction.

2.2 Materials and Methods

2.2.1 Materials

N-(3-Aminopropyl)methacrylamide hydrochloride (APMA) was purchased from Polysciences (Warrington, PA). 4,4'-azobis(4-cyanopentanoic acid) (V-501) was obtained from Wako Chemicals (Richmond, VA). Succinimidyl-4-(*N*-maleimidomethyl) cyclohexane-1-carboxylate (SMCC) and sulfo-SMCC were purchased from Soltec Ventures (Beverly, MA). o-Phthalic dicarboxaldehyde (OPA) and 3-mercaptopropionic

acid (MPA) were purchased from Sigma-Aldrich (St. Louis, MO). *N*-(2-Hydroxypropyl)methacrylamide (HPMA)[28] and 4-cyanopentanoic acid dithiobenzoate (CPDB)[29] were prepared as previously described. All solvents were obtained from Sigma-Aldrich as the highest purity available.

2.2.2 Cell Line, Hybridoma, and Fab' Fragment Preparation

Human Burkitt's B-cell non-Hodgkin's lymphoma Raji cell line (ATCC, Bethesda, MD) was used for biological evaluations. Cells were cultured in RPMI-1640 medium (Sigma, St. Louis, MO) supplemented with 10% fetal bovine serum (Hyclone, Logan, UT) and grown at 37 °C in a humidified atmosphere with 5% CO_2 (v/v). All experiments were performed using cells in exponential growth phase. Murine 1F5 anti-CD20 IgG2a antibody was prepared from the hybridoma clone 1F5 in a CellMax bioreactor (Spectrum Laboratories, Rancho Dominguez, CA) according to the manufacturer's instructions. Cells were initially cultured in aforementioned conditions and adapted to chemically defined, serum-free medium (Invitrogen, Carlsbad, CA). Anti-CD20 mAb was purified on a Protein G Sepharose 4 Fast Flow column (GE Healthcare, Piscataway, NJ) from bioreactor harvest supernatant. Preparation of Fab' fragment from the whole Ab was achieved using a previously reported procedure.[6, 26] Briefly, 1F5 mAb was digested into $F(ab')_2$ with 10% (w/w) pepsin (Sigma, St. Louis, MO) in 0.1 M citric buffer (pH 4.0) and labeled with Rhodamine Red™-X succinimidyl ester (R6010) (Molecular Probes®, Invitrogen). Immediately before use, 5 mg/mL of $F(ab')_2$ was reduced to Fab' with 5 mM tris(2-carboxyethyl)phosphine (TCEP) (Thermo Scientific, Waltham, MA) in 0.1 M phosphate buffered saline (PBS) (pH 6.5).

2.2.3 HPMA Copolymers and Polymer Precursors

Synthesis of HPMA copolymer with pendant amino groups (P-NH_2) and its conversion into maleimide-derivatized polymer precursor (P-mal) are depicted in Figure 2.1. P-NH_2 was synthesized by reversible addition-fragmentation chain transfer (RAFT) copolymerization of HPMA and APMA in deionized (DI) water at 70°C using CPDB as chain transfer agent (CTA) and V-501 as initiator. For the backbone degradable polymer precursor, a bifunctional dithiobenzoate containing enzyme cleavable oligopeptide Gly-Phe-Leu-Gly (GFLG) was synthesized[29] and used as CTA (N^{α},N^{ε}-bis(4-cyano-4-(phenylcarbonothioylthio)pentanoylglycylphenylalanylleucylglycyl)lysine, abbreviated peptide2CTA) (Figure 2.1A). A typical polymerization was as follows: HPMA (134.6 mg, 0.94 mmol) and APMA (10.7 mg, 0.06 mmol) were added into an ampoule attached to a Schlenk-line. After three vaccum-nitrogen cycles to remove oxygen, 0.46 mL degassed DI H_2O was added to dissolve monomers, followed by addition of CPDB solution (0.35 mg in 60 μL methanol) and V-501 solution (0.12 mg in 60 μL methanol) *via* syringe. The mixture was bubbled with nitrogen for 15 min before sealing the ampoule; the copolymerization was performed at 70°C for 20 h. The copolymer was isolated by precipitation into acetone and purified by dissolution-precipitation in methanol-acetone twice and dried under vacuum. Yield of P-NH_2 was 127 mg (87.3%). The molecular weight (Mw) and molecular weight distribution (Mw/Mn) were determined by size-exclusion chromatography (SEC) on ÄKTA FPLC system (GE Healthcare, Piscataway, NJ) equipped with miniDAWN and OptilabREX detectors. Superose 6 HR10/30 column (GE Healthcare) was used with sodium acetate buffer (pH 6.5) and 30% acetonitrile (v/v) as mobile phase. The content of amino groups in the

copolymer was determined by ninhydrin assay.[30]

After polymerization, P-NH_2 copolymers were reacted with 2,2'-azobis(2,4-dimethyl valeronitrile) (V-65) (Wako Chemicals) to remove the terminal (active) dithiobenzoate groups. Briefly, HPMA copolymer (45 mg, Mn = 105 kDa, 0.43 μmol) and V65 (20× excess, 2.13 mg, 8.57 μmol) were added into an ampoule. After three vacuum-nitrogen cycles to remove oxygen, 0.4 mL methanol was added. The solution was bubbled with nitrogen for 15 min, sealed and reacted at 50°C for 3 h. The end-modified copolymer was purified by precipitation into acetone twice and then dried under vacuum (yield 42 mg).

The side chain amino groups of P-NH_2 were converted to maleimides by reaction with SMCC or sulfo-SMCC in DMF in the presence of triethylamine (TEA). A mixture of 42 mg P-NH_2 (12.6 μmol NH_2) and SMCC (12.7 mg, 37.8 μmol) was dissolved in 0.5 ml DMF followed by dropwise addition of TEA (ratio of [NH_2]:[SMCC]:[TEA] = 1:3:3), then kept at room temperature overnight. The product was precipitated into acetone/ether (2:1, v/v), filtered, and redissolved in methanol, precipitated into acetone again, filtered and dried under vacuum. The amount of maleimide in copolymer was determined by a modified Ellman's assay.[31] The conversion of amine into maleimido groups was 54%–59% with SMCC and > 80% when sulfo-SMCC was used.

2.2.4 Preparation of Multivalent Conjugates

The polymer precursors P-mal were conjugated with reduced 1F5 Fab' fragments *via* thioether bonds following a previously established protocol.[32] In brief, 10 mg of P-mal were dissolved in 100 μL of DMSO, and the solution was added to Fab' (5 mg/mL)

in PBS (pH 6.5) (ratio of [mal]:[Fab'] = 5:1). The products were purified on a Superose 6 HR16/60 column (GE Healthcare) to remove unbound Fab', if any. The HPMA copolymer–Fab' conjugates (P-Fab') containing varying amounts of Fab' per macromolecule were collected and analyzed on a Superose 6 HR10/30 column. Fab'-equivalent concentration of conjugates was determined by UV spectroscopy, measuring absorbance at 280 nm on a Varian Cary 400 Bio UV-visible spectrophotometer, and confirmed by bicinchoninic acid (BCA) protein assay (Thermo Scientific).

2.2.5 Determination of Valence and Effective Diameter

A modified amino acid analysis procedure was utilized to determine the concentrations of amino acid residues from Fab' as well as 1-amino-2-propanol derived from the HPMA polymer backbone. This enables the calculation of valence (number of Fab' per polymer chain) of P-Fab' conjugates. In practice, after hydrolysis in 6 N HCl (125 °C, 24 h), samples were precolumn derivatized with o-phthalic dicarboxaldehyde in the presence of 3-mercaptopropionic acid, and analyzed by HPLC (Agilent Technologies, Santa Clara, CA) equipped with an eclipse XDB-C8 column and fluorescence detector (excitation 229 nm, emission 450 nm). Free 1F5 Fab' and HPMA homopolymer were used for calibration, which was performed by a significant peak indicating glutamate (for Fab') and a significant peak indicating 1-amino-2-propanol (for HPMA polymers).

The effective diameters of HPMA copolymer–Fab' conjugates were analyzed by dynamic light scattering using a Brookhaven BI-200SM goniometer and BI-9000AT digital correlator equipped with a He-Ne laser (λ = 633 nm) at room temperature in PBS (pH 7.4). The scattering angle was 90°. Samples in PBS (1 mg/mL, Fab' equivalent

concentration) were filtered through a 0.45 μm filter before measurement. To rule out the possibility of aggregation of P-Fab' conjugates in solution, samples were also measured at lower concentrations (0.5, 0.25 mg/mL). P-NH_2 polymer precursors, 1F5 mAb, and Fab' fragment were also analyzed. All measurements were performed in at least triplicate.

2.2.6 Confocal Fluorescence Microscopy

Confocal fluorescence microscopy was used to detect the biorecognition of (rhodamine-labeled) P-Fab' conjugates at the surface of Raji B-cells. Cells at a density of 2.5–5.0 × 10^5 per well were incubated with 0.5 mL of varying concentrations of conjugates (1, 2, 5, and 10 μM) in culture medium at 37 °C, 5% CO_2 for 2 h prior to analysis. After incubation, media containing conjugates were discarded. The cells were washed twice with PBS, and then plated onto sterile 35 mm glass bottom dishes with 14 mm microwells (MatTek Corporation, Ashland, MA) for live cell fluorescence imaging using Olympus laser scanning confocal microscope (FV 1000). As controls, cells incubated with FITC-labeled 1F5 mAb, rhodamine-labeled $F(ab')_2$, and PBS were also examined.

2.2.7 Apoptosis Evaluation

Apoptosis induction of Raji cells following exposure to the multivalent conjugates was evaluated by three assays: caspase-3 activation, annexin V binding, and TUNEL (terminal deoxynucleotide mediated-dUTP nick-end labeling) assay. Quantification of apoptotic activity was performed by flow cytometry, and presented as “apoptotic index” (% apoptotic cells). In all experiments, 1F5 mAb hyper-crosslinked with a goat

antimouse (GAM) secondary antibody (2° Ab) (KPL, Gaithersburg, MD) was used as a positive control (molar ratio 1F5:GAM = 3:1). Cells treated with: (a) free anti-CD20 Fab' fragments, (b) mixture of Fab' and P-NH_2 (equivalent amounts to conjugates), and (c) culture medium only, were used as negative controls.

2.2.7.1 Caspase-3 Activity

Caspase-3 activity was characterized by analysis of treated cells with the PhiPhiLux kit (OncoImmunin, Gaithersburg, MD). Prior to analyses, 2.5×10^5 Raji cells were suspended in 0.5 mL fresh growth medium with 2 μM of Fab' equivalent of conjugates. The cells were treated for 6 h in a humidified atmosphere at 37 °C and 5% CO_2 and then analyzed for caspase-3 activation following the manufacturer's protocol. For treatments using hyper-crosslinked mAb, cells were firstly incubated with 2 μM of 1F5 mAb for 1 h, and then washed twice with PBS + 1% BSA, followed by re-suspension in 0.5 mL of fresh growth medium with 100 μg per mL of GAM. The cells were incubated for another 5 h at 37 °C prior to staining. All experiments were carried out in triplicate.

2.2.7.2 Annexin V Binding

Apoptotic activity was studied by treating Raji cells with conjugates followed by annexin V staining using the RAPID protocol provided by the manufacturer (Oncogene Research Products, Boston, MA). In addition, annexin V binding assay was chosen to further study the processes in time- and concentration-dependent manner. For each assay, 2.5×10^5 cells were suspended in 0.5 mL of fresh growth medium with an appropriate

amount of conjugate (conjugates in Fab' equivalent ranged from 1 to 8 μM) and incubated for 20 h, 40 h, or 60 h. For positive controls, cells were treated with 1F5 mAb at concentrations from 1 to 8 μM in growth medium for 1 h. The cells were then washed and suspended in 0.5 mL of fresh growth medium with corresponding amounts of GAM antibody (from 50 to 400 μg per mL) (molar ratio 1F5:GAM = 3:1). The cells were treated for another 19 h, 39 h, or 59 h at 37 °C prior to staining. All experiments were carried out in triplicate.

2.2.7.3 TUNEL Assay

Analysis of DNA fragmentation as characteristics of apoptosis was conducted using the TUNEL assay. In these experiments 7.5×10^5 Raji cells were treated with 2 μM of Fab' equivalent of conjugates in 0.5 mL of fresh growth medium and allowed to incubate for 20 h. Raji cells were treated with 2 μM of 1F5 mAb, and they were allowed to incubate for 1 h, and then washed twice with PBS + 1% BSA, followed by re-suspension into 0.5 mL of fresh growth media with 100 μg/mL of GAM antibody. The cells were incubated for another 19 h. Prior to analysis, the cells were fixed with 2% paraformaldehyde in PBS for 1 h at room temperature. Cells were then permeabilized in 70% ethanol overnight at 4 °C. Nick-end labeling was done using an Apo Direct TUNEL kit (Phoenix Flow Systems, San Diego, CA) following the manufacturer's protocol. All experiments were carried out in triplicate.

2.2.8 Cell Viability Study

Viabilities of Raji cells after different treatment times were analyzed by propidium iodide (PI) binding. Quantification of cell viability was performed with flow cytometry. For these experiments, all treatment conditions were identical to those in the time-dependent annexin V binding assays except for selection of different time intervals for analysis. In brief, cells were incubated with 2 μM (Fab'-equivalent) of HPMA copolymer–Fab' conjugates (or 1F5 mAb) for 24 h, 48 h, or 72 h (or 1 h for 1F5 mAb followed by exposure to 100 μg/mL of GAM for 23 h, 47 h, and 71 h). All experiments were carried out in triplicate.

2.2.9 Statistics

All quantified data were presented as means ± standard deviation (SD). Analyses were performed by the Student's *t*-test, with $p < 0.05$ considered as statistically significant.

2.3 Results and Discussion

2.3.1 Synthesis of Multivalent HPMA Copolymer – Fab' Conjugates

Previously, we have demonstrated that attaching multiple Fab' fragments to soluble, branched HPMA copolymer resulted in antigen binding enhancement.[26] Multivalent HPMA copolymer–Fab' conjugates showed significant apoptotic activity initiated by crosslinking the B-cell antigen CD20.[27] To further elucidate the relationship between the structure of HPMA copolymer–Fab' conjugates and their biological activities, a series of linear HPMA copolymers with variable chain lengths and different

contents of APMA comonomer (Fab' attachment points) was designed (Figure 2.1 and Table 2.1). Polymer precursor P1 with polymer backbone with average molecular weight 100 kDa contained the lowest number of pendant amino groups per polymer chain; it served as a "control conjugate." P2 had a double the backbone length (200 kDa) and identical amino group density with P1. P2a had a double the backbone length (200 kDa) but the same number of pendant amino groups as P1. Comparison of conjugates based on P1, P2, and P2a allowed evaluation of the impact of both valence and polymer chain length. P2b had polymer chain length (200 kDa) and pendant group numbers almost identical to P2; however, its backbone contained an enzyme cleavable oligopeptide (GFLG). Comparison of P2b with P2 will evaluate if the insertion of the peptide into polymer backbone would change the flexibility of polymer with potential influence on biorecognition by CD20 receptors. The degradability of the polymer backbone will be of utmost importance in future *in vivo* study. P3 possessed the longest polymer chain (300 kDa) and the highest number of amino groups, and will be used to assess the impact of multivalency.

As described above, multivalent HPMA copolymer – (anti-CD20) Fab' conjugates (P-Fab') were prepared in a three-step process (Figure 2.1A). First, the copolymers of HPMA and APMA (P-NH_2) were synthesized by RAFT copolymerization, which yielded copolymers with precisely designed molecular weight (Mw) and low polydispersity. This process is controllable; an excellent correlation between theoretical and experimental molecular weights was achieved (Table 2.1). This is an improvement over the synthesis using traditional radical polymerization.[26,27] Previously, copolymerization of HPMA and APMA was performed in the presence of a small amount of tetraethyleneglycol

dimethacrylate and produced branched copolymers with high polydispersity. Consequently, fractionation was required to prepare narrowly dispersed polymer precursors.[26]

For the synthesis of biodegradable polymer precursor, a bifunctional chain transfer agent (peptide2CTA) was used. The monomers were incorporated at both dithiobenzoate groups of peptide2CTA with identical efficiency[29] producing a diblock copolymer P2b with an enzyme degradable sequence (GFLG) in the middle of the polymer chain. Such diblock (or multiblock) HPMA polymers have demonstrated excellent backbone degradability in responses to papain and the lysosomal enzyme cathepsin B.[29,33,34]

After converting pendant amino groups to maleimido groups by reaction with heterobifunctional reagent, SMCC or sulfo-SMCC, HPMA copolymers (P-mal) were conjugated with freshly reduced Fab' fragments. Representative SEC profiles of P1 and P1-Fab' are shown in Figure 2.2; a significant shift of signal towards earlier elution time was observed which suggests successful attachment of Fab' to the polymer backbone.

For further characterization of the P-Fab' conjugates, dynamic light scattering (DLS) was used to determine the hydrodynamic effective diameters of the polymers before and after conjugation with Fab' (Table 2.2). To analyze the valence (number of Fab' fragments per polymer chain), a modified amino acid analysis (AAA) was performed (Table 2.2). The results of DLS on polymer precursors (P-NH_2) and unconjugated Fab' fragment corresponded well with both published values[35] and our previous observations[26]. For the conjugates, enlargement of the effective diameter was observed. To rule out aggregation, we measured the hydrodynamic volume at lower

concentrations of samples; no difference was found among different concentrations. The increased volume may be explained by dispersive forces between intrachain Fab' fragments, resulting in the expansion of the polymer coil. In addition, there is a slight possibility of a side reaction between residual amines from P-NH_2 (or amines of Fab') with the maleimido groups resulting in the formation of interchain covalent crosslinks. Nevertheless, when compared to branched HPMA copolymer–Fab' conjugates of comparable Mw and valences,[26] the effective diameters of linear P-Fab' are apparently larger. This could have significant impact on *in vivo* circulating half-life and biodistribution.

Several studies have demonstrated the positive correlation between hydrodynamic volumes of HPMA polymers, copolymers, or conjugates and their intravascular half-lives.[4,36–38] Thus, the P-Fab' conjugates presented here will very likely possess prolonged systematic circulation times. Previous studies on therapeutic mAb or multimeric Ab have pointed out the significant influence of unintended alteration of serum half-life after genetic engineering or physicochemical modification on *in vivo* therapeutic efficacy.[22,23,25] For instance, Popov *et al.* reported the rapid elimination from blood circulation of multivalent rituximab lipid nanoparticles (Ritux-LNPs), and ascribed the observed absence of increase in *in vivo* therapeutic efficacies (when compared to rituximab) to the decreased circulating half-life.[23] The recent design of backbone degradable HPMA copolymers[29,33,34] will permit the use of high-Mw, long-circulating conjugates without impairment of therapeutic efficacy.

Confocal fluorescence microscopy (Figure 2.3) demonstrated the localization of (rhodamine-labeled) conjugates at the surface of Raji B-cell, corresponding to a high

expression level of noninternalizing CD20 surface antigen of this cell line. This result further illustrated the successful synthesis of conjugates with retained biological activity of anti-CD20 Fab' in order to target B-cells.

2.3.2 Relationship Between Polymer Chain Length and Valence of P-Fab' Conjugates and Apoptosis Induction in Raji B-Cells

Previous studies demonstrated that crosslinking of noninternalizing CD20 receptors on Raji B-cells results in receptor clustering with concomitant apoptosis induction. The evaluation of apoptosis initiation following Raji B-cell exposure to multivalent conjugates was performed by three distinct assays from differing perspectives: caspase-3 activation (gene expression due to CD20-mediated signaling), annexin V binding (cell membrane flipping as an early apoptotic event), and the TUNEL assay (DNA fragmentation as a late apoptotic event). Levels of apoptosis induction by the five conjugates (Table 2.2) were compared; results from the three assays were consistent and showed very similar trends (Figure 2.4). P1-Fab' designed as a "control conjugate" had the weakest apoptotic activity among the five, with only minimal effects detected when compared to the untreated group (culture medium only), unconjugated Fab', and Fab' + P-NH_2 controls. Conjugate P2-Fab' with doubled backbone length and doubled valence (than P1-Fab') produced significant apoptotic levels as expected. Interestingly, P2a-Fab' with similar valence as P1-Fab' but a longer polymer chain seemed to have stronger apoptotic efficacy than P1-Fab' (but less than P2-Fab'), suggesting that in addition to valence, polymer chain length could also be a factor for apoptosis induction. This result is striking because, first, none of the previous literature on multimeric anti-

CD20 mAb has published the positive influence of polymer length on apoptosis, and second, Rossi *et al.* suggested the need for clustering at least three CD20 to induce cytotoxicity[25] (noting that the mean valence of P2a-Fab' is 1.3). Data reported here could be potentially explained by either an improved binding kinetics of the conjugate, or a better range of "reaching" to cluster neighboring CD20 as a result of the longer polymer chain, although further analysis is necessary.

Furthermore, P2b-Fab' had almost identical polymer chain length and valence as P2-Fab' but with a peptide (GFLG)-containing enzyme cleavable backbone. The similar degrees of apoptosis observed in P2b-Fab' and P2-Fab' indicate that the insertion of peptide segments into the polymer backbone does not have a noticeable impact on the flexibility of the macromolecule and on its potential to attach to multiple CD20 antigens on the surface of Raji B-cells. In addition, these biodegradable HPMA-based polymer carriers[29,33,34] possess favorable properties for *in vivo* applications. They have long plasma circulation time, their biodegradability profiles can be easily manipulated, and they possess favorable pharmacokinetics and a favorable tumor-to-normal tissue accumulation ratio.[4,39] Data presented here rationalize the future design of a biodegradable, multiblock P-Fab' system composed of HPMA copolymer blocks of molecular weight below the renal threshold (40–45 kDa).

The conjugate P3-Fab' was designed with the longest backbone and highest valence with the aim of achieving an optimal biological efficacy. Although the conjugate P3-Fab' produced the highest apoptotic level among the five conjugates, the enhancement of activity observed at the experimental conditions used (2 μM Fab'-equivalent concentration, 20 h incubation) was modest. We hypothesize that the combination of a

high valence (11.3) and a long polymer chain (336 kDa) might result in a solution conformation that renders some Fab' fragments less accessible (shielded) to interaction with CD20, thus limiting the targeting effect.[40] This explanation was supported by results of DLS (Table 2.2); P3-Fab' had a mean hydrodynamic diameter of 97.3 nm – a modest increase when compared to the other conjugates.

2.3.3 Impact of Exposure Time and P-Fab' Concentration on Apoptosis Induction and Cytotoxicity

A time-dependent cell viability study (Figure 2.5) was performed using propidium iodide (PI) and flow cytometry. PI is a fluorescent DNA-intercalating agent commonly used to bind and detect nonviable cells, or to distinguish late apoptotic cells depending on the experimental setup;[41] here, we applied the former to stain and quantify all nonviable cells. The viability of Raji cells was analyzed at varying time intervals after exposure to multivalent conjugates at similar conditions as used in apoptosis assays described above. The cytotoxicity of conjugates demonstrated a slower onset at shorter exposure times (24 h, 48 h) than the whole 1F5 mAb hyper-crosslinked with a secondary Ab (mAb + 2°Ab); however, at the longer time interval (72 h) the conjugates appeared to be more effective. For instance, at 72 h, conjugates P2-Fab' and P2b-Fab' showed comparable effects as the positive control (mAb + 2°Ab), while P3-Fab' achieved a significantly better efficacy. In the time-dependent apoptosis evaluation (Figure 2.6A) using annexin V assay, the onset patterns of apoptosis were the same as observed in the cytotoxicity assay. Both, P2-Fab' and P3-Fab' reached comparable levels of early apoptosis as the positive control at longer exposure times (40 h, 60 h). In particular, at 60 h, the apoptotic activity of P3-Fab'

exceeded that of the positive control ($p < 0.05$). Since the trends of cytotoxicity compared well with results of apoptosis, we speculate that the PI-positive cells primarily resulted from CD20 clustering (late apoptotic cells); however, the potential contribution of cell necrosis cannot be ruled out. These data and the previous observation that the therapeutic efficacy of anti-CD20 mAb may result in direct eradication of B-lymphomas[10,11,18] bode well for the potential of P-Fab' conjugates as therapeutics for NHL.

The concentration (dose)-dependent apoptosis assay (Figure 2.6B) revealed an increase of apoptotic index with increasing concentration for all compounds tested. However, the dose-escalation effect was stronger in the positive control group (mAb + 2°Ab) than in multivalent conjugates P2-Fab' and P3-Fab'. In addition, within the concentration range used (1–8 μM), saturation of apoptotic index at high concentrations was not observed in contrast to results obtained with branched polymer–Fab' conjugates.[27] This suggests a better accessibility of Fab' fragments bound to linear polymer chains when compared to branched conjugates. This hypothesis is further supported by the comparison of effective diameters of conjugates; the linear P-Fab' conjugates possess larger hydrodynamic sizes than branched conjugates with equivalent Mw, polydispersity, and valency.

The data seem to suggest that to achieve enhanced biological activities, a long exposure time of linear P-Fab' was more important than a high Fab'-equivalent concentration. Two factors may contribute to this phenomenon: (a) shielding effect,[40] and (b) different binding kinetics to CD20 between P-Fab' and mAb followed by 2° Ab. The impact of time corresponds well with the design of backbone degradable, long-circulating conjugates. Optimization of the structure of conjugates based on the best combination of

molecular weight and valency needs to be undertaken.

2.4 Summary

A hybrid biomimetic system composed of RAFT-synthesized, linear, high-Mw HPMA copolymers grafted with multiple anti-CD20 Fab' fragments was designed. The preparation methods did not require fractionation by SEC, thus are well suited for scale-up studies. The technique enabled synthesis of conjugates with low polydispersity and tailor-made properties to study the structure-activity relationship. The biorecognition of multivalent P-Fab' conjugates by CD20 receptors on the surface of Raji B-cells was visualized by confocal fluorescence microscopy. Crosslinking of CD20 receptors on the surface of Raji B-cells induced apoptosis as determined by caspase-3 activity, annexin V binding, and TUNEL assays. Both polymer chain length and valence (amount of Fab' per chain) were factors having an impact on apoptotic efficiency, whereas insertion of a peptide into the HPMA copolymer backbone was not. In addition, long exposure time of the conjugates with Raji B-cells resulted in enhanced apoptosis and higher cytotoxicity when compared to whole anti-CD20 mAb hyper-crosslinked by a secondary Ab; high dose (concentration) seemed to be less influential. The present system possesses ideal architecture (linear) and characteristics (suitable hydrodynamic size, as analyzed by DLS) to allow the further design of long-circulating biodegradable systems. Based on the presented data and the favorable characteristics of CD20 (noninternalizing, not present in serum under standard conditions, with no known natural ligand) as a target for B-lymphoma, this study provides a potential strategy for the improved treatment of NHL and other B-cell malignancies through direct induction of apoptosis without Fc-related

mechanisms and side effects.

2.5 References

1. P. Couvreur and C. Vauthier, Nanotechnology: intelligent design to treat complex disease, *Pharm. Res.*, 2006, **23**, 1417–1450.

2. J. Kopeček, Smart and genetically engineered biomaterials and drug delivery systems, *Eur. J. Pharm. Sci.*, 2003, **20**, 1–16.

3. J. Kopeček and P. Kopečková, HPMA copolymers: origins, early developments, present, and future, *Adv. Drug Deliv. Rev.*, 2010, **62**, 122–149.

4. K. Ulbrich and V. Šubr, Structural and chemical aspects of HPMA copolymers as drug carriers, *Adv. Drug Deliv. Rev.*, 2010, **62**, 150–166.

5. M. J. Vicent, H. Ringsdorf and R. Duncan, Polymer therapeutics: clinical applications and challenges for development, *Adv. Drug Deliv. Rev.*, 2009, **61**, 1117–1120.

6. K. Wu, J. Liu, R. N. Johnson, J. Yang and J. Kopeček, Drug-free macromolecular therapeutics: induction of apoptosis by coiled-coil-mediated cross-linking of antigens on the cell surface, *Angew. Chem. Int. Ed.*, 2010, **49**, 1451–1455.

7. K. Wu, J. Yang, J. Liu and J. Kopeček, Coiled-coil based drug-free macromolecular therapeutics: *in vivo* efficacy, *J. Control. Release*., 2012, **157**, 126–131.

8. R. Siegel, D. Naishadham and A. Jemal, Cancer statistics, 2012, *CA Cancer J. Clin.*, 2012, **62**, 10–29.

9. P. Stashenko, L. M. Nadler, R. Hardy and S. F. Schlossman, Characterization of a human B lymphocyte-specific antigen, *J. Immunol.*, 1980, **125**, 1678–1685.

10. B. D. Cheson and J. P. Leonard, Monoclonal antibody therapy for B-cell non-Hodgkin's lymphoma, *N. Engl. J. Med.*, 2008, **359**, 613–626.

11. A. Molina, A decade of rituximab: improving survival outcomes in non-Hodgkin's lymphoma, *Annu. Rev. Med.*, 2008, **59**, 237–250.

12. M. Allison, PML problems loom for Rituxan, *Nat. Biotechnol.*, **28**, 105–106.

13. E. O. Major, Reemergence of PML in natalizumab-treated patients – new cases, same concerns, *N. Engl. J. Med.*, 2009, **361**, 1041–1043.

14. L. C. Lands, New therapies, new concerns: rituximab-associated lung injury, *Pediatr. Nephrol.*, 2010, **25**, 1001–1003.

15. K. Kamei, S. Ito and K. Iijima, Severe respiratory adverse events associated with rituximab infusion, *Pediatr. Nephrol.*, 2010, **25**, 1193.

16. G. Cartron, *et al.*, Therapeutic activity of humanized anti-CD20 monoclonal antibody and polymorphism in IgG Fc receptor FcγRIIIa gene, *Blood*, 2002, **99**, 754–758.

17. L. E. van der Kolk, A. J. Grillo-López, J. W. Baars, C. E. Hack and M. H. van Oers, Complement activation plays a key role in the side-effects of rituximab treatment, *Br. J. Haematol.*, 2001, **115**, 807–811.

18. M. R. Smith, Rituximab (monoclonal anti-CD20 antibody): mechanisms of action and resistance, *Oncogene*, 2003, **22**, 7359–7368.

19. S. de Haij, *et al.*, *In vivo* cytotoxicity of type I CD20 antibodies critically depends on Fc receptor ITAM signaling, *Cancer Res.*, 2010, **70**, 3209–3217.

20. J. Golay, *et al.*, The role of complement in the therapeutic activity of rituximab in a murine B lymphoma model homing in lymph nodes, *Haematologica*, 2006, **91**, 176–183.

21. R. Stein, *et al.*, Characterization of a humanized IgG4 anti-HLA-DR monoclonal antibody that lacks effector cell functions but retains direct antilymphoma activity and increases the potency of rituximab, *Blood*, 2006, **108**, 2736–2744.

22. N. Zhang, L. A. Khawli, P. Hu and A. L. Epstein, Generation of rituximab polymer may cause hyper-cross-linking–induced apoptosis in non-Hodgkin's lymphomas, *Clin. Cancer Res*., 2005, **11**, 5971–5980.

23. J. Popov, *et al*., Multivalent rituximab lipid nanoparticles as improved lymphoma therapies: indirect mechanisms of action and *in vivo* activity, *Nanomed*., 2011, **6**, 1575–1591.

24. M.-A. Ghetie, H. Bright and E. S. Vitetta, Homodimers but not monomers of Rituxan (chimeric anti-CD20) induce apoptosis in human B-lymphoma cells and synergize with a chemotherapeutic agent and an immunotoxin, *Blood*, 2001, **97**, 1392–1398.

25. E. A. Rossi, *et al.*, Novel designs of multivalent anti-CD20 humanized antibodies as improved lymphoma therapeutics, *Cancer Res.*, 2008, **68**, 8384–8392.

26. R. N. Johnson, P. Kopečková and J. Kopeček, Synthesis and evaluation of multivalent branched HPMA copolymer–Fab' conjugates targeted to the B-cell antigen CD20, *Bioconjug. Chem*., 2009, **20**, 129–137.

27. R. N. Johnson, P. Kopečková and J. Kopeček, Biological activity of anti-CD20 multivalent HPMA copolymer–Fab' conjugates. *Biomacromolecules*, 2012, **13**, 727–735.

28. J. Kopeček and H. Bažilová, Poly[*N*-(2-hydroxypropyl)methacrylamide] — I. Radical polymerization and copolymerization, *Eur. Polym. J.*, 1973, **9**, 7–14.

29. H. Pan, J. Yang, P. Kopečková and J. Kopeček, Backbone degradable multiblock *N*-(2-hydroxypropyl)methacrylamide copolymer conjugates *via* reversible addition-fragmentation chain transfer polymerization and thiol-ene coupling reaction, *Biomacromolecules*, 2011, **12**, 247–252.

30. B. Starcher, A ninhydrin-based assay to quantitate the total protein content of tissue samples, *Anal. Biochem.*, 2001, **292**, 125–129.

31. G. L. Ellman, Tissue sulfhydryl groups, *Arch. Biochem. Biophys.*, 1959, **82**, 70–77.

32. V. Omelyanenko, P. Kopečková, C. Gentry, J. G. Shiah and J. Kopeček, HPMA copolymer – anticancer drug – OV-TL16 antibody conjugates, 1. Influence of the method of synthesis on the binding affinity to OVCAR-3 ovarian carcinoma cells *in vitro*, *J. Drug Target.*, 1996, **3**, 357–373.

33. K. Luo, J. Yang, P. Kopečková and J. Kopeček, Biodegradable multiblock poly[*N*-(2-hydroxypropyl)methacrylamide] *via* reversible addition−fragmentation chain transfer polymerization and click chemistry. *Macromolecules*, 2011, **44**, 2481–2488.

34. J. Yang, K. Luo, H. Pan, P. Kopečková and J. Kopeček, Synthesis of biodegradable multiblock copolymers by click coupling of RAFT-generated heterotelechelic polyHPMA conjugates, *React. Funct. Polym.*, 2011, **71**, 294–302.

35. T. M. Allen, E. Brandeis, C. B. Hansen, G. Y. Kao and S. Zalipsky, A new strategy for attachment of antibodies to sterically stabilized liposomes resulting in efficient targeting to cancer cells, *Biochim. Biophys. Acta*, 1995, **1237**, 99–108.

36. T. Lammers, *et al.*, Effect of physicochemical modification on the biodistribution and tumor accumulation of HPMA copolymers, *J. Control. Release*, 2005, **110**, 103–118.

37. J.-G. Shiah, M. Dvořák, P. Kopečková, Y. Sun, C. M. Peterson and J. Kopeček, Biodistribution and antitumour efficacy of long-circulating *N*-(2-hydroxypropyl)methacrylamide copolymer-doxorubicin conjugates in nude mice, *Eur. J. Cancer*, 2001, **37**, 131–139.

38. M. Allmeroth, *et al.*, Modifying the body distribution of HPMA-based copolymers by molecular weight and aggregate formation, *Biomacromolecules*, 2011, **12**, 2841–2849.

39. J. Kopeček and P. Kopečková, Design of polymer-drug conjugates, In: *Drug Delivery in Oncology*, Eds.: F. Kratz, P. Senter and H. Steinhagen, Wiley-VCH, 2012, pp 485–512.

40. H. Ding, P. Kopečková and J. Kopeček, Self-association properties of HPMA copolymers containing an amphipathic heptapeptide, *J. Drug Target.*, 2007, **15**, 465–474.

41. L. Hervé, Nuclear apoptosis detection by flow cytometry: influence of endogenous endonucleases, *Exp. Cell Res.*, 2002, **277**, 1–14.

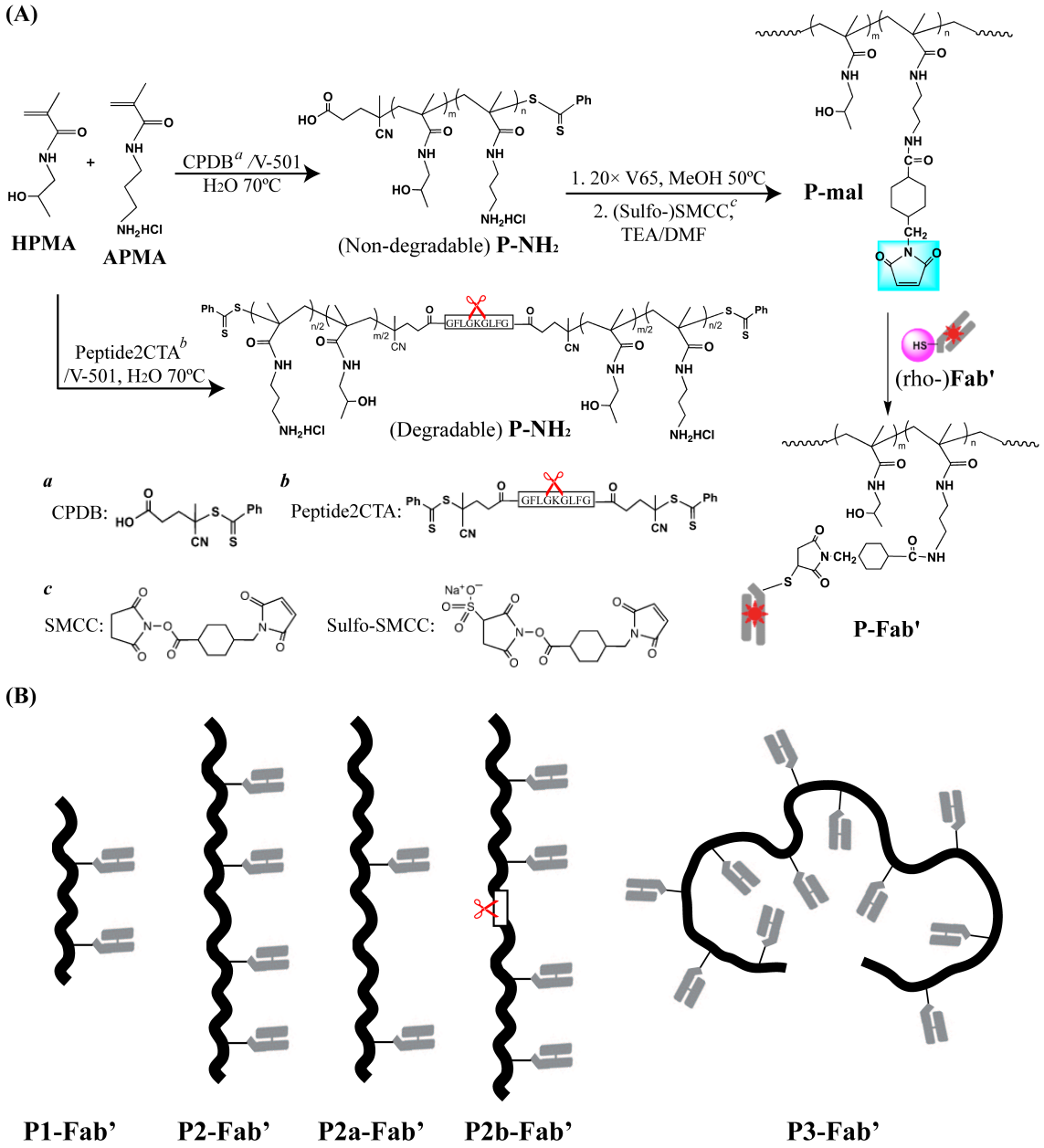

Figure 2.1 Synthesis of multivalent HPMA copolymer – Fab' conjugates. (A) Schemes for the synthesis of polymer precursors (P-NH_2, P-mal) and multivalent conjugates (P-Fab'). (B) Schematics of polymer conjugate architectures.

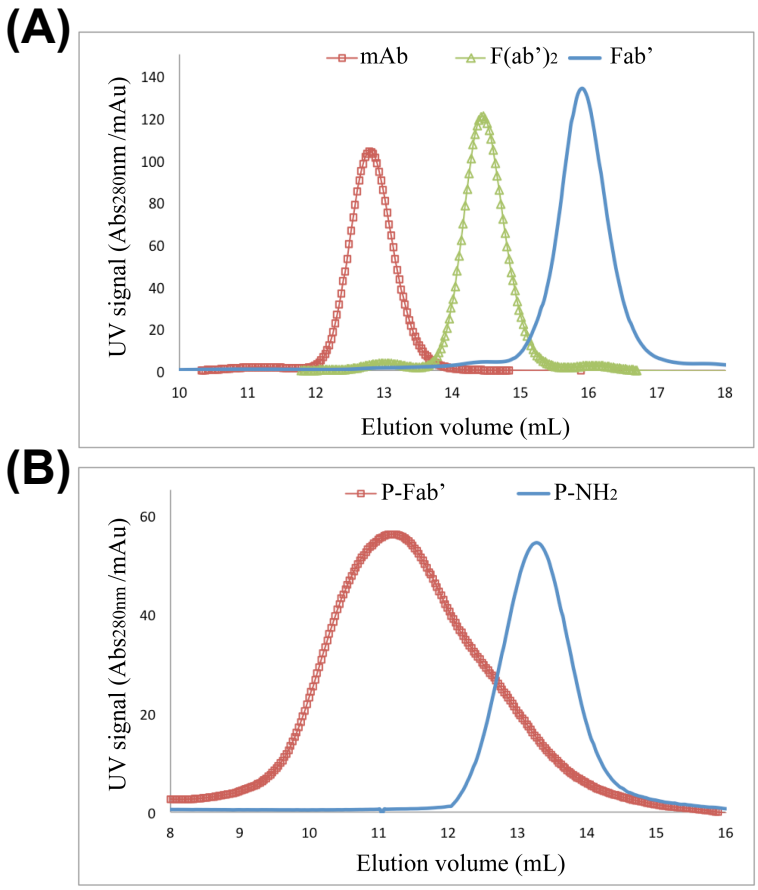

Figure 2.2 SEC profiles of 1F5 mAb, $F(ab')_2$, Fab', $P\text{-}NH_2$ and P-Fab'. (A) SEC profiles of harvested 1F5 mAb, digested $F(ab')_2$ and reduced Fab' fragments by ÄKTA FPLC (Superdex 200 HR10/30 column, PBS). Purity of all products from each step were > 95%. (B) SEC profiles of representative $P\text{-}NH_2$ (P1) and P-Fab' (P1-Fab') by ÄKTA FPLC (Superpose 6 HR10/30 column, acetate buffer + 30% acetonitrile v/v).

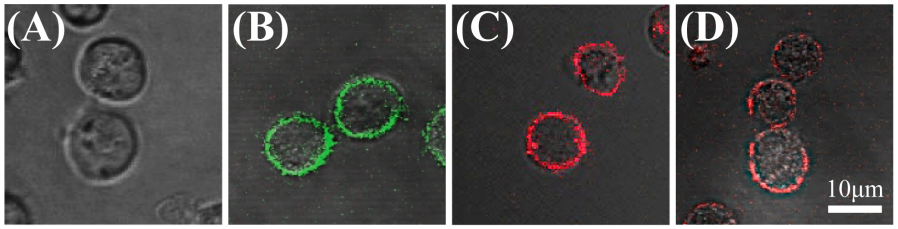

Figure 2.3 Confocal fluorescence microscopic images of Raji B-cells. Cells were exposed to (A) PBS, (B) 1F5 mAb labeled with FITC, (C) $F(ab')_2$ antibody fragment labeled with rhodamine, and (D) P-Fab' conjugate labeled with rhodamine. Raji cells (2.5×10^5) were stained with varying concentrations of each compound for 2 h prior to analysis.

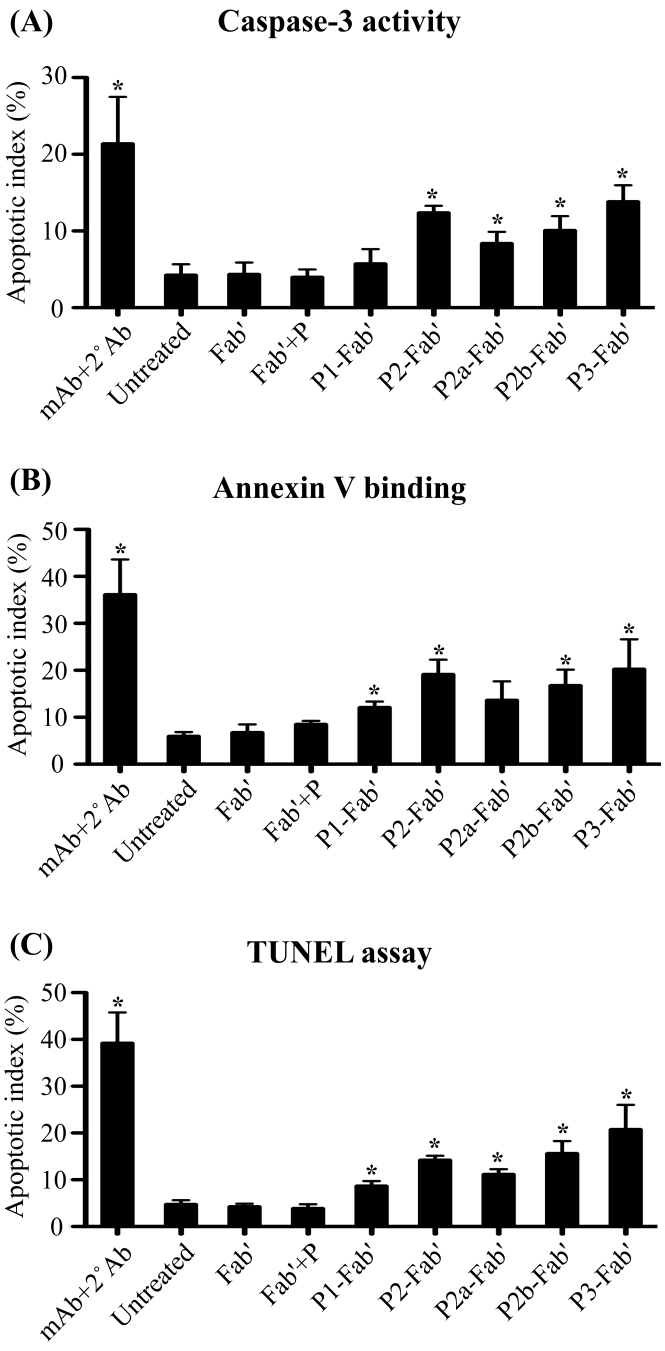

Figure 2.4 Apoptosis induction of Raji B-cells analyzed by (A) caspase-3 activity, (B) annexin V binding, and (C) TUNEL assay. Quantification was performed by flow cytometry. All experiments were carried out in at least triplicate (data shown as mean ± SD). Statistics performed by comparing each group with the untreated (* $p < 0.05$, by Student's *t*-test).

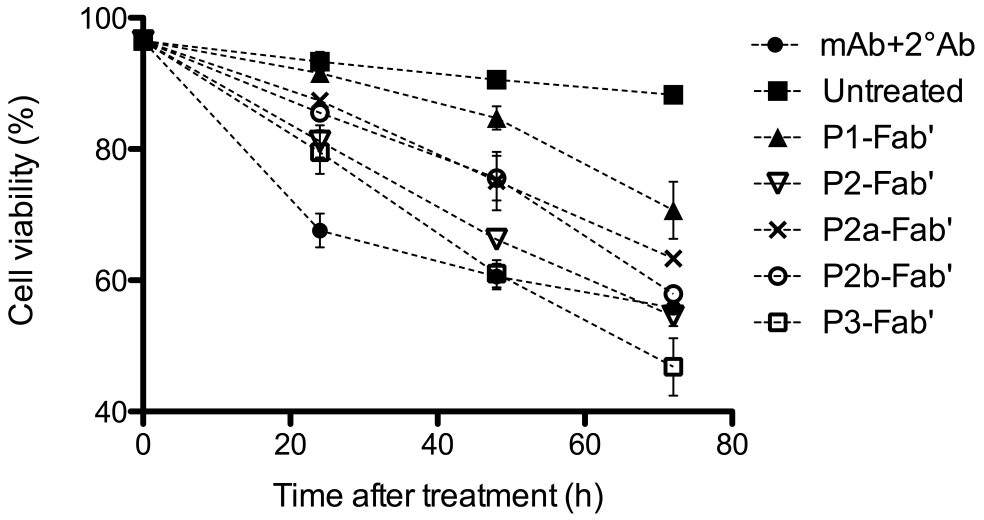

Figure 2.5 Time-dependent cell viability study assessed by PI binding. Treatment conditions were identical to apoptosis assays. Quantification was performed by flow cytometry. Experiments carried out in triplicate (data shown as mean ± SD). (■) Untreated; (•) mAb+2°Ab; (▲) P1-Fab'; (▽) P2-Fab'; (×) P2a-Fab'; (○) P2b-Fab'; (□) P3-Fab'.

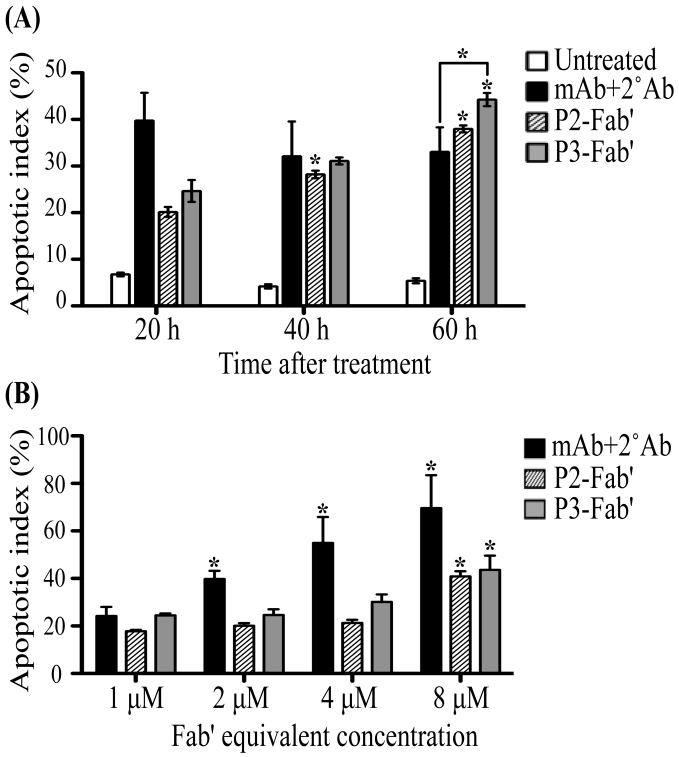

Figure 2.6 Cell apoptosis evaluated by annexin V binding in (A) time-dependent and (B) concentration-dependent assays. All experiments were carried out in triplicate (data shown as mean ± SD). Statistical analyses (unless otherwise indicated) performed by comparing each group with the corresponding shortest time interval or lowest concentration (* $p < 0.05$, by Student's *t*-test).

Table 2.1 Synthesis and characterization of P-NH_2 polymer precursors.

No.	$[M]_0$:$[CTA]_0$:$[I]_0$	Conv.[a] %	Mw (kDa) Theo.[b]	Mw (kDa) SEC[c]	Mw/ Mn	NH_2 mol.% Fed	NH_2 mol.% Found[d]	Structure
P1	800:1:0.33	87.3	102	105	1.09	6	4.31	Non-degradable
P2	1600:1:0.33	89.4	208	207	1.07	6	4.13	Non-degradable
P2a	1600:1:0.33	94.9	219	223	1.04	3	2.12	Non-degradable
P2b*	1600:1:0.25	84.1	197	201	1.11	6	4.23	Degradable
P3	3000:1:0.33	75.7	330	336	1.05	6	4.75	Non-degradable

*Modified CPDB containing enzyme cleavable peptide was used as chain transfer agent (CTA).
[a] Conversion estimated by weight % polymer products.
[b] Theoretical molecular weight of polymer calculated by the following equation:
$Mw_{theo.}$= [($[M]_0$÷$[CTA]_0$) × Conversion × Mean Mw of monomers] + Mw of CTA.
[c] Average molecular weight and polydispersity determined by SEC.
[d] Amine content (NH_2 mol.%) determined by ninhydrin assay.

Table 2.2 Characterization of P-Fab' conjugates.

No.	Valence[a]	Effective Diameter[b] (nm) before conj.	Effective Diameter[b] (nm) after conj.
P1-Fab'	1.7	12.4	36.2
P2-Fab'	3.3	19.1	82.3
P2a-Fab'	1.3	21.1	56.3
P2b-Fab'*	3.4	21.6	74.3
P3-Fab'	11.3	27.4	97.3
Fab'	–	4.5	
P-3Fab3.2†	3.2	30.2	

*Degradable backbone containing GFLG oligopeptide.
† Branched conjugates with polymer Mw=193 kDa.[26]
[a] Fab' per polymer chain as determined by modified AAA.
[b] Determined by DLS (all samples with polydispersity < 0.2).

CHAPTER 3

CELL SURFACE SELF-ASSEMBLY OF HYBRID NANOCONJUGATES *VIA* OLIGONUCLEOTIDE HYBRIDIZATION INDUCES APOPTOSIS[1]

Hybrid nanomaterials composed of synthetic and biological building blocks possess high potential for the design of nanomedicines. The use of self-assembling nanomaterials as "bio-mimics" may trigger cellular events and result in new therapeutic effects. Motivated by this rationale, we designed a therapeutic platform that mimics the mechanism of immune effector cells to crosslink surface receptors of target cells and induce apoptosis. This platform was tested against B-cell lymphomas that highly express the surface antigen CD20. In this chapter, two nanoconjugates were synthesized: (1) an anti-CD20 Fab' fragment covalently linked to a single-stranded morpholino oligonucleotide (MORF1), and (2) a linear, synthetic copolymer of *N*-(2-hydroxypropyl) methacrylamide (HPMA) grafted with multiple copies of the complementary oligonucleotide MORF2. We show that the two conjugates self-assemble *via* MORF1-MORF2 hybridization at the surface of $CD20^+$ malignant B-cells, which crosslinks CD20 antigens and initiates apoptosis. When tested in a murine model of human non-Hodgkin's lymphoma, the two conjugates, either administered consecutively or as a premixture,

[1]This chapter is adapted with permission from: T.-W. Chu, J. Yang, R. Zhang, M. Sima and J. Kopeček. Cell surface self-assembly of hybrid nanoconjugates *via* oligonucleotide hybridization induces apoptosis. *ACS Nano*. 2014; 8(1): 719–730. Copyright (2014) American Chemical Society.

eradicated cancer cells and produced long-term survivors. The designed therapeutics contain no small-molecule cytotoxic compounds and are immune-independent, with the aim of a treatment improved over chemotherapy, radiotherapy and immunotherapy. This therapeutic platform can be applied to crosslink any noninternalizing receptor and potentially treat other diseases.

3.1 Background

Molecular biorecognition is a fundamental feature of life – many biological processes are governed by the complex yet specific interactions between macromolecules, *e.g.*, antibody-antigen binding and DNA base pairing. These high-fidelity recognition motifs from nature can be employed to design self-assembling nanobiomaterials for applications in drug delivery,[1–3] tissue engineering,[4,5] bio-detection,[6–8] *etc*. A new direction of research is to use such precisely defined "smart" materials to incite or control cellular activities;[9–11] in this case the materials alone, without any conventional drug, can provide therapeutic effects. Such biomimetic strategy translates molecular biorecognition into cellular responses to define new therapeutic entities with high functional specificity.

Non-Hodgkin's lymphoma (NHL) is a prevalent cancer worldwide with a high mortality rate.[12] Conventional chemotherapy and radiotherapy are accompanied by significant adverse reactions, particularly cytopenias leading to increased risk of infection and need for transfusions. Because most NHLs are of B-cell origin, immunotherapies using monoclonal antibodies (mAbs) targeted to the B-cell surface antigen CD20 have become common treatments.[13] However, large populations of patients exist who are not

responsive to immunotherapies, especially in the relapse setting. For example, rituximab, the most commonly used anti-CD20 mAb, has a less than 50% overall response rate for relapsed/refractory NHL.[14] This is largely attributed to the inactivity of immune effector cells to hyper-crosslink ligated mAbs.[15,16] Moreover, mAb treatments cause rare but lethal side effects such as progressive multifocal leukoencephalopathy[17] and lung injuries,[18,19] which are due to Fc-mediated effector cellular events (*e.g.*, complement activation).[20] These clinical obstacles warrant new, improved therapeutic strategies.

We designed a biomimetic material platform composed of self-assembling hybrid nanoconjugates (Figure 3.1A) as a therapeutic system against B-cell lymphomas (Figure 3.1B). It comprises an anti-CD20 Fab' antibody fragment, a pair of complementary phosphorodiamidate morpholino oligomers (MORF1 and MORF2), and a linear polymer (P) of *N*-(2-hydroxypropyl)methacrylamide (HPMA). We hypothesized that: (1) the exposure of malignant $CD20^+$ B-cells to the conjugate of anti-CD20 Fab' and MORF1 (**Fab'-MORF1**) decorates the cell surfaces with MORF1; and (2) further treatment of decorated B-cells with HPMA copolymer grafted with multiple copies of MORF2 (**P-MORF2**) results in MORF1-MORF2 hybridization at the cell surface with concomitant CD20 crosslinking, which triggers apoptosis. The proposed mechanism of apoptosis induction is shown in Figure 3.1B.

This design is inspired by the fact that cell surface receptor clustering is a driving force for numerous cellular events, *e.g.*, cell adhesion,[21] cell proliferation,[22] and hormone uptake.[23] In particular, when CD20-bound antibodies are hyper-crosslinked by Fc receptor (FcR)-expressing immune effector cells (*e.g.*, macrophages, natural killer cells), CD20 clustering occurs within lipid rafts and induces apoptosis.[24] We named the

designed platform "drug-free macromolecular therapeutics" due to the absence of low-molecular-weight drugs that are often toxic (*e.g.*, chemotherapeutic agents).[9] Furthermore, each component (Fab', morpholino oligo, HPMA polymer) of this system, when used individually, does not have any pharmacological effect. The apoptosis induction is direct (*i.e.*, independent of immune function) and specific (*i.e.*, targeted to CD20); thus, it has the potential to address the side effect problems of currently used immunotherapy, chemo- and radiotherapy.

The design is based on a pair of morpholino (MORF) oligonucleotides with complementary sequences. They form double helixes by Watson-Crick base pairing (hybridization) and serve as physical crosslinkers. MORF oligos have a charge-neutral phosphorodiamidate backbone resulting in much stronger binding affinity than DNA or RNA.[25] More importantly, they are biocompatible and nuclease resistant; this ensures *in vivo* stability and safety.[26] Due to these advantages, MORF oligos have been successfully used as macromolecular binders to enhance therapeutic delivery.[2,27,28] The HPMA copolymers are water-soluble and long circulating in the bloodstream; they have well-established safety profiles and are used extensively as therapeutic carriers.[29] In aqueous solutions, linear HPMA copolymers have a random coil conformation and are able to effectively present targeting moieties that are grafted to the side chains.[30]

In this chapter, we show the development and preclinical evaluation of the proposed anti-lymphoma nanomedicine. Biorecognition of the two nanoconjugates (Fab'-MORF1 and P-MORF2) was characterized. The therapeutic system was optimized to achieve efficient apoptosis induction of malignant B-cell lines. Excellent anticancer efficacy (100% survival without residual tumors) was demonstrated in a mouse model of

human NHL. These findings validate the concept of the designed therapeutic platform.

3.2 Materials and Methods

3.2.1 MORF1 and MORF2

The two complementary 3'-amine-derivatized 25-mer phosphorodiamidate morpholino oligomers were obtained from Gene Tools, LLC (Philomath, OR). MORF1: 5'-GAGTAAGCCAAGGAGAATCAATATA-linker-amine-3' (MW: 8630.5 Da); MORF2: 5'-TATATTGATTCTCCTTGGCTTACTC-linker-amine-3' (MW: 8438.5 Da). Structure of the linker is shown in Figure 3.2. For the design of base sequences, sequence scrambling software (http://www.sirnawizard.com/scrambled.php) and sequence analysis software (http://www.basic.northwestern.edu/biotools/oligocalc.html) were used.

3.2.2 Preparation of Fab'-MORF1

The 1F5 mAb was prepared from a murine hybridoma cell subclone 1F5 (ATCC, Bethesda, MD) in a CellMax® bioreactor (Spectrum Laboratories, Rancho Dominguez, CA). Antibodies were harvested from the culture media, and purified on a Protein G Sepharose 4 Fast Flow column (GE Healthcare, Piscataway, NJ). Preparation of Fab' from mAb followed a previously reported procedure.[31] Briefly, mAb was digested into $F(ab')_2$ with 10% (w/w) pepsin (Sigma, St. Louis, MO) in citric buffer (pH 4.0). Immediately before conjugation, $F(ab')_2$ was reduced to Fab' by 10 mM tris(2-carboxyethyl)phosphine (Thermo Scientific, Waltham, MA). To prepare the Fab'-MORF1 conjugate, the MORF1 oligo containing a 3'-primary amine was reacted with succinimidyl-4-(*N*-maleimidomethyl)cyclohexane-1-carboxylate (SMCC) to introduce a

terminal (thiol-reactive) maleimide group. This produced MORF1 with 3'-maleimide (MORF1-mal). MORF1-mal was then conjugated to Fab' (containing a terminal thiol group) *via* a thioether bond to obtain Fab'-MORF1. The conjugates were purified using size exclusion chromatography (SEC) to remove free, unconjugated Fab' and MORF1.

A typical procedure was as follows: first, 200 nmol MORF1-NH_2 was reacted with 0.67 mg (2 μmol) SMCC (Soltec Ventures, Beverly, MA) in 170 μL DMSO to produce the MORF1-mal. The reaction was performed at RT (room temperature) for 24 h. The product was isolated by precipitation into 1.5 mL acetone, purified by dissolution-precipitation in deionized water-acetone twice, and dried under vacuum. Second, 200 nmol MORF1-mal was dissolved in 200 μL 10 mM PBS (pH 6.5), and then the solution was mixed with 200 nmol (~10 mg) freshly reduced Fab'-SH in 2 mL PBS (pH 6.5). The reaction was performed at 4 °C for 24 h. Finally, the Fab'-MORF1 conjugate was purified using SEC. An ÄKTA FPLC system (GE Healthcare, Piscataway, NJ) equipped with Sephacryl S-100 HR16/60 column (GE Healthcare) eluted with PBS (pH 7.2) was used. Alternatively, Fab'-MORF1 was labeled with 5–10 molar excess Rhodamine Red™-X succinimidyl ester (R6010) (Molecular Probes®, Invitrogen, Carlsbad, CA) for imaging studies. The product was purified using a PD-10 desalting column (GE Healthcare). To determine Fab' equivalent concentration of the Fab'-MORF1 conjugate, a bicinchoninic acid (BCA) protein assay (Thermo Scientific Pierce, Rockford, IL) was used. The obtained values were compared to the MORF1 equivalent concentrations obtained from UV-visible spectroscopy (using a molar absorptivity of 278,000 M^{-1} cm^{-1}). Such comparison confirmed a 1:1 stoichiometry of the coupling reaction.

3.2.3 Preparation of P-MORF2

The multivalent P-MORF2 conjugates were prepared in two steps. First, the polymer precursors (P-TT), namely, copolymers of *N*-(2-hydroxypropyl)methacrylamide (HPMA), *N*-methacryloylglycylglycine thiazolidine-2-thione (MA-GG-TT), and optionally (for imaging studies only), *N*-methacryloylaminopropyl fluorescein thiourea (MA-FITC), were synthesized by RAFT copolymerization. Second, P-TT was reacted with MORF2-NH_2 to produce the multivalent P-MORF2.

3.2.3.1 Synthesis of P-TT

In the RAFT copolymerization, 2,2'-azobis[2-(2-imidazolin-2-yl)propane] dihydrochloride (VA-044) was used as the initiator, and 4-cyanopentanoic acid dithiobenzoate (CPDB) as the chain transfer agent. CPDB[32] and monomers HPMA,[33] MA-GG-TT,[34] and MA-FITC[35] were synthesized as previously described. The reaction was carried out in methanol containing 0.3% (v/v) acetic acid ($MeOH/H^+$). A typical procedure was as follows: HPMA (272 mg, 1.9 mmol) and MA-GG-TT (30.1 mg, 0.1 mmol) were added into an ampoule attached to an Schlenk-line. After three vaccum-nitrogen cycles to remove oxygen, 1 mL degassed $MeOH/H^+$ was added to dissolve monomers, followed by addition of CPDB solution (0.43 mg in 50 μL $MeOH/H^+$) and VA-044 solution (0.25 mg in 50 μL $MeOH/H^+$) *via* syringe. The mixture was bubbled with nitrogen for 15 min before sealing the ampoule; the copolymerization was performed at 40 °C for 36 h. The copolymer was isolated by precipitation into acetone and purified by dissolution-precipitation in methanol-acetone twice and dried under vacuum. Yield of P-TT was 160 mg (53%). The number average molecular weight (Mn)

and molecular weight distribution (polydispersity, Pd) of P-TT were determined by SEC, using ÄKTA FPLC equipped with miniDAWN and OptilabREX detectors (GE Healthcare). Superose 6 HR10/30 column (GE Healthcare) was used, with sodium acetate buffer (pH 6.5) and 30% acetonitrile (v/v) as mobile phase. To remove the terminal (active) dithiobenzoate groups, P-TT copolymers were reacted with 2,2'-azobis(2,4-dimethyl valeronitrile) (V-65) (Wako Chemicals, Richmond, VA). Briefly, P-TT (39 mg, Mn = 92 kDa, ~0.42 mmol) and V-65 (20× excess, 2.1 mg, ~8.47 mmol) were added into an ampoule. After three vacuum-nitrogen cycles to remove oxygen, 0.4 mL MeOH/H^+ was added. The solution was bubbled with nitrogen for 15 min, sealed and reacted at 50 °C for 3 h. The end-modified copolymer was purified by precipitation into acetone twice and then dried under vacuum (yield 34 mg, or 86%). The content of TT groups in the copolymers was determined by UV absorbance at 305 nm (molar absorptivity = 10,900 M^{-1} cm^{-1}; in methanol).[34] The content of FITC was determined by absorbance at 495 nm (molar absorptivity = 82,000 M^{-1} cm^{-1}; in borate buffer pH 9.2 + 10% (v/v) DMF).[35]

3.2.3.2 Attachment of MORF2-NH_2 to P-TT to Produce P-MORF2

The P-TT described above was reacted with MORF2-NH_2 to produce multivalent P-MORF2. A typical reaction was as follows: 10 mg P-TT (92 kDa; containing 3.83 μmol TT groups) was mixed with 6.46 mg (766 nmol) MORF2-NH_2 in 400 μL 10 mM PBS (pH 7.4). The solution mixture in an ampoule was stirred at RT for 24 h; then 1 μL 1-amino-2-propanol (Sigma-Aldrich, St. Louis, MO) was added and stirred for another 15 min to aminolyze unreacted TT groups on the polymer chains. After reaction, the solution was filtered through a 0.22 μm filter, and the conjugate was purified by SEC using

ÄKTA FPLC with Superose 6 HR16/60 column (GE Healthcare) eluted with PBS (pH 7.2). P-MORF2 was characterized by UV absorbance at 265 nm after removal of unconjugated MORF2 (if any). To quantify the content of MORF2 and determine the valence (number of MORF2 per polymer chain), the fractionated P-MORF2 conjugates were freeze-dried and dissolved in 0.1 N HCl prior to UV-Vis analysis. A molar absorptivity of 252,000 (M^{-1} cm^{-1}) was used for quantification of MORF2. The valences of the P-MORF2 conjugates were calculated based on the resulting MORF2 contents and the Mn of the polymer backbones (as previously determined by SEC).

3.2.4 Analysis of Fab'-MORF1/P-MORF2 Self-Assembly by UV-Visible Spectroscopy and Dynamic Light Scattering (DLS)

Analysis of the hypochromic effect upon MORF1-MORF2 hybridization was performed using a Varian Cary 400 Bio UV-visible spectrophotometer (Agilent Technologies, Santa Clara, CA). MORF1 and MORF2 (or Fab'-MORF1 and P-MORF2) were firstly dissolved in 1 mL PBS (pH 7.4) each at a concentration of 2.5 μM (MORF equivalent) and then mixed in different ratios. The final concentrations of MORF oligos (MORF1 + MORF2) in every solution mixture were kept constant (2.5 μM). For example, the mixture containing 75% MORF1 (or 25% MORF2) was contained in a 0.75 mL of 2.5 μM MORF1 solution and 0.25 mL of 2.5 μM MORF2 solution. Samples were placed in a 1-cm quartz cuvette for measurement. The optical density (OD) at 260 nm (contributed by bases) was recorded. All measurements were performed in triplicate.

The hydrodynamic effective diameters of the conjugates, Fab'-MORF1 and P-MORF2, and their precursors, Fab'-SH and P-TT, were analyzed by DLS (dynamic light

scattering) using a Brookhaven BI-200SM goniometer and BI-9000AT digital correlator equipped with a He-Ne laser (λ = 633 nm) at RT in PBS (pH 7.4). The scattering angle was 90°. A Nanosphere™ polystyrene bead with a standard diameter of 102 ± 3 nm (STD100nm) (Thermo Scientific, Waltham, MA) was used to measure in line. Conjugates and precursors at a concentration of about 1 mg/mL were filtered through a 0.22 μm filter prior to measurement. All samples showed a polydispersity less than 0.2, and the mean particle diameters were recorded. Furthermore, DLS was used to characterize the change of particle size upon the binding of Fab'-MORF1 and P-MORF2. The analysis was performed at different times (10, 30 and 60 min) after mixing the two conjugates (at equimolar MORF1/MORF2 concentrations). All samples contained a major population of particles (polydispersity < 0.2) indicating the hybridized conjugates, as well as minor populations indicating unbound Fab'-MORF1 and P-MORF2. The mean effective diameter of the major population was recorded. All measurements were performed in triplicate.

3.2.5 Circular Dichroism (CD) Spectrometry

An Aviv 62DS CD spectrometer with a thermoelectric temperature control system (Aviv Biomedical, Lakewood, NJ) was used. Regular measurements (excluding thermal melting analysis) were carried out at 25 °C where each sample was scanned from 200 to 340 nm with 1 nm/step (bandwidth = 1 nm, each step = 2 sec). Samples were prepared in 10 mM PBS (pH 7.4) at 50 μM MORF equivalent concentrations (Fab'-SH at 50 μM Fab'-eqv.). Prior to measurement, samples were filtered through a 0.22 μm filter and placed in a 0.1-cm path length quartz cuvette. The obtained spectra were subtracted from

the background (PBS, pH 7.4); data from three sequential scans were averaged. For thermal melting studies, the CD signal at 260 nm was recorded (n = 3). Fab'-MORF1 and P-MORF2 (or MORF1 and MORF2) were mixed in equimolar ratio (5 μM/5 μM MORF1/MORF2) in PBS for 1 h at RT. The solution mixtures were filtered and placed in a 1-cm path length quartz cuvette prior to measurement. Each sample first underwent a forward scan where the temperature increased from 25 to 95 °C at 2 °C/step. For each step, the sample was equilibrated for 2 min followed by 30 sec of data point averaging. Afterward, a reverse scan was performed where the temperature decreased from 95 to 25 °C at -10 °C/step. For each step, the sample was equilibrated for 5 min followed by 30 sec of data point averaging.

The measured ellipticity (θ_{obs}) was converted to molar ellipticity (θ) using the following equation: $\theta = \theta obs/(l * c)$ where l is the cuvette's optical path length and c is MORF-equivalent molar concentration. To analyze melting temperature (Tm) of MORF1-MORF2 hybridization, θ (at 260 nm) was plotted against temperature (T), and the data were fitted to a thermo-melting curve by nonlinear regression (GraphPad Prism 5 software) using the following four-parameter logistic function:

$$\theta = \theta min + (\theta max - \theta min)/[1 + (T/Tm)\text{^}H\ ]$$

where θ_{min} is the minimal molar ellipticity (at 260 nm) in the curve, θ_{max} is the maximal molar ellipticity (at 260 nm) in the curve, and H is the Hill slope.

3.2.6 Confocal Fluorescence Microscopy

Human Burkitt's B-cell non-Hodgkin's lymphoma Raji cell line (ATCC, Bethesda, MD) was cultured in RPMI-1640 medium (Sigma, St. Louis, MO)

supplemented with 10% fetal bovine serum (Hyclone, Logan, UT) at 37 °C in a humidified atmosphere with 5% CO_2 (v/v). All experiments were performed using cells in exponential growth phase. For the consecutive treatment, cells at a density of 10^6 per well were incubated with 0.4 mL Fab'-MORF1-RHO (0.4 μM Fab' equivalent) in culture medium at 37 °C for 1 h; then the cells were washed twice with PBS prior to incubation with 0.4 mL of P-MORF2-FITC (0.4 μM MORF2 equivalent) in culture medium for another 1 h. For the premixed treatment, Fab'-MORF1-RHO and P-MORF2-FITC were firstly mixed in culture medium in equimolar concentrations (0.4 μM) for 1 h; then cells at the same density were incubated with 0.4 mL of the premixture solution for 1 h. After incubation, the cells were washed twice with PBS (to discard the media that contained the conjugates), and then plated onto sterile 35-mm glass bottom dishes with 14-mm microwells (MatTek Corporation, Ashland, MA) for imaging, using Olympus laser scanning confocal microscope (FV 1000). For control studies, concentrations of all corresponding components were kept consistent; excess amounts of P-FITC and P-dsMORF were used. Prior to analysis, cells incubated with FITC-labeled 1F5 mAb, rhodamine-labeled $F(ab')_2$, and PBS were used to adjust channel setting and confirm CD20 binding.

3.2.7 *In Vitro* Apoptosis Evaluation

Apoptosis of human NHL B-cells was evaluated by three methods: caspase-3 activation assay, annexin V/propidium iodide (PI) binding assay, and terminal deoxynucleotide mediated-dUTP nick-end labeling (TUNEL) assay. These assays evaluated apoptosis from different aspects – levels of caspase-3 activation represented

apoptotic protein expression; annexin V/PI binding characterized cell membrane flipping as an early apoptotic event; TUNEL assay analyzed genomic DNA fragmentation as a late apoptotic event. Quantification of apoptotic activity (% apoptotic cells) was performed by flow cytometry. In all experiments, 1F5 mAb hyper-crosslinked with a goat antimouse (GAM) secondary antibody (2° Ab) (KPL, Gaithersburg, MD) was used as a positive control (molar ratio 1F5:GAM = 2:1). Untreated cells (in culture media) were used as negative controls. The procedures of each assay are described below.

3.2.7.1 Caspase-3 Activity

A Phi-PhiLux kit (OncoImmunin, Gaithersburg, MD) was used. For the consecutive treatment, 2×10^5 Raji cells were suspended in 0.4 mL fresh growth medium containing 0.5 μM Fab'-MORF1. The cells were incubated for 1 h in a humidified atmosphere at 37 °C with 5% CO_2, and then washed twice with PBS + 1% bovine serum albumin (BSA), followed by resuspension in 0.4 mL medium containing 0.5 or 5 μM (MORF2-eqv.) P-MORF2. The cell suspension was incubated for 6 or 24 h. For the premixed treatment, first, 0.5 μM Fab'-MORF1 was mixed with 0.5 or 5 μM (MORF2-eqv.) P-MORF2 in culture medium at RT for 1 h, and then 2×10^5 Raji cells were suspended in 0.4 mL of the premixed solution. The cell suspension was incubated for 6 or 24 h. For the positive control, cells were firstly incubated with 0.4 mL 0.5 μM of 1F5 mAb in culture medium for 1 h, and then washed twice with PBS + 1% BSA, followed by resuspension in 0.4 mL of fresh growth medium containing 0.25 μM GAM. The cells were incubated for another 6 or 24 h at 37 °C. After the treatments, cells were washed twice with PBS and analyzed for caspase-3 activity following the manufacturer's

protocol. All experiments were carried out in triplicate.

3.2.7.2 Annexin V/PI Binding

Annexin V-FITC and PI staining were performed following the RAPID™ protocol provided by the manufacturer (Oncogene Research Products, Boston, MA). For the consecutive treatment, 2×10^5 Raji or DG75 (CD20 negative; control) cells were suspended in 0.4 mL fresh growth medium containing 0.5, 1, 2 or 5 μM Fab'-MORF1. The cells were incubated for 1 h in a humidified atmosphere at 37 °C with 5% CO_2, and then washed twice with PBS + 1% bovine serum albumin (BSA), followed by resuspension in 0.4 mL culture medium containing 0.5, 1, 2 or 5 μM (MORF2-eqv.) of P-MORF2. The cell suspension was incubated for 24 or 48 h. For the premixed treatment, first, 0.5, 1, 2 or 5 μM Fab'-MORF1 was mixed with 0.5, 1, 2 or 5 μM (MORF2-eqv.) P-MORF2 in culture medium at RT for 1 h, and then 2×10^5 Raji or DG75 cells were suspended in 0.4 mL of the premixed solution. The cell suspension was incubated for 24 or 48 h. For the positive control, cells were firstly incubated with 0.4 mL 0.5, 1, 2 or 5 μM of 1F5 mAb in culture medium for 1 h, and then washed twice with PBS + 1% BSA, followed by resuspension in 0.4 mL of fresh growth medium containing 0.25, 0.5, 1 or 2.5 μM GAM. The cells were incubated for another 24 or 48 h at 37 °C. Prior to staining, cells were washed twice with PBS. All experiments were carried out in triplicate.

3.2.7.3 TUNEL Assay

An Apo Direct TUNEL kit (Phoenix Flow Systems, San Diego, CA) was used. For the consecutive treatment, 10^6 Raji cells were suspended in 0.5 mL fresh growth

medium containing 0.5 μM Fab'-MORF1. The cells were incubated for 1 h in a humidified atmosphere at 37 °C with 5% CO_2, and then washed twice with PBS + 1% bovine serum albumin (BSA), followed by resuspension in 0.5 mL medium containing 0.5 or 5 μM (MORF2-eqv.) P-MORF2. The cell suspension was incubated for 24 or 48 h. For the premixed treatment, first, 0.5 μM Fab'-MORF1 was mixed with 0.5 or 5 μM (MORF2-eqv.) P-MORF2 in culture medium at RT for 1 h, and then 10^6 Raji cells were suspended in 0.5 mL of the premixed solution. The cell suspension was incubated for 24 or 48 h. For the positive control, cells were firstly incubated with 0.5 mL 0.5 μM of 1F5 mAb in culture medium for 1 h, and then washed twice with PBS + 1% BSA, followed by resuspension in 0.5 mL of fresh growth medium containing 0.25 μM GAM. The cells were incubated for another 24 or 48 h at 37 °C. After the treatments, cells were washed twice with PBS and fixed with 2% paraformaldehyde in PBS for 1 h at RT. Cells were then permeabilized in 70% ethanol overnight at 4 °C. Prior to analysis, nick-end labeling was performed following the manufacturer's protocol. All experiments were carried out in triplicate.

3.2.8 Animal Model and Evaluation of *In Vivo* Anticancer Efficacy

Female C.B-17 SCID mice (Charles River Laboratories, Wilmington, MA) at about 7 weeks of age were intravenously injected with 4×10^6 Raji cells in 200 μL saline *via* the tail vein (day 0). This animal model represents dissemination, infiltration and growth of lymphoma cells in various organs, including the spinal cord which leads to hind-limb paralysis and subsequent animal death.[36–38] The conjugates, Fab'-MORF1 (57.5 μg/20 g; 1 nmol MORF1) and P-MORF2/v10 (22 μg/20 g; 1 nmol MORF2), were

dissolved in 100 μL PBS and injected *via* tail vein either consecutively (1-h interval) or as a premixture (mixed 1 h prior to treatment). The inoculated mice were divided into seven groups: (1) negative control (injected with 200 μL PBS), (2) single administration of the consecutive treatment (Cons ×1), (3) single administration of the premixed treatment (Prem ×1), (4) consecutive treatment administered three times (Cons ×3), (5) premixed treatment administered three times (Prem ×3), (6) single administration of the consecutive treatment but with 5× excess P-MORF2/v10 (110 μg/20 g; 5 nmol MORF2) to Fab'-MORF1 (Cons (1:5) ×1), and (7) positive control injected with three doses (75 μg/20 g; 1 nmol Fab'-equivalent per dose) of 1F5 mAb *via* tail vein. For single-dose groups, conjugates were administered on day 1 (24 h after injection of cancer cells); for multiple-dose groups, conjugates (or mAb) were given on days 1, 3 and 5.

Posttreatment monitoring of the animals was performed twice a day. Body weight of mice was recorded every other day. Major aspects of the mice closely assessed included: hind-limb paralysis, food/water consumption, vital signs of abnormal mobility/activity (*e.g.*, licking, biting, scratching a particular area, vocalizing), and physical appearance (*e.g.*, failure to groom, unkept appearance, abnormal resting/hunched posters, piloerection). Animals were sacrificed in the following scenarios (whichever showed up first): (1) at the onset of (hind-limb) paralysis, and (2) body weight loss exceeding 20% of the baseline (one day before the injection of cancer cells). Animals without any aforementioned signs were kept until 125 days (after the injection of cancer cells) and sacrificed for further analysis. These procedures adhered to the Institutional Animal Care and Use Committee (IACUC) protocol #12-11004 of the University of Utah. Animals without signs of paralysis/sickness were kept until 125 days and

considered long-term survivors.

3.2.9 Magnetic Resonance Imaging (MRI) of Mice

To monitor disease progression and treatment efficacy, mice (2–4 per group) were scanned by T_1-weighted MRI on weeks 4, 5, and 16 after tumor inoculation. Gadobenate dimeglumine (MultiHance®; Bracco SpA, Milan, Italy) was used as a contrast agent for imaging. Precontrast images were also acquired (for comparison). A typical procedure was as follows: first, mice were anesthetized with 1%–2.5% isoflurane (IsoFlo®, Abbott Laboratories, Abbott Park, IL) in oxygen from a precision vaporizer, and then mice were placed in the prone position at the coil center. A 7-Tesla Bruker BioSpec MRI scanner (Bruker Biospin, Billerica, MA) with a 30-cm wide cylindrical bore and a 12-cm gradient insert was used. Precontrast images were firstly acquired, and then mice were injected with gadobenate dimeglumine *via* tail vein at 0.3 mmol/kg (100 μL, in physiological saline). Twenty minutes after the injection, postcontrast images were acquired. During the scanning, mouse body temperature was maintained at 37 °C using a warm-air circulation system (SA Instruments, Stony Brook, NY). Respiration was monitored continuously. Scanning was performed under the ParaVision® 5.1 software environment. Acquisition parameters were as follows: T_1-weighted FLASH sequence with retrospective gating to suppress breathing artifacts, echo time (TE) 2.9 ms, repetition time (TR) 43.2 ms, flip angle 50°, 6 sagittal plane slice with thickness 0.5 mm, matrix 256 × 256, field-of-view (FOV) 3 cm × 3 cm, 50 repetitions. After the scanning, images were analyzed and processed on an off-line workstation (OsiriX).

3.2.10 Flow Cytometry Analysis of Residual Raji Cells

After mice were sacrificed, the following organs/tissues were analyzed by flow cytometry for residual Raji cells: bone marrow (femur), mesenteric and inguinal lymph nodes, spinal cord, and spleen. Two fluorescently labeled antibodies, R-phycoerythrin (PE)-labeled mouse anti-human CD10 (IgG1, κ isotype) and allophycocyanin (APC)-labeled mouse anti-human CD19 (IgG1, κ isotype) (BD Biosciences, San Jose, CA), were used to stain Raji B-cells.[39] Single-cell suspensions were prepared from the organs/tissues using the following procedures. For bone marrow, fresh femurs were purged with 1 mL PBS to obtain cell suspensions. Cells were resuspended in 5 mL red blood cell (RBC) lysis buffer and incubated at RT for 5 min. Cells were then washed with 5 mL PBS and centrifuged to remove debris, followed by resuspension in 400 μL cold washing buffer and equally divided into four tubes: (1) nonstained control, (2) CD10 singly-stained, (3) CD19 singly-stained, and (4) CD10/CD19 doubly-stained cells. For the staining, 20 μL of each antibody was added to 100 μL cell suspension containing about 10^6 cells. Cells were incubated for 30 min at 4 °C in the dark, and washed with 1.5 mL washing buffer prior to analysis. For lymph nodes, spinal cord and spleen, a mechanical method was used. Tissues were gently disaggregated with the help of tweezers in a Petri dish containing 1 mL PBS. The suspensions were passed through a 70-μm Falcon™ cell strainer (BD Biosciences) to remove large clumps and debris, and then cells were centrifuged and resuspended in 5 mL RBC lysis buffer. The rest of the procedures were the same as aforementioned. For flow cytometry analysis, data of $1.0–1.5 \times 10^5$ cells were recorded.

3.2.11 Pathological and Histopathological Examinations

Immediately after mice were sacrificed, the following organs/tissues were harvested for pathological evaluation: brain, heart, lung, liver, spleen, kidneys, spinal cord and lymph nodes. These organs/tissues were fixed in 10% formalin overnight at RT, and then transferred and preserved in 70% ethanol. Histopathological examination was performed by a blinded veterinary pathologist at ARUP Laboratories (Salt Lake City, UT). Sections were cut at 4-μm thickness, mounted on glass slides, and stained by hematoxylin and eosin (H&E).

3.2.12 Statistical Analysis

All experiments in this study were at least triplicated. Quantified data were presented as mean ± standard deviation (SD). Statistical analyses were performed by Student's *t*-test to compare between two groups, or one-way analysis of variance (ANOVA) to compare three or more groups (with p value < 0.05 indicating statistically significant difference). Animal survival analysis was performed with the log-rank test using the GraphPad Prism 5 software.

3.3 Results and Discussion

To verify the concept of hybridization-mediated drug-free macromolecular therapeutics, we selected CD20 as a pharmacological target. CD20 is a noninternalizing receptor expressed on most NHL malignant B-cells as well as on normal B-cells.[40] However, it is not expressed on plasma cells (effector B-cells) and stem cells. Consequently, humoral immunity of patients is not severely affected, and normal

numbers of B-cells can be restored after treatment.[41,42] Here, we employed an anti-CD20 Fab' fragment in the therapeutic system and used NHL as a disease model to demonstrate the first example of the designed platform.

3.3.1 Design of MORF1 and MORF2

The MORF oligos used in this study were 25 bp and about 8.5 kDa (see structure in Figure 3.2 and base sequence in *Subsection 3.2.1*). Their 3' termini were modified with a primary amine used for conjugation. The A/T/C/G content was selected to achieve optimal binding efficacy and specificity (GC = 35–65%),[26] maintain aqueous solubility (G < 36%),[26] and potentially provide favorable pharmacokinetics (number of C < 7 to avoid rapid kidney uptake).[27] After the base composition was determined, the sequences were generated by a scrambling software to minimize off-target binding with human and murine mRNA and further optimized to prevent self-complementarity.

3.3.2 Synthesis and Characterization of Fab'-MORF1 and P-MORF2

To prepare the Fab'-MORF1 conjugate (Figure 3.2A), the Fab' fragment from a mouse anti-human CD20 IgG2a mAb (1F5)[43] was tethered to the 3' end of MORF1 *via* a thioether bond. Optionally, the conjugates were labeled with rhodamine (RHO) for imaging studies. Fab'-MORF1 was successfully synthesized as confirmed by HPLC (Figure 3.2B) and size exclusion chromatography (SEC) (Figure 3.3A); the coupling reaction followed a 1:1 stoichiometry as characterized by MALDI-ToF mass spectrometry (Figure 3.3B) and UV-visible spectroscopy (Figure 3.3C). The molecular weight (MW) of Fab'-MORF1 was about 57.5 kDa.

To prepare the multivalent P-MORF2 conjugates (Figure 3.2C), we first synthesized HPMA copolymers containing glycyl-glycine (GG; spacer) side-chains terminated in (amine-reactive) thiazolidine-2-thione (TT) groups. These polymer precursors (P-TT) were synthesized by reversible addition-fragmentation chain transfer (RAFT) polymerization. A polymerizable fluorescein isothiocyanate (FITC) derivative was optionally added for imaging studies. Using RAFT polymerization, polymer backbones with narrow MW distribution (polydispersity index ≤ 1.15, as determined by SEC) were reproducibly synthesized. Furthermore, the amine-derivatized MORF2 oligos (MORF2-NH_2) were grafted *via* stable amide linkage to the side chains of the HPMA copolymers to produce multivalent P-MORF2. The conjugates were purified and characterized by SEC (Figure 3.2D). Three different P-MORF2's with varying backbone MW and valences (number of MORF2 per polymer chain) were synthesized; see Figure 3.4 for details. The backbone number average molecular weights (Mn) of these conjugates ranged from 70 to 136 kDa. Valences of the three P-MORF2 conjugates were 2, 3 and 10, respectively.

3.3.3 *In Vitro* Hybridization of Fab'-MORF1 and P-MORF2

Hybridization of the two conjugates *via* MORF1-MORF2 biorecognition was first evaluated by UV-visible spectroscopy. The two conjugates were mixed in different ratios, and the optical density at 260 nm (contributed by bases) was measured. Upon mixing Fab'-MORF1 and P-MORF2, a "hypochromic effect" was observed (Figure 3.5A); the $OD_{260\,nm}$ reached a minimum when a molar ratio of 1:1 (MORF1:MORF2) was used. Such decrease was due to hydrogen bonding between complementary bases that limited

the resonance of the aromatic rings. This method was also used to determine hybridization of the free, unconjugated MORF1 and MORF2, and the same hypochromicity was observed. These results indicated that the function of MORF1-MORF2 hybridization was preserved after conjugation to Fab' or polymers.

Furthermore, the binding of Fab'-MORF1 and P-MORF2 was characterized by dynamic light scattering (DLS) (Figure 3.5B). As shown in Figure 3.5B, a significant and rapid increase of hydrodynamic size upon mixing the two conjugates (at equimolar MORF1/MORF2) was revealed. The fast attainment of stable diameter (~40 nm) reflected a fast binding kinetics (< 10 min) of MORF1-MORF2 hybridization of the conjugates. Such rapid binding is in agreement with the literature; for example, Mang'era *et al.* reported that a pair of 15-mer complementary MORF oligomers reached near-maximal binding within 2–5 min.[28] This characteristic is favorable for the design of drug-free macromolecular therapeutics.

Circular dichroism (CD) spectroscopy was used to determine the melting temperature (Tm) of the Fab'-MORF1/P-MORF2 complex in physiological conditions (PBS pH 7.4) (Figure 3.5C). First, a pronounced optical signature (maximum at 260 nm, minimum at 210 nm) indicating A-form double helixes[44] was obtained upon mixing the two conjugates; a similar CD profile was observed when unconjugated MORF1 and MORF2 were mixed (Figure 3.6). Second, a thermal melting study was performed to analyze the mixture of Fab'-MORF1 and P-MORF2. Data showed that the aforementioned CD signature no longer existed at 95 °C; the positive band at 260 nm underwent a significant bathochromic shift that produced a peak centered around 275 nm (Figure 3.7). The thermo-melting curves shown in Figures 3.5C and 3.7B demonstrate

that the signal at 260 nm decreased in a sigmoidal pattern as temperature increased. Results of nonlinear regression indicated a Tm value of about 57 to 62 °C. The Tm is well above body temperature, suggesting *in vivo* stability of the binding.

3.3.4 Biorecognition of Fab'-MORF1 and P-MORF2 at B-Cell Surface

Human B-cell lymphoma Raji cell line ($CD20^+$)[40,45] was used to study the biorecognition of Fab'-MORF1 and P-MORF2 at the cell surface. This study was performed by confocal fluorescence microscopy. First, exposure of Raji cells to rhodamine-labeled Fab'-MORF1 resulted in cell surface red signal (RHO) decoration due to Fab'-MORF1 binding to CD20; cells exposed to only FITC-labeled P-MORF2 did not show any fluorescent signal (Figure 3.8A). Second, when Raji cells were exposed to both fluorescently labeled conjugates (Fab'-MORF1 + P-MORF2), either consecutively or as a premixture, the red and the green (FITC) signals were well colocalized at the surfaces of B-cells (Figure 3.8B). This observation indicated successful MORF1-MORF2 hybridization at the cell surface. Figure 3.8C shows the microscopic images obtained from two control groups: (1) cells exposed to the premixture of Fab'-MORF1(-RHO) and an HPMA copolymer carrying FITC dye but without MORF2 (P-FITC); (2) a "preblocking" control achieved by exposing cells consecutively to Fab'-MORF1(-RHO) followed by a mixture of P-MORF2(-FITC) with an excess of unconjugated MORF1 (this produced HPMA copolymers grafted with double-stranded MORF; P-dsMORF). As expected, both control treatments resulted in only the red signal at cell surfaces (Figure 3.8C) due to absence of a biorecognition pair. Results of these controls confirmed that the cell surface biorecognition of Fab'-MORF1 and P-MORF2 was indeed mediated by

MORF1-MORF2 hybridization.

3.3.5 Apoptosis Induction of Human NHL B-Cells

Apoptosis induction of human B-cell lines (Raji and DG75) was evaluated by three methods: caspase-3 activation assay, annexin V/propidium iodide (PI) binding assay, and terminal deoxynucleotidyl transferase dUTP nick end-labeling (TUNEL) assay. Throughout these studies, anti-CD20 1F5 mAb hyper-crosslinked with a goat anti-mouse secondary Ab (2° Ab) was used as a positive control to imitate the function of FcR^+ immune effector cells.[45] This control partly reflects the therapeutic efficacy of anti-CD20 mAbs. Results showed that cotreatment with Fab'-MORF1 and P-MORF2, either consecutively or as a premixture, effectively induced apoptosis of Raji B-cells (Figure 3.9). In contrast, single-component treatments with either Fab'-MORF1 or P-MORF2 failed to initiate apoptosis. A series of control experiments validated the hypothesis that MORF1-MORF2 hybridization with concomitant crosslinking of CD20 antigens is responsible for the apoptosis induction. Raji cells were exposed to: (1) a mixture of Fab'-MORF1 and the polymer precursor P-TT; (2) a mixture of Fab' and P-MORF2; (3) "preblocked" conjugates whose MORF1 or MORF2 binding sites were blocked by excess unconjugated complementary MORFs prior to treatment. None of these treatments induced apoptosis (Figure 3.10A), due to absence of MORF1-MORF2 hybridization. Furthermore, the apoptosis of a negative control B-cell line (DG75) that does not (or minimally) express CD20 was evaluated.[46] The levels of apoptosis after cotreatment with two conjugates were very low, and similar to that of the untreated cells (Figure 3.10B). This result indicated that CD20 binding is a necessary event for apoptosis induction.

3.3.6 Optimization of Apoptosis Induction

To optimize the therapeutic system, several factors and their impact on apoptosis of Raji B-cells were examined, including concentration of conjugates, ratio between two conjugates, valence of P-MORF2, and exposure time. We started with a P-MORF2 containing about 3 oligos per polymer chain (P-MORF2/v3). Results of annexin V/PI staining assay indicated that 1 μM Fab'-MORF1 and equimolar P-MORF2/v3 (MORF1:MORF2 = 1:1) induced about 40% of apoptotic cells (more than 4 fold compared to untreated) (Figure 3.9A). When all conditions were kept identical except different concentrations of Fab'-MORF1 (and corresponding P-MORF2/v3), a concentration-dependent apoptosis induction was observed (Figure 3.9B). Data suggested that increasing concentrations of the conjugates from 0.5 μM to 2 and 5 μM (Fab' equivalent) resulted in higher levels of apoptosis. The dose-dependent trends were observed in both consecutive and premixed treatment regimens as well as in the positive control (mAb + 2° Ab). At the highest concentration tested (5 μM), apoptosis induction by drug-free macromolecular therapeutics (Fab'-MORF1 + P-MORF2/v3) reached about 7 fold compared to untreated controls. In addition, the percentage of the apoptotic cells induced by mAb + 2° Ab seemed to saturate when the concentration of 1F5 mAb was increased from 2 to 5 μM; however, such saturation was not observed in the nanomedicine groups. This difference was likely due to P-MORF2 having multimeric interactions with targets, in contrast to mAbs with only two binding sites.

Furthermore, we examined the influence of the valence of P-MORF2 and the ratio between Fab'-MORF1 and P-MORF2 on apoptosis induction of Raji B-cells. A “high-valence” P-MORF2 containing 10 oligos per chain (P-MORF2/v10) was compared with

P-MORF2/v3 (3 oligos per chain). Results showed that when all treatment conditions were identical (0.5 μM Fab', MORF1:MORF2 = 1:1 or 1:10), the P-MORF2/v10 conjugate induced about 2-fold higher levels of apoptosis compared to P-MORF2/v3 (Figure 3.9C). It is noteworthy that the consecutive treatment of Fab'-MORF1 and P-MORF2/v10 induced apoptosis more effectively than the positive control (consecutive treatment of mAb and 2° Ab). The superior apoptosis induction observed here was likely due to multivalency of P-MORF2/v10 resulting in higher avidity to B-cells, as well as more effective CD20 clustering.[47–49] Interestingly, when Raji cells were exposed to the same concentration of Fab'-MORF1 (0.5 μM), whereas a 10-time excess P-MORF2 was used (MORF1:MORF2 = 1:10), we did not observe significantly enhanced apoptotic levels compared to the treatment with equimolar MORF1/MORF2 (Figure 3.9C). Apparently, the MORF1 binding sites on the surfaces of the Fab'-MORF1-decorated cells were saturated, which suggests good accessibility of MORFs on the polymer chain for hybridization (minimal steric hindrance effect by the polymer chain). The same trends of apoptosis induction were observed at different exposure times (6, 24 and 48 h) and from different apoptosis assays (caspase-3, annexin V/PI, TUNEL).

3.3.7 Preclinical Evaluation in a Murine Model of Human NHL

In vivo therapeutic efficacy of the hybridization-mediated drug-free macromolecular therapeutics was evaluated in SCID (C.B-17) mice bearing systemically disseminated Raji B-cells. This animal model has a near 100% tumor engraftment rate,[36] and the hind-limb paralysis-free survival time after treatment accurately reflects anticancer efficacy.[37,38] The conjugates, Fab'-MORF1 and P-MORF2/v10, were injected

via the tail vein of mice either consecutively or as a premixture. Mice divided into different groups (n = 6–7) received either one or three doses of the nanomedicine, starting at 24 h after tumor injection. Doses and treatment regimens were based on literature[37,38] and our previous study with peptide conjugates.[50] The animal survival curve is shown in Figure 3.11. The negative control mice treated with PBS (n = 8) developed hind-limb paralysis in 17–35 days after injection of cancer cells; the median survival time was 24 days. This observation was in agreement with the literature.[38,50] A single administration of the consecutive treatment (Cons ×1; MORF1:MORF2 = 1:1) substantially extended the animal survival (median survival time: 81 days). A single premixed dose (Prem ×1; MORF1:MORF2 = 1:1) had similar efficacy as the consecutive treatment, resulting in a median survival of 78 days. When the same dose of Fab'-MORF1 (57.5 μg/20 g) was given but followed by 5-times the excess P-MORF2/v10 (MORF1:MORF2 = 1:5), the efficacy significantly improved over the treatment with equimolar MORF1/MORF2. A single administration of such treatment (Cons (1:5) ×1) produced a 67% survival rate (4/6 long-term survivors; 125 days). The discrepancy between *in vivo* and *in vitro* data (Figure 3.9C), when excess P-MORF2 was used, can be explained by blood dilution of the conjugates, which interferes with binding saturation.

Excellent therapeutic efficacy was observed with the groups of mice that received three consecutive administration doses (Cons ×3; n = 7) or three premixed administration doses (Prem ×3; n = 7). All mice survived until the experimental endpoint (day 125). The positive control group (n = 7) that received three equivalent doses of 1F5 mAb (i.v.) had an 86% survival rate. Although the difference to the three-dose nanomedicine groups is not statistically significant, the anticancer activity of the nanomedicine, unlike mAbs, is

independent of immune effector mechanisms such as antibody-dependent cellular cytotoxicity (ADCC) and complement-dependent cytotoxicity (CDC).[45] These data indicated that the direct apoptosis induction strategy can be as effective as the immunotherapy while simultaneously reducing the concerns of side effects that are mostly associated with ADCC and CDC.[20,51] The preclinical evaluation here demonstrated the *in vivo* anticancer efficacy of the hybridization-mediated drug-free macromolecular therapeutics and suggested that the therapeutic efficacy can be further improved by increasing the number of treatments and/or the dose of the second, therapeutically active conjugate (P-MORF2).

3.3.8 Analysis of *In Vivo* Anti-Lymphoma Efficacy

Using the above-mentioned animal model, eradication of Raji cells in SCID mice after treatment with Fab'-MORF1 and P-MORF2 was confirmed by MRI, flow cytometry and histology. MRI with gadolinium-based contrast at 4–5 weeks after injection of cancer cells showed that the control mice treated with PBS developed tumors in the lumbar spinal cord, whereas three doses of the nanomedicine prevented tumor development (Figure 3.12A). The surviving mice treated with Cons ×3 or Prem ×3 were imaged again on week-16; no relapse of the disease was observed. After the mice were sacrificed, flow cytometry was performed to analyze residual Raji cells (human $CD10^+$ $CD19^+$) in the femoral bone marrow (Figure 3.12B). Two fluorescently labeled antibodies, PE-labeled mouse anti-human CD10 and APC-labeled mouse anti-human CD19, were used for flow cytometry analysis.[39] Results indicated that the paralyzed animals (PBS-treated) bore significant amounts of Raji cells in the bone marrow, while all long-term survivors in the

therapy groups (Cons ×3 and Prem ×3) were tumor free (Figure 3.12C). Flow cytometry also confirmed Raji cells in the spinal cord of paralyzed mice (PBS-treated), but not in the long-term survivors (Figure 3.13), which was in agreement with MRI data. Furthermore, histological examination disclosed lymphoma dissemination in the liver, lung and brain of PBS-treated mice (Figure 3.14). In contrast, no tumors were found in the long-term survivors. Importantly, histology suggested no toxicity caused by the treatments in any of the tissues evaluated; this corresponded to a stable body weight growth of the treated animals. In conjunction these results indicated that the nanomedicine successfully inhibited lymphoma cell growth/dissemination *in vivo* without acute toxicity.

3.4 Summary

Data presented here validate the proposed concept of hybridization-mediated cell surface antigen crosslinking and apoptosis induction. A unique bio-inspired nanomaterial system has been demonstrated where extracellular hybridization of oligonucleotide analogues translates into innate biological responses. The cellular event (apoptosis) is triggered by specific biorecognition defined from the molecular level (*i.e.*, base pairing), suitable for the design of precisely targeted therapeutics. The proposed two-step (consecutive) treatment offers the opportunity of pretargeting.[52–54] This is an advantage over the premixed treatment and other single-component anti-CD20 constructs, such as rituximab polymers[55] and multivalent anti-CD20 Fab'-functionalized polymers.[47–49] For example, the timing of administration of the crosslinking dose (P-MORF2) can be optimized based on biodistribution of the pretargeting dose (Fab'-MORF1), in order to

achieve maximal tumor-to-tissue accumulation in individual patients and enable more efficient treatment. This approach would also limit potential adverse reactions associated with off-target binding, thus being beneficial for the treatment of solid tumors as well as disseminated diseases. For blood-based cancers, the pharmacokinetics of Fab'-MORF1 and the binding kinetics of Fab'-MORF1 to diseased cells can be further studied to determine the best timing for P-MORF2 administration.

The presented work offers a new strategy in lymphoma treatment by immune-independent apoptosis induction. This is a potential improvement over currently used immunotherapies with type I anti-CD20 mAbs (*e.g.*, rituximab).[14,16] Comparing to type II anti-CD20 mAbs (*e.g.*, obinutuzumab) that may also induce direct apoptosis,[56] our nanomedicine approach still possesses two advantages: (1) superior targeting of B-cells due to multivalency, and (2) potential for decreased side effects that are associated with immune functions. Previously our lab has designed and developed a pilot anti-CD20 drug-free macromolecular therapeutic system using a pair of pentaheptad peptides that formed antiparallel coiled-coil heterodimers as the biorecognition moieties.[9,50] The binding of CCE and CCK served as the driving force for CD20 clustering and concomitant apoptosis induction in malignant B-cells. When the cell surface biorecognition and apoptosis were evaluated on Raji cells (using conditions similar to this study), we found that a 25-time excess of the second peptide (CCE:CCK = 1:25) was required in order to achieve significant efficacy *in vitro*[9] and *in vivo*[50]. In contrast, for the hybridization-mediated system (Fab'-MORF1/P-MORF2), the treatment with **equimolar MORF1/MORF2** was sufficient for biorecognition and apoptosis induction (Table 3.1). Results of the animal experiments showed that at equivalent doses, a single treatment of

Fab'-MORF1 + P-MORF2 (1:1) was significantly more effective than a single treatment of Fab'-CCE + P-CCK (1:25) in preventing lymphoma dissemination (Table 3.1). In conjunction these data suggested superior binding and accessibility of the MORF oligos on the HPMA polymer chains as compared to the coiled-coil forming peptides. In addition, for the MORF1-MORF2 hybridization, a rapid binding kinetics was observed (~10 min as characterized by DLS; Figure 3.5B in the main article). On the contrary, the CCE-CCK coiled-coil formation required a much longer time (~60 min).[9] The comparison of CCs vs. MORFs clearly indicates that the hybridization system is advantageous for the design of drug-free macromolecular therapeutics. Other advantages of the MORF oligos include: (1) specific binding due to a well-defined hydrogen bonding pattern (*i.e.*, base pairing), (2) charge-neutral property that prevents potential off-target effects, and (3) water solubility due to good base-stacking property resulting in favorable pharmacokinetics.[26]

Besides lymphomas, the therapeutic conjugates developed here can be used for other B-cell-associated diseases such as rheumatoid arthritis, multiple sclerosis, and chronic lymphocytic leukemia. The designed platform can be applied to crosslink any non- or slowly internalizing receptor (*e.g.*, CD45,[57] prostate stem cell antigen[58]) and control different cellular activities.[21–23] In addition, other targeting moieties (*e.g.*, aptamer instead of Fab')[54] can be used to construct various self-assembling antigen crosslinkers. Therefore, this work constitutes a new paradigm of nanomaterial-based therapeutics with significant potential for the treatment of multiple different diseases.

3.5 References

1. S. M. Douglas, I. Bachelet and G. M. Church, A logic-gated nanorobot for targeted transport of molecular payloads, *Science*, 2012, **335**, 831–834.

2. J. J. Mulvey, *et al.*, Self-assembly of carbon nanotubes and antibodies on tumours for targeted, amplified delivery, *Nat. Nanotechnol.*, 2013, **8**, 763–771.

3. Z. R. Lu, P. Kopečková and J. Kopeček, Polymerizable Fab' antibody fragments for targeting of anticancer drugs, *Nat. Biotechnol.*, 1999, **17**, 1101–1104.

4. M. Gungormus, M. Branco, H. Fong, J. P. Schneider, C. Tamerler and M. Sarikaya, Self assembled bi-functional peptide hydrogels with biomineralization-directing peptides, *Biomaterials*, 2010, **31**, 7266–7274.

5. T. C. Holmes, S. de Lacalle, X. Su, G. Liu, A. Rich and S. Zhang, Extensive neurite outgrowth and active synapse formation on self-assembling peptide scaffolds, *Proc. Natl. Acad. Sci. U.S.A.*, 2000, **97**, 6728–6733.

6. W. Yuan, J. Yang, P. Kopečková and J. Kopeček, Smart hydrogels containing adenylate kinase: translating substrate recognition into macroscopic motion, *J. Am. Chem. Soc.*, 2008, **130**, 15760–15761.

7. J. D. Ehrick, S. K. Deo, T. W. Browning, L. G. Bachas, M. J. Madou and S. Daunert, Genetically engineered protein in hydrogels tailors stimuli-responsive characteristics, *Nat. Mater.*, 2005, **4**, 298–302.

8. J. Liu, D. Mazumdar and Y. Lu, A simple and sensitive ”dipstick” test in serum based on lateral flow separation of aptamer-linked nanostructures, *Angew. Chem. Int. Ed.*, 2006, **45**, 7955–7959.

9. K. Wu, J. Liu, R. N. Johnson, J. Yang and J. Kopeček, Drug-free macromolecular therapeutics: induction of apoptosis by coiled-coil-mediated cross-linking of antigens on the cell surface, *Angew. Chem. Int. Ed.*, 2010, **49**, 1451–1455.

10. M. H. Cho, *et al.*, A magnetic switch for the control of cell death signalling in *in vitro* and *in vivo* systems, *Nat. Mater.*, 2012, **11**, 1038–1043.

11. J. Kopeček and J. Yang, Smart self-assembled hybrid hydrogel biomaterials, *Angew. Chem. Int. Ed.*, 2012, **51**, 7396–7417.

12. R. Siegel, D. Naidsham and A. Jemal, Cancer statistics, 2013, *CA Cancer J. Clin.*, 2013, **63**, 11–30.

13. B. D. Cheson and J. P. Leonard, Monoclonal antibody therapy for B-cell non-Hodgkin’s lymphoma, *N. Engl. J. Med.*, 2008, **359**, 613–626.

14. A. Molina, A decade of rituximab: improving survival outcomes in non-Hodgkin's lymphoma, *Annu. Rev. Med.*, 2008, **59**, 237–250.

15. G. Cartron, *et al.*, Therapeutic activity of humanized anti-CD20 monoclonal antibody and polymorphism in IgG Fc receptor FcγRIIIa gene, *Blood*, 2002, **99**, 754–758.

16. M. R. Smith, Rituximab (monoclonal anti-CD20 antibody): mechanisms of action and resistance, *Oncogene*, 2003, **22**, 7359–7368.

17. M. Allison, PML problems loom for Rituxan, *Nat. Biotechnol.*, **28**, 105–106.

18. L. C. Lands, New therapies, new concerns: rituximab-associated lung injury, *Pediatr. Nephrol.*, 2010, **25**, 1001–1003.

19. K. Kamei, S. Ito and K. Iijima, Severe respiratory adverse events associated with rituximab infusion, *Pediatr. Nephrol.*, 2010, **25**, 1193.

20. L. E. van der Kolk, A. J. Grillo-López, J. W. Baars, C. E. Hack and M. H. van Oers, Complement activation plays a key role in the side-effects of rituximab treatment, *Br. J. Haematol.*, 2001, **115**, 807–811.

21. Y. Shimizu, *et al.*, Crosslinking of the T cell-specific accessory molecules CD7 and CD28 modulates T cell adhesion, *J. Exp. Med.*, 1992, **175**, 577–582.

22. L. D. Vallat, Y. Park, C. Li and J. G. Gribben, Temporal genetic program following B-cell receptor cross-linking: altered balance between proliferation and death in healthy and malignant B cells, *Blood*, 2007, **109**, 3989–3997.

23. C. R. Kahn, K. L. Baird, D. B. Jarrett and J. S. Flier, Direct demonstration that receptor crosslinking or aggregation is important in insulin action, *Proc. Natl. Acad. Sci. U. S. A.*, 1978, **75**, 4209–4213.

24. J. P. Deans, H. Li and M. J. Polyak, CD20-mediated apoptosis: signalling through lipid rafts, *Immunology*, 2002, **107**, 176–182.

25. P. E. Nielsen, DNA analogues with nonphosphodiester backbones, *Annu. Rev. Biophys. Biomol. Struct.*, 1995, **24**, 167–183.

26. J. Summerton and D. Weller, Morpholino antisense oligomers: design, preparation, and properties, *Antisense Nucleic Acid Drug Dev*., 1997, **7**, 187–195.

27. G. Liu, *et al.*, Pretargeting in tumored mice with radiolabeled morpholino oligomer showing low kidney uptake, *Eur. J. Nucl. Med. Mol. Imaging*, 2004, **31**, 417–424.

28. K. O. Mang'era, *et al.*, Initial investigations of ^{99m}Tc-labeled morpholinos for radiopharmaceutical applications, *Eur. J. Nucl. Med. Mol. Imaging*, 2001, **28**, 1682–1689.

29. J. Kopeček and P. Kopečková, HPMA copolymers: origins, early developments, present, and future, *Adv. Drug Deliv. Rev.*, 2010, **62**, 122–149.

30. K. Ulbrich and V. Šubr, Structural and chemical aspects of HPMA copolymers as drug carriers, *Adv. Drug Deliv. Rev.*, 2010, **62**, 150–166.

31. K. D. Fowers, J. Callahan, P. Byron and J. Kopeček, Preparation of Fab' from murine IgG2a for thiol reactive conjugation, *J. Drug Target.*, 2001, **9**, 281–294.

32. H. Pan, J. Yang, P. Kopečková and J. Kopeček, Backbone degradable multiblock *N*-(2-hydroxypropyl)methacrylamide copolymer conjugates *via* reversible addition-fragmentation chain transfer polymerization and thiol-ene coupling reaction, *Biomacromolecules*, 2011, **12**, 247–252.

33. J. Kopeček and H. Bažilová, Poly[*N*-(2-hydroxypropyl)methacrylamide] — I. Radical polymerization and copolymerization, *Eur. Polym. J.*, 1973, **9**, 7–14.

34. V. Šubr and K. Ulbrich, Synthesis and properties of new *N*-(2-hydroxypropyl)methacrylamide copolymers containing thiazolidine-2-thione reactive groups, *React. Funct. Polym.*, 2006, **66**, 1525–1538.

35. V. Omelyanenko, P. Kopečková, C. Gentry and J. Kopeček, Targetable HPMA copolymer – adriamycin conjugates. Recognition, internalization, and subcellular fate, *J. Control. Release*, 1998, **53**, 25–37.

36. M. A. Ghetie, J. Richardson, T. Tucker, D. Jones, J. W. Uhr and E. S. Vitetta, Disseminated or localized growth of a human B-cell tumor (Daudi) in SCID mice, *Int. J. Cancer*, 1990, **45**, 481–485.

37. M. A. Ghetie, K. Tucker, J. Richardson, J. W. Uhr and E. S. Vitetta, The antitumor activity of an anti-CD22 immunotoxin in SCID mice with disseminated Daudi lymphoma is enhanced by either an anti-CD19 antibody or an anti-CD19 immunotoxin, *Blood*, 1992, **80**, 2315–2320.

38. G. L. Griffiths, *et al.*, Cure of SCID mice bearing human B-lymphoma xenografts by an anti-CD74 antibody – anthracycline drug conjugate, *Clin. Cancer Res.*, 2003, **9**, 6567–6571.

39. W. C. Chen, G. C. Completo, D. S. Sigal, P. R. Crocker, A. Saven and J. C. Paulson, *In vivo* targeting of B-cell lymphoma with glycan ligands of CD22, *Blood*, 2010, **115**, 4778–4786.

40. P. Stashenko, L. M. Nadler, R. Hardy and S. F. Schlossman, Characterization of a human B lymphocyte-specific antigen, *J. Immunol.*, 1980, **125**, 1678–1685.

41. K. C. Anderson, *et al.*, Expression of human B cell-associated antigens on leukemias and lymphomas: a model of human B cell differentiation, *Blood*, 1984, **63**, 1424–1433.

42. E. Kimby, Tolerability and safety of rituximab (MabThera®), *Cancer Treat. Rev.*, 2005, **31**, 456–473.

43. O. W. Press, *et al.*, Monoclonal antibody 1F5 (anti-CD20) serotherapy of human B cell lymphomas, *Blood*, 1987, **69**, 584–591.

44. W. C. Johnson, CD of nucleic acids, In: *Circular Dichroism: Principles and Applications*, Eds.: N. Berova, K. Nakanishi and R. W. Woody, Wiley-VCH, 2000, pp 703–718.

45. D. Shan, J. A. Ledbetter and O. W. Press, Apoptosis of malignant human B cells by ligation of CD20 with monoclonal antibodies, *Blood*, 1998, **91**, 1644–1652.

46. H. Ben-Bassat, *et al.*, Establishment in continuous culture of a new type of lymphocyte from a "Burkitt like" malignant lymphoma (line D.G.-75), *Int. J. Cancer*, 1977, **19**, 27–33.

47. R. N. Johnson, P. Kopečková and J. Kopeček, Synthesis and evaluation of multivalent branched HPMA copolymer–Fab' conjugates targeted to the B-cell antigen CD20, *Bioconjug. Chem*., 2009, **20**, 129–137.

48. R. N. Johnson, P. Kopečková and J. Kopeček, Biological activity of anti-CD20 multivalent HPMA copolymer–Fab' conjugates. *Biomacromolecules*, 2012, **13**, 727–735.

49. T.-W. Chu, J. Yang and J. Kopeček, Anti-CD20 multivalent HPMA copolymer–Fab' conjugates for the direct induction of apoptosis, *Biomaterials*, 2012, **33**, 7174–7181.

50. K. Wu, J. Yang, J. Liu and J. Kopeček, Coiled-coil based drug-free macromolecular therapeutics: *in vivo* efficacy, *J. Control. Release*., 2012, **157**, 126–131.

51. M. Okroj, A. Österborg and A. M. Blom, Effector mechanisms of anti-CD20 monoclonal antibodies in B cell malignancies, *Cancer Treat. Rev.*, 2013, **39**, 632–639.

52. D. A. Goodwin and C. F. Meares, Advances in pretargeting biotechnology, *Biotechnol. Adv.*, 2001, **19**, 435–450.

53. J. Gunn, S. I. Park, O. Veiseh, O. W. Press and M. A. Zhang, Pretargeted nanoparticle system for tumor cell labeling, *Mol. Biosyst.*, 2011, **7**, 742–748.

54. J. Zhou, B. Soontornworajit, M. P. Snipes and Y. Wang, Development of a novel pretargeting system with bifunctional nucleic acid molecules, *Biochem. Biophys. Res. Commun.*, 2009, **386**, 521–525.

55. N. Zhang, L. A. Khawli, P. Hu and A. L. Epstein, Generation of rituximab polymer may cause hyper-cross-linking–induced apoptosis in non-Hodgkin's lymphomas, *Clin. Cancer Res*., 2005, **11**, 5971–5980.

56. S. Herter, *et al.*, Preclinical activity of the type II CD20 antibody GA101 (obinutuzumab) compared with rituximab and ofatumumab *in vitro* and in xenograft models, *Mol. Cancer Ther.*, 2013, **12**, 2031–2042.

57. J. T. Nguyen, *et al.*, CD45 modulates galectin-1-induced T cell death: regulation by expression of core 2 *O*-glycans, *J. Immunol.*, 2001, **167**, 5697–5707.

58. Z. Gu, J. Yamashiro, E. Kono and R. E. Reiter, Anti-prostate stem cell antigen monoclonal antibody 1G8 induces cell death *in vitro* and inhibits tumor growth *in vivo via* a Fc-independent mechanism, *Cancer Res.*, 2005, **65**, 9495–9500.

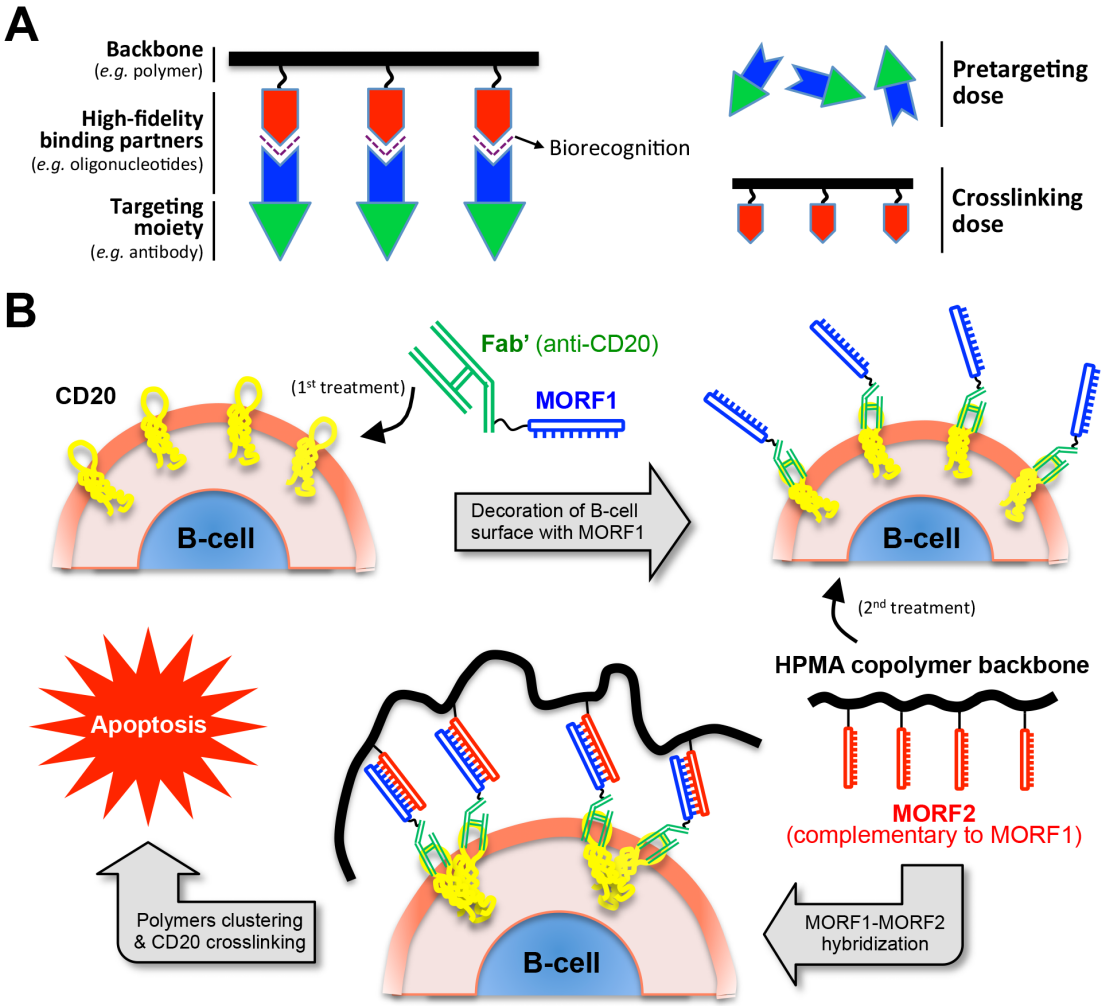

Figure 3.1 Self-assembling hybrid nanoconjugates for apoptosis induction. (A) General design concept of the therapeutic platform. Two nanoconjugates that self-assemble *via* biorecognition can be administered consecutively as pretargeting and crosslinking doses, or premixed to form a multivalent construct and used as a single dose. (B) Apoptosis induction of B-cells by crosslinking of the CD20 antigens that is mediated by extracellular hybridization of complementary morpholino oligonucleotides (MORF1-MORF2).

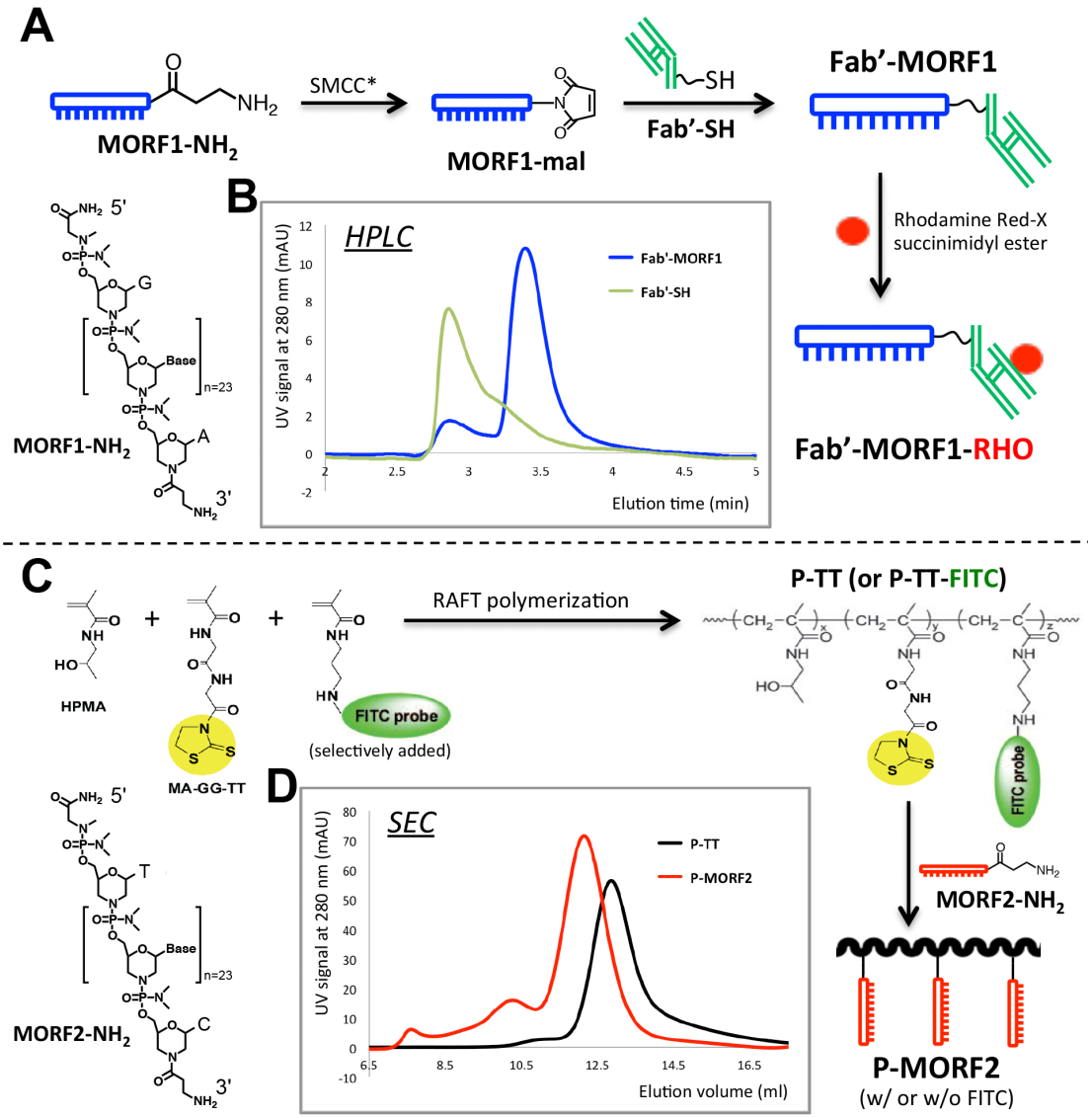

Figure 3.2 Synthesis of Fab'-MORF1 and P-MORF2. (A) Scheme of Fab'-MORF1 synthesis. *SMCC: succinimidyl-4-(*N*-maleimidomethyl)cyclohexane-1-carboxylate heterobifunctional linker. (B) HPLC analysis of the Fab' fragment (Fab'-SH) of 1F5 mAb and the Fab'-MORF1 conjugate; Agilent Zorbax 300SB-C18 column (4.6 x 250 mm) eluted with a gradient of buffer A (H_2O + 0.1% trifluoroacetic acid v/v) and buffer B (acetonitrile + 0.1% trifluoroacetic acid v/v). (C) Scheme of the synthesis of polymer precursors (P-TT) and multivalent conjugates (P-MORF2). MA-GG-TT: *N*-methacryloylglycylglycine thiazolidine-2-thione (MA-GG-TT). (D) SEC analysis of representative P-TT and P-MORF2 (valence = 3); Superose 6 HR10/30 column (acetate buffer + 30% acetonitrile v/v).

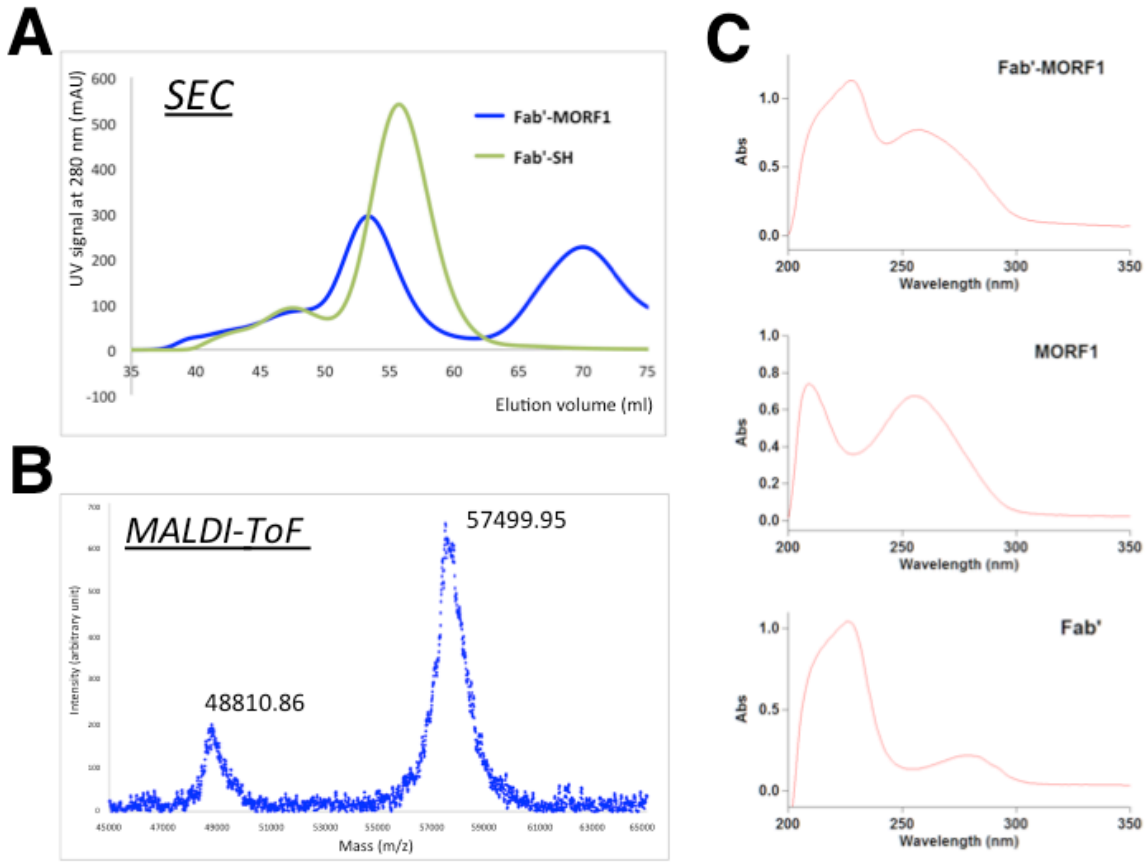

Figure 3.3 Characterization of Fab'-MORF1. (A) Size exclusion chromatography (SEC) analysis of the Fab' fragment (Fab'-SH) of 1F5 mAb and the Fab'-MORF1 conjugate using Sephacryl S-100 HR16/60 column eluted with PBS. The profile of Fab'-MORF1 demonstrates the process of purification by ÄKTA FPLC – the first peak (eluted at 53 mL) represents the conjugate (collected during purification); the second peak (eluted at 70 mL) indicates unconjugated MORF1 (removed). Fab'-MORF1 was characterized by an earlier elution volume compared to Fab'-SH (56 mL). (B) MALDI-ToF mass spectrum of Fab'-MORF1. The major fraction shows that the molecular weight is about 57.5 kDa (Fab': ~48.8 kDa, MORF1: ~8.6 kDa); a small fraction of unconjugated Fab' was observed. (C) UV-Vis spectra of the purified Fab'-MORF1, unconjugated MORF1, and Fab' fragment. Concentrations of all components were 2.5 μM. The Fab'-MORF1 conjugate was characterized by a combination of absorbance at 260 nm (contributed by MORF1) and 280 nm (contributed by Fab').

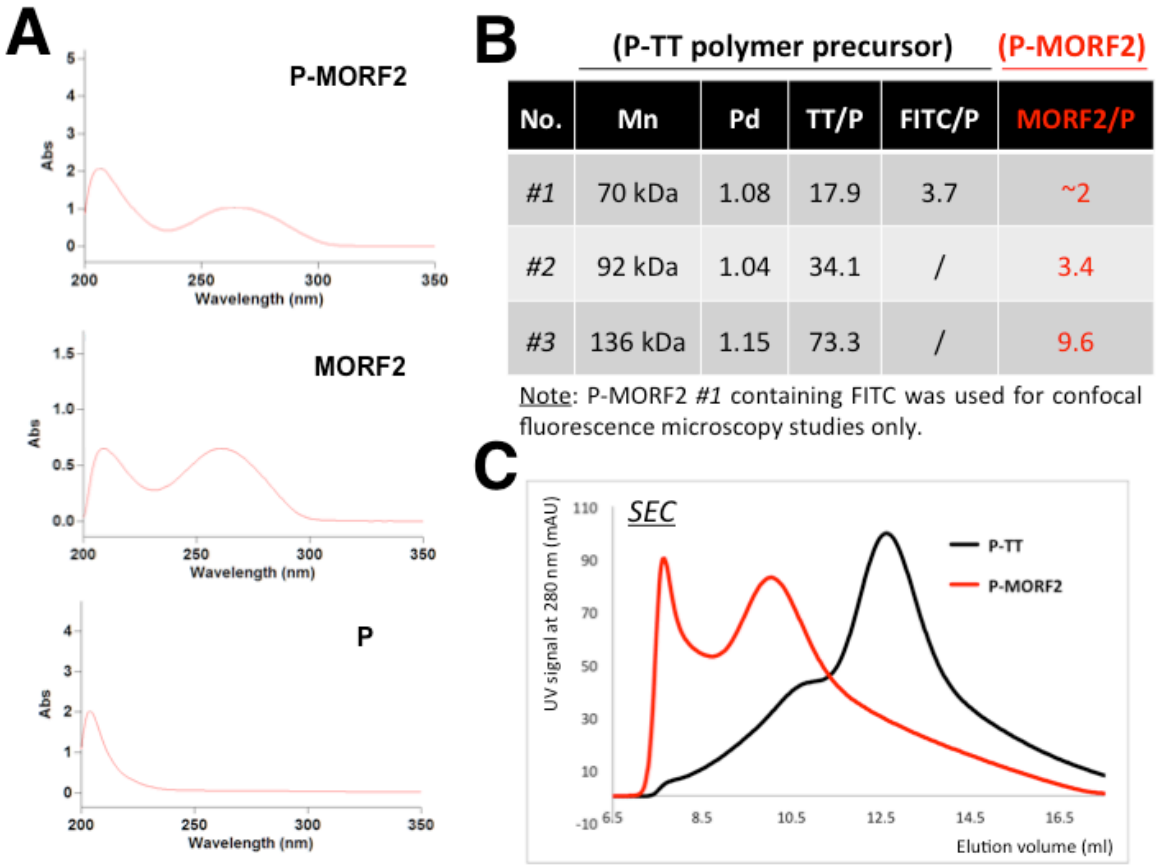

Figure 3.4 Characterization of P-MORF2. (A) UV-Vis spectra of the SEC-purified P-MORF2 conjugate (1 mg/mL), unconjugated MORF2 (2.5 μM), and HPMA polymers (P) (1 mg/mL). The multivalent P-MORF2 conjugates were characterized by UV absorbance at 260 nm (contributed by MORF2). (B) Physicochemical properties of different P-MORF2 conjugates and their polymer precursors (P-TT) that were synthesized and used in this study. Number average molecular weight (Mn) and polydispersity (Pd) were determined by SEC. Number of thiazolidine-2-thione (TT) groups per polymer chain (TT/P) was determined by UV absorbance at 305 nm; number of FITC per chain (FITC/P) was determined by absorbance at 495 nm; number of MORF2 oligo per chain (MORF2/P) was determined by UV absorbance at 260 nm. (C) Size exclusion chromatography (SEC) analysis of P-MORF2 #3 and its P-TT polymer precursor by ÄKTA FPLC; Superose 6 HR10/30 column (acetate buffer pH 6.5 + 30% acetonitrile v/v). The retention limit of this column is about 7 mL.

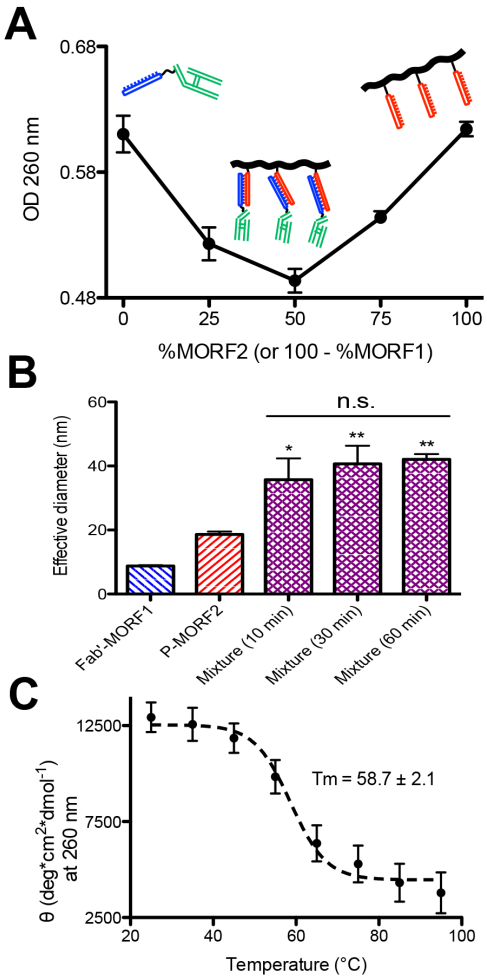

Figure 3.5 *In vitro* hybridization of Fab'-MORF1 and P-MORF2. (A) Hypochromic effect upon hybridization of Fab'-MORF1 and P-MORF2 as analyzed by UV-Vis. The optical density (OD) at 260 nm decreased when the two conjugates were mixed (in different ratios). (B) Effective hydrodynamic diameters of the two conjugates and their mixture (equimolar MORF1/MORF2; tested at different times after mixing) as characterized by dynamic light scattering. The valence of P-MORF2 was 3. Statistics, unless otherwise indicated, was performed by comparing the mixture with P-MORF2 (* $p < 0.05$; ** $p < 0.005$; n.s., no significant difference). (C) CD thermal melting curve of the hybridized Fab'-MORF1/P-MORF2. The molar ellipticity (θ) at 260 nm underwent a sigmoidal decrease as temperature increased. The melting temperature (Tm) resulted from fitting the data to a logistic function using nonlinear regression (GraphPad Prism 5 software). All experiments were performed at physiological conditions (PBS, pH 7.4). Data are presented as mean ± SD ($n = 3$, Student's *t*-test).

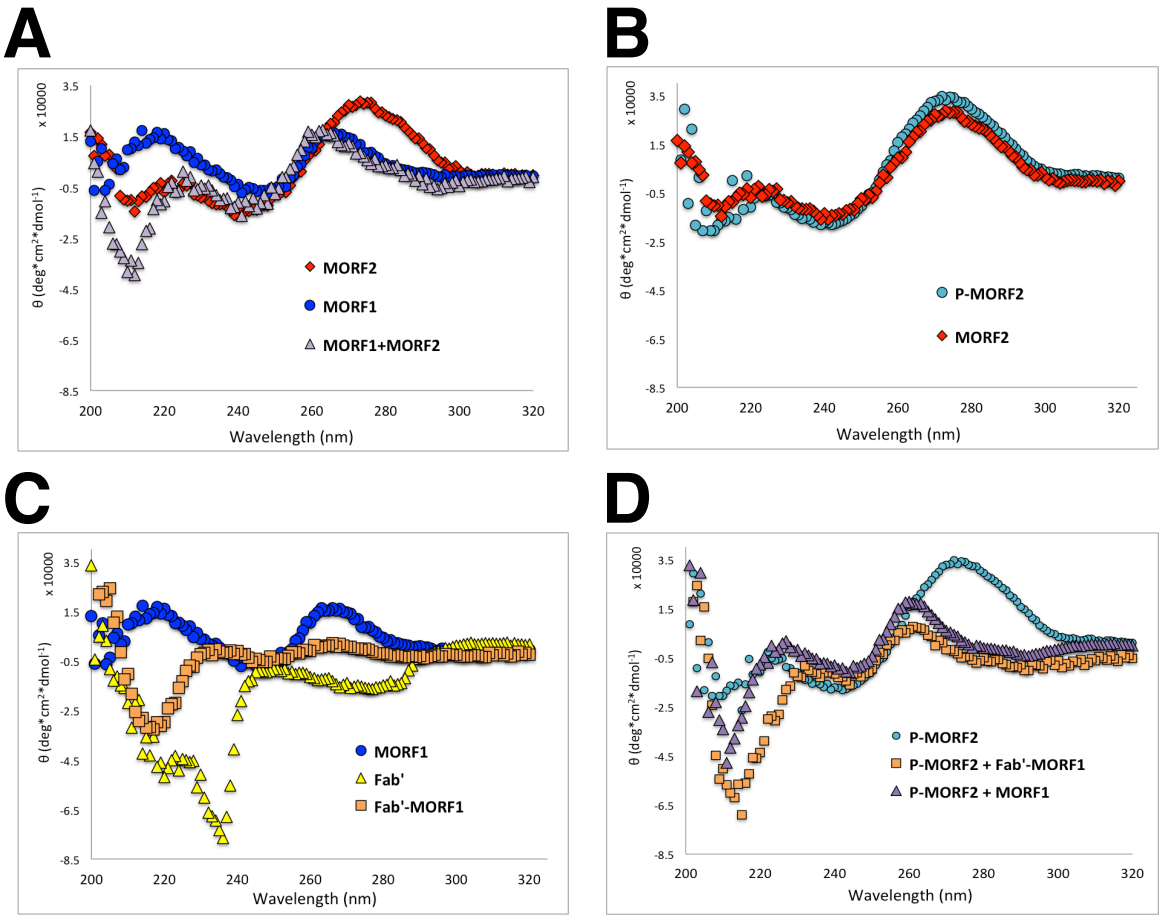

Figure 3.6 CD spectra of free, unconjugated MORFs, the conjugates, and their mixtures. All components were dissolved in PBS (pH 7.4) at 50 μM MORF equivalent concentration. The y-axis shows molar ellipticity (θ). (A) Free MORF1, MORF2, and the equimolar mixture of both. When mixed, an optical signature (maxima at 260 nm, minima at 210 nm) indicates that A-form double helixes were formed. (B) Comparison of P-MORF2 (valence = 3) with free MORF2. An identical spectrum was observed. (C) Comparison of the Fab'-MORF1 conjugate with free Fab' fragment and free MORF1. The conjugate appears to have the combined optical signatures of Fab' and MORF1. (D) Mixing P-MORF2 with either free MORF1 or Fab'-MORF1 (equimolar MORF1/MORF2 concentrations) shifted the CD spectrum from that of the single-stranded MORF2 to that indicating A-form double-stranded oligos. Such spectral shift suggested that the function of MORF1-MORF2 hybridization was preserved after conjugation to Fab' or polymers.

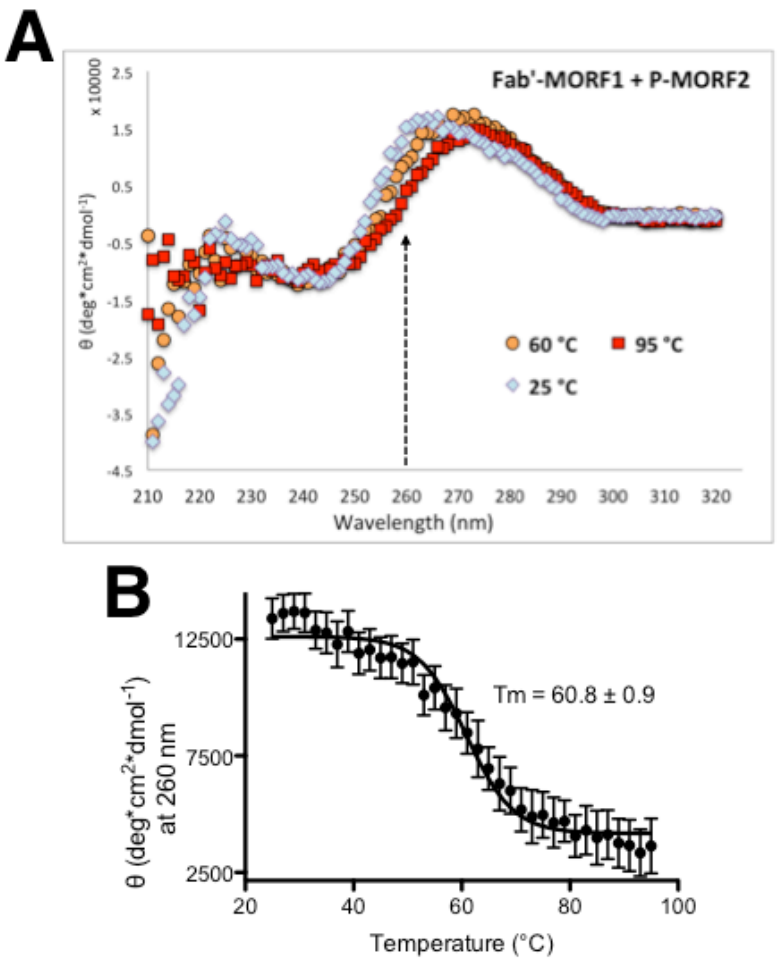

Figure 3.7 Analysis of melting temperature (Tm) of the Fab'-MORF1/P-MORF2 hybridization by CD spectroscopy. (A) CD spectra of the mixture of Fab'-MORF1 (5 μM MORF1-eqv.) and P-MORF2/v3 (5 μM MORF2-eqv.; valence = 3) in PBS (pH 7.4) at different temperatures. When temperature increased from 25 °C to 60 and 95 °C, the positive band at 260 nm underwent a bathochromic shift that produced a peak centered around 275 nm. Molar ellipticity (θ) at 260 nm was used in the following thermal melting studies. (B) CD thermal melting curve of the hybridized Fab'-MORF1/P-MORF2. A sigmoidal decrease of θ at 260 nm was observed as temperature increased. Data are presented as mean ± SD (n = 3). These data were fitted to a logistic function to obtain Tm; results of nonlinear regression indicated Tm = 60–62 °C. The forward scan (increasing temperature) analysis as shown here gave similar results as the reverse scan (decreasing temperature; see Figure 3.5C).

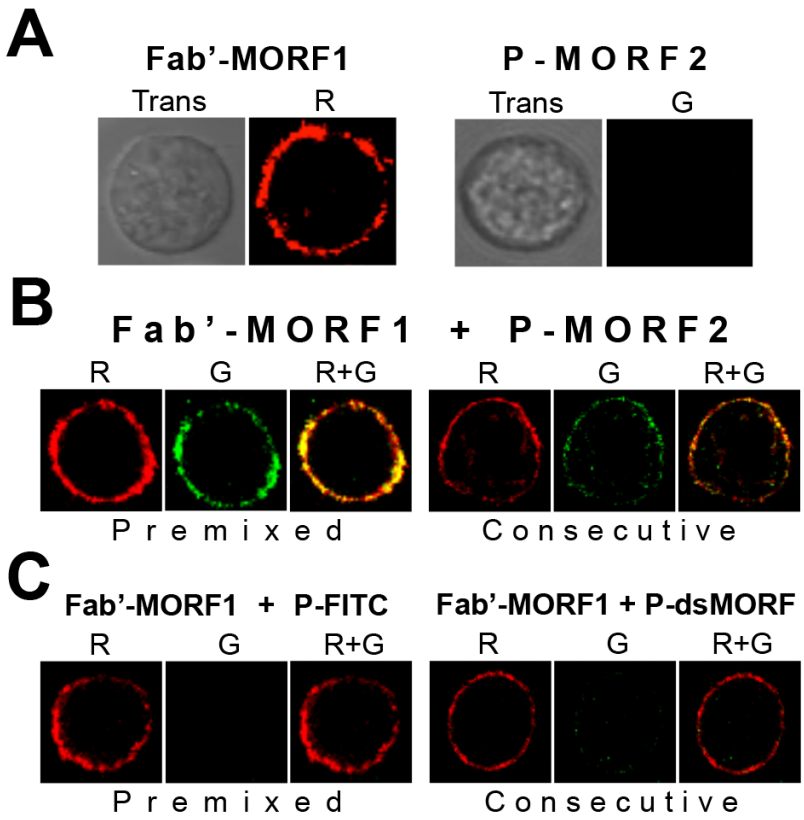

Figure 3.8 Biorecognition of Fab'-MORF1 and P-MORF2 at the B-cell surface. Confocal microscopic images of Raji B-cells ($CD20^{+}$) exposed to Fab'-MORF1 (labeled with rhodamine; red) and P-MORF2 (labeled with FITC; green; valence = 2) are shown. Trans: images acquired under transmitted light, R: red channel, G: green channel. (A) Cells exposed to only Fab'-MORF1 (0.4 μM) or P-MORF2 (0.4 μM, MORF2 equivalent). (B) Cells exposed to the mixture of Fab'-MORF1 (0.4 μM) and P-MORF2 (0.4 μM, MORF2 equivalent) (*Premixed*), or Fab'-MORF1 first, followed 1 h later by P-MORF2 (*Consecutive*). (C) Control studies: (left panel) cells exposed to a premixture of Fab'-MORF1 (0.5 μM) and polymer precursors labeled with FITC (P-FITC; excess amount); (right panel) cells exposed consecutively to Fab'-MORF1 (0.5 μM) and P-MORF2 preblocked by MORF1 (P-dsMORF; excess amount).

Figure 3.9 Apoptosis induction of Raji B-cells. Percentage of apoptotic cells were analyzed by annexin V/PI binding and quantified by flow cytometry. Incubation time was 48 h. (A) *Untreated*: cells in culture medium; *mAb + 2° Ab*: 1F5 mAb (1 μM) followed (1 h later) by goat anti-mouse secondary Ab (0.5 μM); *Fab'-MORF1*: single-component at 1 μM; *P-MORF2*: single-component of P-MORF2/v3 at 1 μM (MORF2-eqv.); *Consecutive*: Fab'-MORF1 (1 μM) followed (1 h later) by P-MORF2/v3 (1 μM); *Premixed*: premixture of Fab'-MORF1 (1 μM) and P-MORF2/v3 (1 μM). Statistics, unless otherwise indicated, were performed by comparing each group with untreated (*** $p < 0.0001$; n.s., no significant difference). (B) Treatments with different concentrations of Fab'-MORF1 (as indicated) and corresponding P-MORF2/v3 (at equimolar MORF1/MORF2). ** $p < 0.005$; n.s., no significant difference. (C) Treatments with different valences of P-MORF2 (3 or 10 MORF2 per polymer chain) and different MORF1:MORF2 molar ratios (1:1 or 1:10). *Cons*: consecutive treatment of two conjugates; *Prem*: premixture of two conjugates. Concentration of Fab'-MORF1 was 0.5 μM. *P-MORF2*: single-component treatment with P-MORF2/v3 or P-MORF2/v10 at 5 μM (MORF2 equivalent); *mAb + 2° Ab*: 1F5 mAb (0.5 μM) followed by goat anti-mouse secondary Ab (0.25 μM). Statistics, unless otherwise indicated, were performed by comparing each "high-valence" group with the corresponding "low-valence" group (** $p < 0.005$; n.s., no significant difference). All data are presented as mean ± SD ($n = 3$, Student's *t*-test).

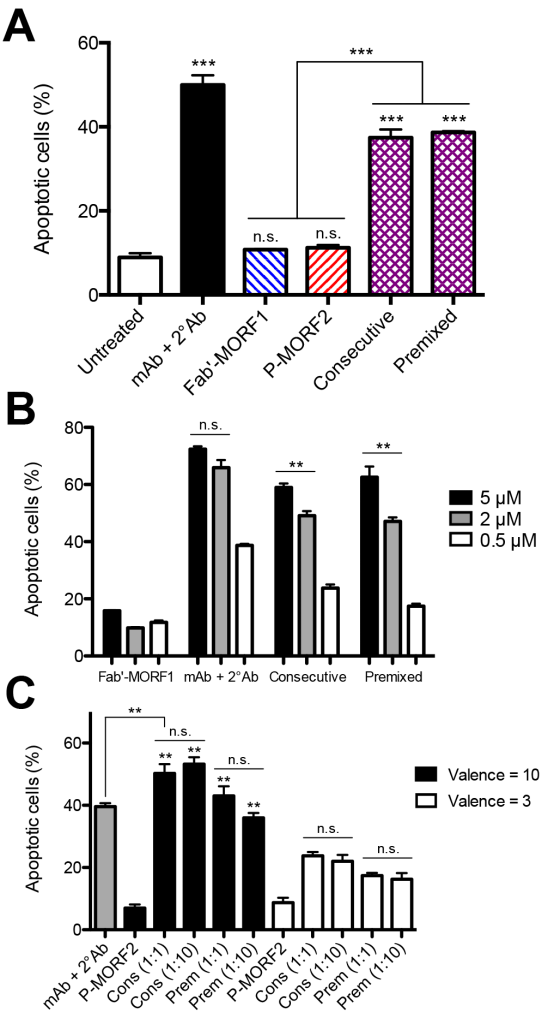
A
Apoptotic cells (%)
60
40
20
0
***
***
***
***
n.s.
n.s.
Untreated
mAb + 2°Ab
Fab'-MORF1
P-MORF2
Consecutive
Premixed
B
Apoptotic cells (%)
80
60
40
20
0
n.s.
**
**
5 μM
2 μM
0.5 μM
Fab'-MORF1
mAb + 2°Ab
Consecutive
Premixed
C
Apoptotic cells (%)
60
40
20
0
**
n.s.
**
**
n.s.
**
**
n.s.
n.s.
Valence = 10
Valence = 3
mAb + 2°Ab
P-MORF2
Cons (1:1)
Cons (1:10)
Prem (1:1)
Prem (1:10)
P-MORF2
Cons (1:1)
Cons (1:10)
Prem (1:1)
Prem (1:10)

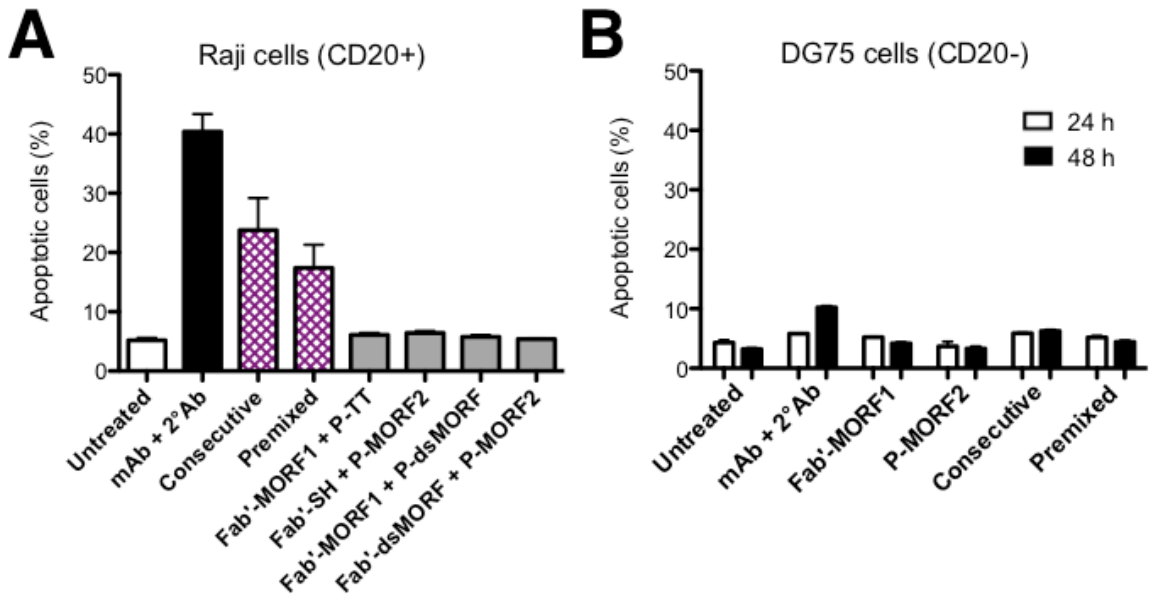

Figure 3.10 Control studies of *in vitro* apoptosis by annexin V/PI binding assay. (A) Apoptosis induction of Raji B-cells (high levels of CD20 expression). Incubation time was 48 h. (B) Apoptosis induction of DG75 B-cells (minimal or no CD20 expression). Incubation time was as indicated. The following indications apply to both figures – *Untreated*: cells in culture medium; *mAb + 2° Ab*: 1F5 mAb (0.5 μM) followed (1 h later) by goat anti-mouse secondary Ab (0.25 μM); *Fab'-MORF1*: single-component at 0.5 μM; *P-MORF2*: single-component of P-MORF2/v3 at 0.5 μM (MORF2 equivalent); *Consecutive*: Fab'-MORF1 (0.5 μM) followed (1 h later) by P-MORF2/v3 (0.5 μM MORF2-eqv.); *Premixed*: premixture of Fab'-MORF1 (0.5 μM) and P-MORF2/v3 (0.5 μM MORF2-eqv.); *Fab'-MORF1 + P-TT*: premixture of Fab'-MORF1 (0.5 μM) and the polymer precursor P-TT #2 (1 mg/mL); *Fab'-SH + P-MORF2*: premixture of free Fab' (0.5 μM) and P-MORF2 (0.5 μM MORF2-eqv.); *Fab'-MORF1 + P-dsMORF*: consecutive treatment (1-h interval) of Fab'-MORF1 (0.5 μM) and "preblocked" P-MORF2 (~1 mg/mL) whose MORF2 binding sites were blocked by excess free MORF1 (1 h before treatment); *Fab'-dsMORF + P-MORF2*: consecutive treatment (1-h interval) of "preblocked" Fab'-MORF1 (0.5 μM) whose MORF1 binding sites were blocked by excess free MORF2 (1 h before treatment) and P-MORF2 (0.5 μM MORF2-eqv.). Apoptotic cells percentage was quantified by flow cytometry. Data are presented as mean ± SD (n = 3).

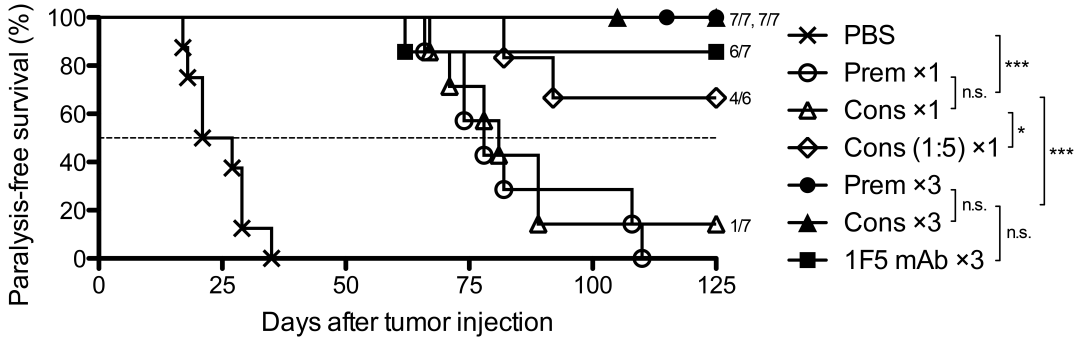

Figure 3.11 Therapeutic efficacy of the nanomedicine against systemic lymphoma in mice. Four million Raji B-cells were injected *via* tail vein on day 0; incidence of hind-limb paralysis or survival of mice was monitored until day 125. One-dose treatment on day 1; three-dose treatment on days 1, 3, and 5. *PBS*: mice injected with PBS (n = 8); *Cons ×1*: consecutive treatment of Fab'-MORF1 and P-MORF2/v10, one-dose (n = 7); *Prem ×1*: premixture of Fab'-MORF1 and P-MORF2/v10, one-dose (n = 7); *Cons (1:5) ×1*: consecutive treatment, MORF1:MORF2 = 1:5, one-dose (n = 6); *Cons ×3*: three doses of consecutive treatment (n = 7); *Prem ×3*: three doses of premixture (n = 7); *1F5 mAb ×3*: three doses of 1F5 mAb (n = 7). The paralysis-free survival of mice is presented in a Kaplan-Meier plot. Numbers of long-term survivors in each group are indicated (if any). Statistics were performed with log-rank test (* $p < 0.05$; *** $p < 0.0001$; n.s., no significant difference).

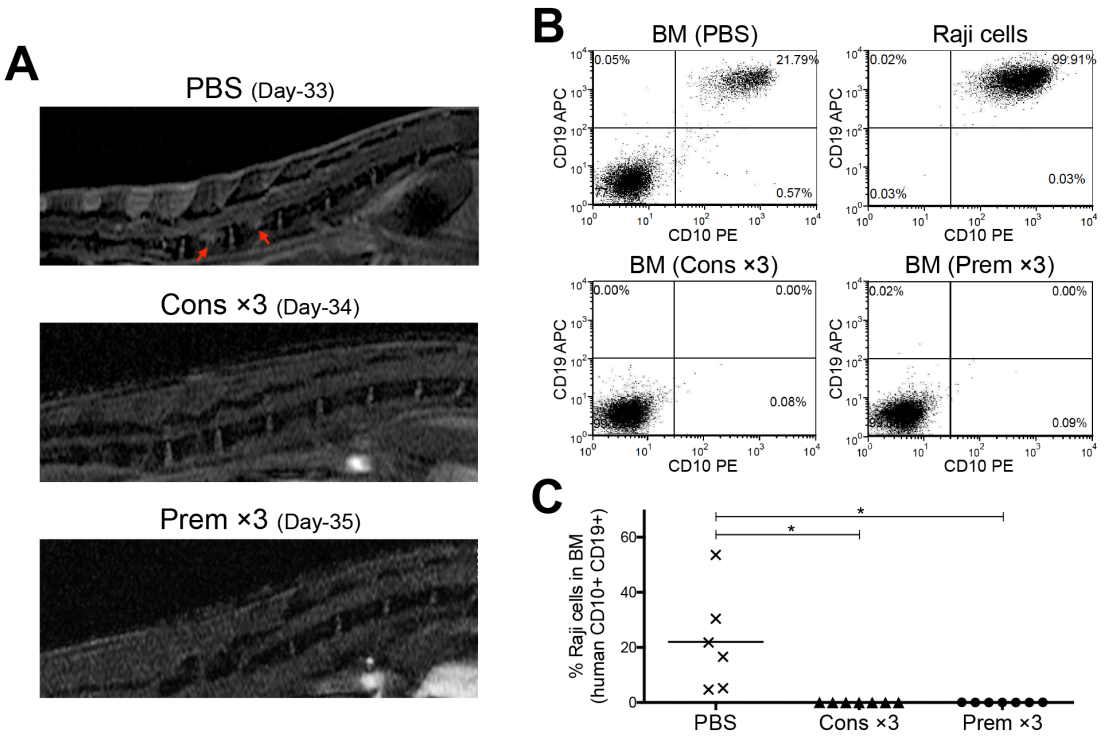

Figure 3.12 Eradication of Raji cells in mice. Mice i.v. injected with 4×10^6 Raji B-cells on day 0 were exposed to different treatments – *PBS*: mice injected with PBS; *Cons ×3*: consecutive treatment of Fab'-MORF1 and P-MORF2/v10 on days 1, 3 and 5; *Prem ×3*: three doses of the premixture of Fab'-MORF1 and P-MORF2/v10 on days 1, 3 and 5. (A) Postcontrast T_1-weighted sagittal MRI focusing on the lumbar spine of mice. A heterogeneous appearance and irregularly shaped masses indicating tumor nodules (red arrows) were observed in the spinal cord of control mice (PBS, n = 4), but not in the treated mice (Cons ×3 and Prem ×3, n = 4). (B) Flow cytometry analysis of residual Raji cells in the bone marrow (BM) of the PBS-treated, paralyzed mice (PBS) and the nanomedicine-treated, surviving mice (Cons ×3, Prem ×3). Bone marrow cells isolated from the femur of mice and Raji cells from culture flasks (upper right panel) were stained with PE-labeled mouse anti-human CD10 and APC-labeled mouse anti-human CD19 antibodies. (C) Quantitative comparison of % Raji cells (human $CD10^+$ $CD19^+$) in the bone marrow of control mice (PBS, n = 6) and the nanomedicine-treated mice (Cons ×3 and Prem ×3, n = 7 per group) as analyzed by flow cytometry. Each data point represents an individual mouse; mean % is indicated. Statistics were performed by Student's t-test of unpaired samples (* $p < 0.05$).

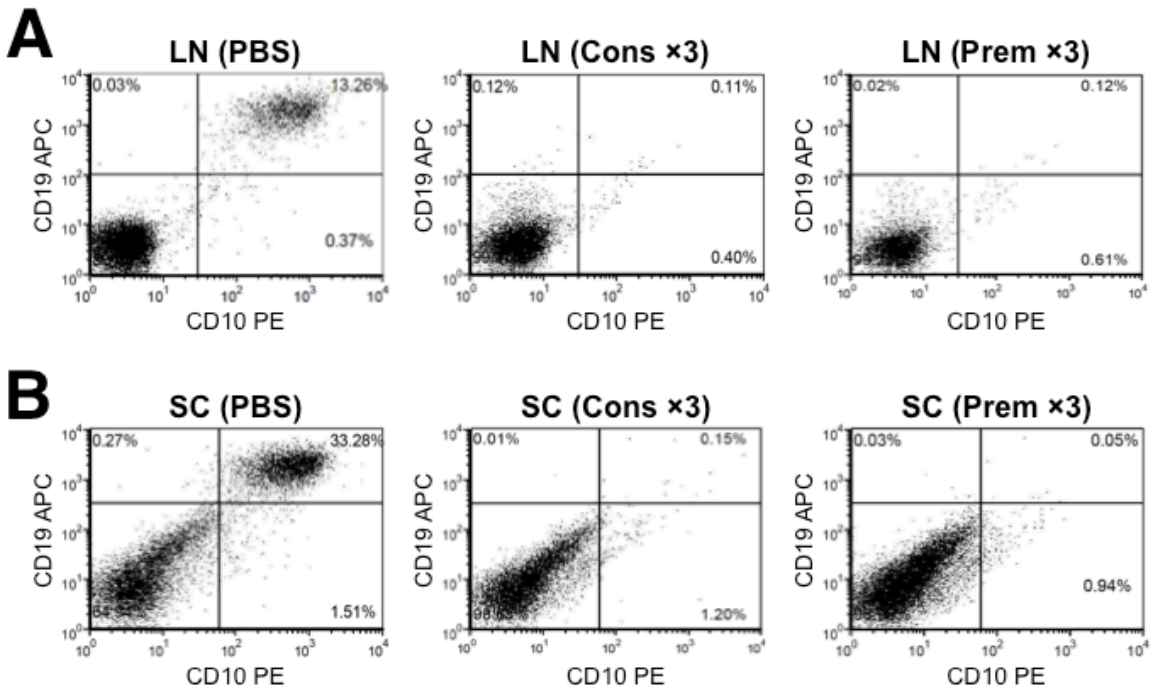

Figure 3.13 Flow cytometry analysis of residual Raji B-cells in different organs/tissues. (A) Cells isolated from the inguinal and mesenteric lymph nodes (LN) of mice. (B) Cells isolated from the spinal cord (SC) of mice. These cells were stained with PE mouse anti-human CD10 and APC mouse anti-human CD19 antibodies; upper right quadrant ($CD10^+$ $CD19^+$) represents Raji cells. Results indicated that the PBS-treated, paralyzed mice (PBS) bore Raji cells in both LN (n = 6) and SC (n = 3), while the long-term survivors in the therapy groups (Cons ×3, Prem ×3) were tumor free (n = 6 per group).

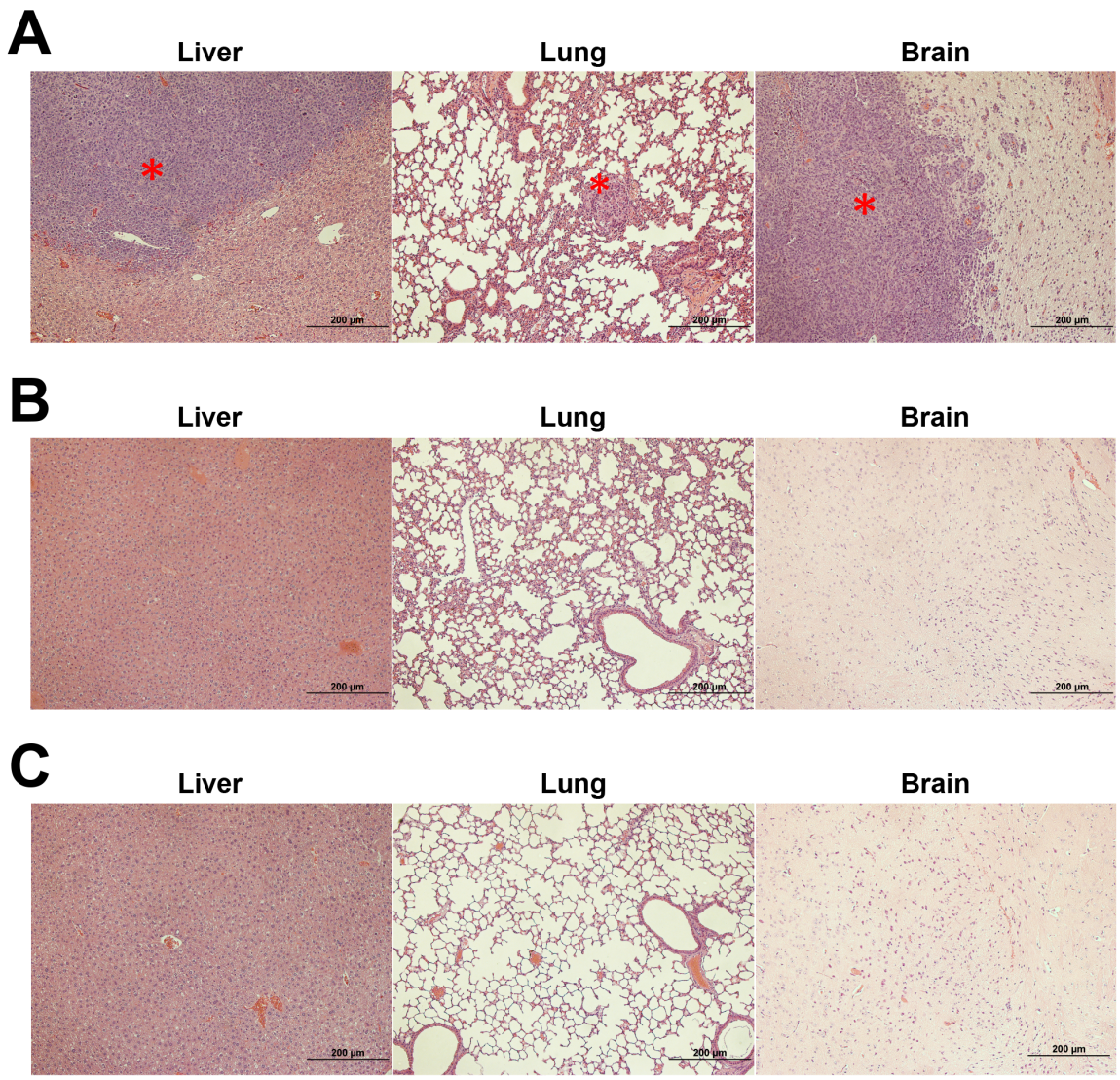

Figure 3.14 Histopathological examination. (A) Control mice that were injected with Raji cells and treated with PBS developed metastatic tumors in the liver (2 mice found with tumors/4 mice examined), lung (3/4), and brain (1/4), as demonstrated by invasion of monomorphic lymphoma cells (red asterisks) and disruption of normal tissue architecture. (B) Three doses of the consecutive treatment of Fab'-MORF1 and P-MORF2 (Cons ×3) resulted in no evidence of lymphoma invasion (0/3, for all organs). (C) Three doses of the premixed treatment (Prem ×3) prevented lymphoma dissemination (0/3, for all organs). Hematoxylin and eosin (H&E)-stained tissue specimens were examined by a blinded veterinary pathologist. No toxicity of the treatment was suggested in any of the organs evaluated.

Table 3.1 Comparison of anti-B-NHL efficacies (coiled-coil vs. morpholino).

In Vitro* – Apoptotic Index				
	CCE/CCK	MORF1/MORF2		
Consecutive	(1 μM, valence=9)	(0.5 μM, valence=3)	(1 μM, valence=3)	(0.5 μM, valence=9)
	12%	23%	37%	50%
Premixed	(1 μM, valence=9)	(0.5 μM, valence=3)	(1 μM, valence=3)	(0.5 μM, valence=9)
	16%	17%	39%	43%
***In Vivo* – Median Survival Time†**				
	CCE/CCK	MORF1/MORF2		
Consecutive	(1 nmol, 1:25)	(1 nmol, 1:1)		
	50 days	81 days		
Premixed	(1 nmol, 1:25)	(1 nmol, 1:1)		
	55 days	78 days		

*Apoptotic index (%) of Raji cells assessed by annexin V assay. Concentrations of Fab' and valences of polymer conjugates are listed; comparison at time intervals corresponding to maximum apoptosis.

† Median survival (day) of mice bearing systemic B-cell lymphoma and exposed to different treatments.

CHAPTER 4

A TWO-STEP PRETARGETED NANOTHERAPY FOR CD20 CROSSLINKING MAY ACHIEVE SUPERIOR ANTI-LYMPHOMA EFFICACY TO RITUXIMAB[1]

The use of rituximab, an anti-CD20 mAb, in combination with chemotherapy is the current standard for the treatment of B-cell lymphomas. However, because of a significant number of treatment failures, there is a demand for new, improved therapeutics. We designed a nanomedicine that crosslinks CD20 and directly induces apoptosis of B-cells without the need for toxins or immune effector functions. The therapeutic system comprises a pretargeting component (anti-CD20 Fab' conjugated with an oligonucleotide1) and a crosslinking component (HPMA copolymer grafted with multiple complementary oligonucleotide2). Consecutive treatment with the two components resulted in CD20 clustering on the cell surface and effectively killed malignant B-cells *in vivo*. Here, to enhance therapeutic efficacy, a two-step pretargeting approach is employed. We show that the time lag between the two doses can be optimized based on pharmacokinetics and biodistribution of the Fab'-oligonucleotide1 conjugate. In a mouse model of human non-Hodgkin lymphoma (NHL), increasing the

[1]This chapter is adapted from the following publication: T.-W. Chu, R. Zhang, J. Yang, M. P. Chao, P. J. Shami and J. Kopeček. A two-step pretargeted nanotherapy for CD20 crosslinking may achieve superior anti-lymphoma efficacy to rituximab. *Theranostics*. 2015; 5(8): 834–846. Ivyspring.

time lag from 1 h to 5 h resulted in dramatically improved tumor growth inhibition and animal survival. When the 5 h interval was used, the nanotherapy was more efficacious than rituximab and led to complete eradication of lymphoma cells with no signs of metastasis or disease recurrence. We further evaluated the nanomedicine using patient mantle cell lymphoma cells; the treatment demonstrated more potent apoptosis-inducing activity than rituximab hyper-crosslinked with secondary antibodies. In summary, our approach may constitute a novel treatment for NHL and other B-cell malignancies with significant advantages over conventional chemo-immunotherapy.

4.1 Background

Non-Hodgkin lymphoma (NHL) is a prevalent cancer with an around 70,000 projected new cases in 2014 in the United States.[1] Approximately 85% of NHLs arise from B-lymphocytes, and the rest are of T-cell origin. Rituximab, an anti-CD20 monoclonal antibody (mAb), was approved in 1997 for the treatment of B-cell NHL and remains one of the best-characterized antibodies in cancer immunotherapy.[2] The current standard for the treatment of most B-cell NHLs is rituximab in combination with chemotherapy. However, in spite of significant success with this approach, primary resistance and relapse remain a problem.[3] This has been attributed to the inability of immune effector cells to hyper-crosslink ligated mAbs,[4,5] and Fc receptor (FcR)-mediated endocytosis[6] or "trogocytosis"[7] of CD20 antigens. These clinical problems warrant the development of new, improved therapeutic strategies.

CD20 is one of the most reliable biomarkers of B-lymphocytes. It is a noninternalizing[8] or slowly internalizing[9,10] receptor, highly expressed on the surfaces of

most malignant B-cells, as well as normal B-cells. However, CD20 is not expressed on stem cells and mature plasma cells.[11] Consequently, therapeutics targeting CD20 are safe because normal B-cells can be restored after treatment. It is a well-established fact that crosslinking of CD20 at the surface of B-cells induces apoptosis.[12] One widely accepted model suggests that when CD20-bound antibodies are hyper-crosslinked by FcR-expressing immune effector cells (*e.g.*, macrophages, natural killer cells), the clustered CD20 tend to redistribute at the cell surface and become localized to lipid rafts.[13] Such events mediate the interaction of CD20 with Src-family kinases that are also located in lipid rafts, and trigger apoptotic signaling.[14] Without hyper-crosslinking, apoptosis initiated by ligated mAbs is very limited.[15]

Based on the above-mentioned mechanism, we designed a biomimetic therapeutic system (Figure 4.1) that crosslinks CD20 and directly induces apoptosis of lymphoma B-cells without the need for chemotherapeutic agents, toxins or immune effector functions. The therapeutic system is composed of two macromolecular conjugates: (1) Fab'-MORF1: anti-CD20 Fab' attached to a morpholino oligonucleotide, MORF1, and (2) P-MORF2: a linear *N*-(2-hydroxypropyl)methacrylamide (HPMA) polymer (P) backbone grafted with multiple copies of the complementary oligonucleotide, MORF2. We have previously shown that exposure of the human NHL B-cell line Raji to the first conjugate (Fab'-MORF1) decorated the cell surface with MORF1 *via* CD20 binding; further treatment of the cells with the second conjugate (P-MORF2) resulted in MORF1/MORF2 hybridization at the cell surface, which mediated CD20 crosslinking and induced apoptosis *in vitro* and *in vivo*.[16] We named the designed platform "drug-free macromolecular therapeutics" because it does not contain small-molecule cytotoxic

compounds (*e.g.*, chemotherapeutics) and the individual components do not have apoptosis-inducing activity.[17,18] This new therapeutic approach aims to selectively target B-cells for direct apoptosis induction. It has the potential to improve outcomes currently obtained with conventional chemo-immunotherapy.

A significant advantage of the designed "two-step" therapeutics (*i.e.*, consecutive administration of Fab'-MORF1 followed by P-MORF2) is the opportunity of pretargeting. Pretargeting is an approach used in cancer radio-immunotherapy, by which targeting functionality and therapeutic modalities are separated in order to achieve desirable pharmacokinetic (PK) goals and reduce adverse side reactions.[19] With the help of modern nanotechnology, the concept of pretargeting has been expanded in recent years and applied in such strategies as amplified therapeutic delivery[20] and universal targeting of different tumor ligands.[21] In the work presented here, Fab'-MORF1 and P-MORF2 are used as a pretargeting dose and a crosslinking dose (effector), respectively. We hypothesized that the time lag between the two doses could be optimized based on PK and biodistribution of the first dose (Fab'-MORF1), in order to achieve maximal tumor-to-tissue accumulation in individual patients. This approach would enable more efficient treatment and limit potential side effects associated with off-target binding.

In this chapter, we show the development and preclinical evaluation of drug-free macromolecular therapeutics for B-cell lymphomas. *In vivo* therapeutic efficacy was evaluated in mice using a luciferase-based imageable model of human B-cell NHL. The two-step pretargeting approach was employed where the time lag was optimized after determining the PK and biodistribution of Fab'-MORF1. The designed therapeutic system was compared with rituximab in mouse xenografts and against patient NHL cells in order

to test its potential for clinical translation.

4.2 Materials and Methods

4.2.1 Preparation of Fab'-MORF1 and P-MORF2

A pair of 25 bp morpholino oligonucleotides (MORF1 and MORF2) with 3' primary amine modification was purchased from Gene Tools. MORF1 was modified with succinimidyl-4-(*N*-maleimidomethyl)cyclohexane-1-carboxylate (SMCC) and then conjugated to the Fab' fragment of the 1F5 mAb (IgG2a) *via* thiol-ene reaction. The second conjugate was obtained in two steps: The polymeric precursor was first synthesized by reversible addition-fragmentation chain transfer (RAFT) copolymerization of HPMA and *N*-methacryloylglycylglycine thiazolidine-2-thione (MA-GG-TT). Then, the complementary MORF2 was grafted to the copolymer backbone *via* amide linkage. Both conjugates were purified by size exclusion chromatography.[16] For detailed procedures, see *Chapter 3, Subsections 3.2.1* and *3.2.2*.

4.2.2 Cell Lines

Burkitt's B-lymphoma cell line Raji was purchased from the American Type Culture Collection (ATCC). ATCC confirmed this line tested positive for the presence of Epstein Barr viral DNA sequences *via* PCR. Luciferase-expressing Raji cell line (Raji-luc) was generated as previously described.[22] Raji-luc harbors a dual reporter gene L2G (Luc-2A-eGFP) containing a modified firefly luciferase gene joined to eGFP at the 3' end. The L2G construct was ligated into the pCDH-CMV-MCS lentiviral cDNA expression vector (System Biosciences).

4.2.3 Confocal Fluorescence Microscopy

Raji cell line was cultured in RPMI-1640 medium (Sigma) supplemented with 10% fetal bovine serum (HyClone) at 37 °C in a humidified atmosphere with 5% CO_2 (v/v). Experiments were performed using cells in exponential growth phase. Cells at a density of 10^5 per well were incubated with 0.5 mL rhodamine-labeled Fab'-MORF1 (1 μM) in culture medium at 37 °C for 1 h; then, the cells were washed twice with PBS prior to incubation with 0.5 mL of FITC-labeled P-MORF2 (1 μM, MORF2 equivalent) or FITC-labeled P-scMORF2 (1 or 5 μM, MORF eqv.) for another 1 h. Conjugates P-MORF2 and P-scMORF2 were prepared from the same polymer backbone and had a similar valence (~5 oligos/chain). After the incubation, cells were washed twice with PBS, and plated onto sterile 35-mm glass bottom dishes with 14-mm microwells (MatTek Corporation) for imaging. An Olympus laser scanning confocal microscope (FV 1000) was used. Please note that all other experiments (except confocal microscopy) were performed with P-MORF2 containing 9 oligonucleotides/chain. For the CD20 preblocking control studies, all conditions were kept the same, except that the cells were pretreated for 1 h with excess amounts of a mouse anti-human CD20 mAb, 1F5.[23]

4.2.4 Pharmacokinetics and Biodistribution Studies

4.2.4.1 Radiolabeling of Fab'-MORF1

Iodine-125 labeling of the Fab'-MORF1 conjugate was performed immediately before use. $Na^{125}I$ (PerkinElmer) was reacted with Fab'-MORF1 in 10 mM PBS (pH 7.4) in a precoated iodination tube (Thermo Scientific). The reaction mixture was gently stirred at room temperature for 10 min, followed by purification with a Sephadex PD-10

column (GE Healthcare) and then a Millipore® ultrafiltration tube (30 kDa cut-off). The specific radioactivity of the hot samples was in the range of 1.6–2.2 mCi/mg.

4.2.4.2 Pharmacokinetics

Female C.B-17 SCID mice (6- to 8-week-old; 18–20 g; Charles River Laboratories) were used in all the following animal experiments in this chapter. Mice (*n* = 5) were intravenously injected with ^{125}I-labeled Fab'-MORF1 (20 μCi per mouse; 1 nmol Fab' equivalent; 58 μg). At predetermined time intervals, 10 μL blood samples were collected from tail vein, and the radioactivity of each sample was measured with a Gamma Counter (Packard). The blood pharmacokinetic parameters were analyzed using a two-compartment model with WinNonlin 5.0.1 software (Pharsight).

4.2.4.3 Biodistribution

Mice were intravenously injected with 4×10^6 Raji cells (in 200 μL PBS) *via* the tail vein. At day 1 or 7 postinoculation, mice were i.v. administered with ^{125}I-Fab'-MORF1 (20 μCi; 58 μg). Healthy mice (without Raji cells injected) were also given the same dose of ^{125}I-Fab'-MORF1 as controls. At 1 h or 5 h postadministration of conjugates, mice (*n* = 4 per group) were sacrificed. Various organs and tissues were harvested, weighed, and counted for radioactivity with a Gamma Counter. Uptake of conjugates was calculated as the percentage of the injected dose per gram of organs or tissues (% ID/g).

4.2.5 Fluorescence Molecular Tomography (FMT) Imaging

Raji cells were stained with 10 μM DiR (1,1'-dioctadecyl-3,3,3',3'-tetramethyl indotricarbocyanine iodide) (PerkinElmer) at 37 °C for 20 min. Following staining, cells were washed twice with cold PBS. Four million DiR-labeled Raji cells (in 200 μL PBS; used immediately after stained) were injected into mice (n = 4) *via* the tail vein. At 24 h postinoculation, the mice were sacrificed, and various organs and tissues were harvested. The fluorescence signals of these organs and tissues were measured using an FMT camera (PerkinElmer) equipped with a 745 nm laser. Total signal intensities (count/energy) of each organ or tissue were quantified. Healthy mice (without tumor) were used as controls (n = 4).

4.2.6 *In Vivo* Anti-Lymphoma Efficacy Study

Mice were injected *via* the tail vein with 4×10^6 Raji-luc cells. One week later, the inoculated mice were divided into groups (n = 6 or 7) and administered *via* the tail vein with three doses of different treatments (in 100 μL PBS) every other day. These treatments were: (1) PBS (100 μL), (2) Rituxan® (Genentech/Biogen Idec; 75 μg/20 g), (3) 1F5 mAb (75 μg/20 g), (4) Fab'-MORF1 (58 μg/20 g; 1 nmol MORF1) followed by P-MORF2 (119 μg/20 g; 5 nmol MORF2), 1 h interval, and (5) same as (4) but with 5 h interval. Mice were sacrificed at the onset of paralysis or when the body weight dropped below 80% of the baseline; otherwise, the mice were maintained until 125 days and considered long-term survivors.

4.2.7 Bioluminescence Imaging

Imaging of luciferase-expressing Raji lymphoma was performed *in vivo* and *ex vivo*, as previously described.[22] Female C.B-17 SCID mice (6- to 8-week-old; 18–20 g; Charles River Laboratories) were intravenously engrafted with 4×10^6 Raji-luc cells *via* the tail vein and underwent different treatments as above-mentioned. *In vivo* imaging was performed twice per week on weeks 1–4 and once per week on weeks 5–7. Mice were anesthetized with 2% (v/v) isoflurane gas (IsoFlo®, Abbott Laboratories) in oxygen from a precision vaporizer and intraperitoneally injected with 3 mg firefly D-luciferin (Biosynth). At 15 min postinjection of luciferin (a predetermined time interval, with maximal luciferase signal intensity), mice were scanned in the prone position. Xenogen IVIS® Spectrum (Perkin Elmer) was used, with 1 min exposure time, medium binning, and 1 f/stop. Images were acquired and analyzed under the Living Image® (Perkin Elmer) software environment. Region of interest (ROI) was selected by drawing contours to include the whole mice. Luciferase light unit was quantified in average radiance (photons/sec/cm^2/sr). For *ex vivo* analysis, mice were injected with 3 mg luciferin 12 min prior to being sacrificed. Various organs and tissues (heart, liver, spleen, kidney, lung, intestine, stomach, muscle, brain, spinal cord, femur, tibia, and mesenteric and inguinal lymph nodes) were harvested for imaging. Acquisition parameters were as follows: 1 min exposure time, small binning, and 1 f/stop.

4.2.8 Microcomputed Tomography (MicroCT) Imaging

In vivo microCT imaging of mice was performed on week 10 after tumor implantation. Mice were anesthetized with 2% (v/v) isoflurane gas in oxygen and

positioned left lateral on the scanner bed. The hind limbs of mice were scanned using a high-resolution microCT Quantum FX system (Perkin Elmer) at 90 keV and 160 mA, with a field of vision (FOV) of 24 mm. The acquisition time was 4.5 min. Three-dimensional (3D) reconstruction of bone architecture was performed under a Quantum FX viewer 1.3.0 software environment (Perkin Elmer). All above animal experiments were performed according to the protocol approved by the Institutional Animal Care and Use Committee (IACUC) of the University of Utah.

4.2.9 Flow Cytometry Analysis of Femoral Bone Marrow Cells

After mice were sacrificed, fresh femurs (from both hind limbs) were purged with 1 mL PBS to obtain bone marrow cells. The suspension was passed through a 70-μm Falcon^{TM} cell strainer (BD Biosciences), followed by centrifugation (200 g, 5 min) and resuspension in 5 mL red blood cell lysis buffer. The suspension was incubated at room temperature for 5 min and washed/resuspended in cold PBS. Allophycocyanin (APC)-labeled mouse anti-human CD19 antibody (IgG1, κ isotype; BD Biosciences) (10 μL) was added to 100 μL single-cell suspension containing about 10^6 cells.[24] Cells were incubated for 45 min at 4 °C in the dark, and washed with 1.5 mL PBS prior to analysis. For flow cytometry, data of 5×10^5 cells were recorded.

4.2.10 Patient Samples Analysis and Apoptosis Assay

Leukocytes were isolated from four previously untreated mantle cell lymphoma (MCL) patients following ammonium chloride lysis. Two isolates were from lymph node biopsies (patients 1 and 2) and two were from the peripheral blood (patients 3 and 4). The

isolated cells harbor the t(11;14) chromosomal translocation, a typical MCL phenotype. Specimens were collected after informed consent under a protocol approved by the University of Utah Institutional Review Board. Primary cells (2×10^5) were suspended in 0.4 mL RPMI-1640 medium (Sigma) supplemented with 10% fetal bovine serum (Hyclone) and treated consecutively (1 h or 5 h interval) with Fab'-MORF1 and P-MORF2 (at equimolar MORF1/MORF2 concentrations). Untreated cells in the culture medium were used as negative controls. For positive controls, cells were treated consecutively (identical time intervals) with anti-CD20 mAbs (1F5 or rituximab) and a goat anti-mouse secondary antibody (KPL) (molar ratio mAb:2°Ab = 2:1). Incubation was carried out for 24 h at 37 °C in a humidified atmosphere with 5% CO_2. All experiments were conducted in duplicate or triplicate wells. After treatments, cells were washed twice with PBS prior to staining by propidium iodide (PI) and FITC-labeled annexin V. Staining was performed following the RAPID™ protocol provided by the manufacturer (Oncogene Research Products). Percentage of total apoptotic cells (annexin V^+ PI^+ + annexin V^+ PI^-) was quantified by flow cytometry where data of 10^4 cells were recorded.

4.2.11 Statistical Analysis

Statistics were performed by Student's *t*-test to compare two groups, or one-way analysis of variance (ANOVA) to compare three or more groups (with p value < 0.05 indicating statistical significance). Animal survival analysis was performed with the log-rank test using the GraphPad Prism 5 software.

4.3 Results

4.3.1 Conjugates Fab'-MORF1 and P-MORF2 were Successfully Synthesized

The morpholino oligonucleotide pair, MORF1 and MORF2 (Figure 4.1), were 25 bp and both about 8.5 kDa. Their base sequences were designed to achieve optimal binding and solubility, and to avoid self-complementarity and off-target binding with human and murine mRNA.[16] The 3'-primary amine was used for conjugation to Fab' or the polymer backbone. The Fab' fragment was from a mouse anti-human CD20 mAb, 1F5.[23] MORF1 was tethered to the terminal thiol of Fab' *via* a thioether bond. This site-specific conjugation would prevent undesirable impact on antigen binding. The coupling reaction followed a 1:1 stoichiometry; molecular weight of the conjugate was 57.5 kDa (see *Chapter 3, Subsection 3.3.2*). The hydrodynamic effective diameter of Fab'-MORF1 was 9 nm, as characterized by dynamic light scattering (Figure 4.2).

To prepare the multivalent P-MORF2 conjugate, we first synthesized a copolymer of HPMA with MA-GG-TT by RAFT polymerization.[25] The copolymer contained multiple side chains terminated in (amine-reactive) thiazolidine-2-thione groups and possessed a narrow distribution of molecular weights as determined by size exclusion chromatography (number average molecular weight, Mn = 136 kDa; polydispersity, Pd = 1.15). Then, the MORF2 oligonucleotides (containing a 3'-primary amine) were attached to the HPMA copolymer side chains *via* amide bonds. The valence (*i.e.*, number of oligonucleotide grafts per polymer chain) of the P-MORF2 was 9. The hydrodynamic effective diameter of P-MORF2 was about 19 nm (Figure 4.2).

4.3.2 Fab'-MORF1 and P-MORF2 Self-Assembled on the Surface of NHL B-Cells

We have previously shown that the MORF1–MORF2 hybridization was fast (< 10 min) and stable (Tm = 59 °C) after conjugation to Fab' and the polymer.[16] When the two conjugates were mixed at equimolar MORF1/MORF2 concentration, a near 100% binding between Fab'-MORF1 and P-MORF2 was observed (Figure 4.3). This indicated highly efficient *in vitro* self-assembly of the two conjugates. We further determined the cell surface biorecognition of the two conjugates by confocal microscopy (Figure 4.4). In these experiments, Fab'-MORF1 was labeled with rhodamine (red), and P-MORF2 was labeled with FITC (green). Results showed that Fab'-MORF1 successfully decorated the surfaces of Raji cells (a human NHL B-cell line) *via* CD20 binding (Figure 4.4A). Preblocking of the CD20 receptors at cell surfaces with an excess amount of 1F5 mAb resulted in no red signal decoration after the Fab'-MORF1 treatment. Furthermore, consecutive exposure of Raji cells to Fab'-MORF1 followed by P-MORF2 led to both the red and green signal decoration at the cell surface (Figure 4.4B). This was mediated by the MORF1/MORF2 hybridization, as confirmed by controls using an HPMA copolymer labeled with FITC and grafted with multiple copies of a scrambled sequence of MORF2 (scMORF2). The polymer (P)–scMORF2 control conjugate, even in excess amounts, failed to bind to the surfaces of the MORF1-decorated B-cells, due to absence of the biorecognition pair. These data suggested that Fab'-MORF1 and P-MORF2 self-assemble on the surfaces of lymphoma B-cells with high functional specificity.

4.3.3 PK and Biodistribution Suggested an Optimal Time Lag of 5 Hours for Efficient Tumor Pretargeting

We planned to employ the two-step pretargeting strategy in the *in vivo* therapy experiments. Therefore, we analyzed the PK and biodistribution of the pretargeting dose, Fab'-MORF1, in order to determine the optimal time lag. The blood radioactivity versus time profile of the ^{125}I-labeled Fab'-MORF1 conjugate in mice is illustrated in Figure 4.5A, and the PK parameters are summarized in Figure 4.5B. Results showed that Fab'-MORF1 had a terminal plasma half-life of about 5 h, which was longer than the half-lives of other Fab' fragments of IgG antibodies.[26] This was possibly due to the attachment of MORF1 since the PK of antibody fragments without Fc is molecular weight (MW)-dependent.[27] Importantly, at about 5 h after intravenous injection, Fab'-MORF1 reached a plateau or steady blood concentration, indicating a suitable timing for P-MORF2 administration. At that point, most Fab'-MORF1 were cleared from the blood or distributed to tumors and tissues. Consequently, at this time point there were minimal free conjugates in the blood (unbound to B-cells) that would interfere with the hybridization when P-MORF2 is administered. Based on this result, we hypothesized that, by using a time lag of 5 h, the pretargeting and second-step targeting can be more effective, and the therapeutic efficacy of drug-free macromolecular therapeutics can be improved over our previous experimental conditions that used a 1 h interval.[16]

To further support this hypothesis, we compared the biodistribution of Fab'-MORF1 at 1 h and 5 h (Figure 4.5C). The studies were performed in healthy SCID mice (no tumor), as well as SCID mice bearing systemically injected Raji B-cells (tumor). We first used fluorescence molecular tomography (FMT) imaging to determine the "hot

spots" of Raji lymphoma dissemination (Figure 4.5D); tumors were found abundantly in the tibiae, femora, spine, and lymph nodes, which is in agreement with previous reports.[28] Results of biodistribution showed that 5 h after intravenous injection, Fab'-MORF1 indeed had a better tumor pretargeting efficiency when compared to 1 h postinjection. As shown in Figure 4.5C, at 5 h, significantly more conjugates were found in the tibiae, femora, and lymph nodes of the tumor-engrafted mice, when compared to 1 h postinjection. These organs with substantially more uptake of Fab'-MORF1 matched with the Raji lymphoma tumor sites (as determined by FMT; Figure 4.5D). Furthermore, in order to define tumor-specific uptake of Fab'-MORF1 (Figure 4.5E), the mean radioactivity (^{125}I) in each organ of healthy mice (no tumor; background) was subtracted from the radioactivity of corresponding organs of the tumor-bearing mice. The increase from the background indicated tumor-specific uptake of the conjugates. This analysis suggested significantly more Fab'-MORF1 tumor uptake at 5 h, when compared to 1 h. Differences were statistically significant (5 h vs. 1 h) for all lymphoma hot spots (tibia, femur, spine, and lymph node) ($p < 0.05$), but not for organs without tumors (*e.g.*, brain, muscle, and intestine). These data confirmed that, in this animal model, an optimal time lag of 5 h was suitable for tumor pretargeting of Fab'-MORF1.

Interestingly, we observed less accumulation of Fab'-MORF1 at 5 h (vs. 1 h) in several major organs, including the liver, kidneys, and lungs (Figure 4.5C), suggesting a lower chance of off-target binding after the administration of P-MORF2 (effector). This observation further strengthens the rationale of using 5 h as an optimal time lag. The biodistribution results were concordant with the PK data, which confirmed significant blood clearance of Fab'-MORF1 conjugates from 1 h (~18% ID/g) to 5 h (~5% ID/g for

healthy mice). In addition, at 5 h, mice bearing tumors had more conjugates in the blood (~10% ID/g) when compared to mice without tumors (~5% ID/g). This phenomenon likely resulted from Fab'-MORF1 targeting to the circulating lymphoma B-cells in the blood. The biodistribution study was performed on day 7 after tumor inoculation of mice; similar trends were also observed at day 1 after tumor inoculation. However, the tumor pretargeting efficiency was apparently better on day 7 (Figure 4.5C) when compared to day 1, presumably due to more pronounced tumor dissemination and infiltration on day 7.

4.3.4 Pretargeted Nanotherapeutics Showed *In Vivo* Anti-Lymphoma Efficacy that is Superior to Rituximab

We used an imageable mouse model of systemically disseminated human B-cell lymphoma for preclinical evaluation of drug-free macromolecular therapeutics (Figure 4.6). Luciferase-labeled Raji cells (Raji-luc) were engrafted intravenously into adult SCID mice, which have functional macrophages, natural killer cells and complement. One week after tumor inoculation, mice were administered three doses of different treatments every other day. Administration time and doses were based on a preliminary experiment (Figure 4.7) and our previous studies.[16,29] In this animal model, the hind-limb paralysis-free survival time reflects the therapeutic efficacy.[28–30] Luciferase imaging can be performed *in vivo* to determine tumor engraftment, dissemination, and growth/inhibition.[22] Here, we employed the two-step pretargeting strategy where Fab'-MORF1 and P-MORF2 were administered (*via* the tail vein) consecutively, using 1 h or 5 h as an interval. These two nanomedicine groups (Cons 1h, Cons 5h) were compared side-by-side with the immunotherapy control (1F5 mAb) and a clinically used anti-CD20

mAb, rituximab. The animal survival curve is shown in Figure 4.6A. Data showed that mice in the placebo group (PBS) rapidly developed hind-limb paralysis within 4 weeks after tumor injection; the median survival time was 25 days (0% survival). The designed nanomedicine using the 1 h interval (Cons 1h) substantially prolonged animal survival, resulting in a median survival of 55 days (14% survival; $p = 0.003$ compared to PBS). The therapeutic efficacy of Cons 1h was comparable to a Fab'-equivalent dose of rituximab, which had a median survival of 72 days (17% survival; $p = 0.772$ compared to Cons 1h). Importantly, when the 5 h interval (previously optimized time lag) was used, the nanomedicine achieved a significantly improved anticancer efficacy over the 1 h treatment ($p = 0.008$). This optimized treatment regimen (Cons 5h) produced an 83% animal survival, which was comparable to the immunotherapy control (1F5 mAb; $p = 0.317$) and was significantly better than rituximab ($p = 0.009$).

The *in vivo* tumor imaging studies (Figures 4.6B and 4.6C) were in agreement with the animal survival. Bioluminescent images of mice (on day 25) are shown in Figure 4.6B. These images demonstrate B-cell lymphoma dissemination in various organs, including the spine, femora and tibiae. Furthermore, whole-body bioluminescent intensities of mice were quantified to compare groups; the averaged tumor signal versus time profiles are illustrated in Figure 4.6C. The negative control mice (PBS) showed a rapid progression of tumor burden after 10 days. At day 25, the luciferase signals in the PBS group reached saturation. Our drug-free nanotherapeutic using the 1 h interval (Cons 1h) had a moderate effect of tumor inhibition, which was comparable to rituximab. The progression of lymphoma in these two groups (Cons 1h, Rituximab) was significantly delayed when compared to the placebo group. When the 5 h interval was used, the

nanomedicine (Cons 5h) showed a substantial improvement over the 1 h treatment, leading to complete elimination of tumor load in 5 (out of 6) animals. At day 49, the average luciferase signal of Cons 5h was similar to the background and was significantly lower than Cons 1h (p = 0.004). Although there is no difference between Cons 5h and 1F5 mAb in tumor inhibition and animal survival, the anti-lymphoma efficacy of the designed nanotherapeutic, unlike mAbs, is independent of immune effector mechanisms, such as antibody-dependent cellular cytotoxicity (ADCC) and complement-dependent cytotoxicity (CDC),[31] and is a direct result of only apoptosis.

We also performed three-dimensional microcomputed tomography (3D microCT) imaging on the mice that bore Raji-luc lymphoma xenografts and underwent different treatments (Figure 4.8). These images were focused on the lumbar spine and hind limbs (hot-spots of B-cell NHL metastasis). Results revealed extensive bone destruction in the rituximab-treated mice and moderate bone lesions in the mice administered drug-free nanotherapeutics using the 1 h interval (Cons 1h). Observed bone heterogeneity was extensive in the femur, and in some cases, the proximal tibia (close to the knee joint), indicating abnormal osteoclast activation (bone remodeling) stimulated by lymphoma metastases.[32] However, no signs of bone remodeling were found in mice treated with Cons 5h. Taken together, superior anti-lymphoma efficacy was achieved using the 5 h interval treatment, when compared to the 1 h treatment and rituximab. These results validate our hypothesis that 5 h is optimal for efficient pretargeting/2nd-step targeting in drug-free macromolecular therapeutics.

4.3.5 Optimized Nanotherapy Completely Eradicates Lymphoma Cells in 83% of Mice

Ex vivo luciferase imaging was performed to examine tumors in multiple organs and tissues (Figure 4.9A). Results were concordant with *in vivo* imaging and showed that Raji-luc lymphoma cells readily infiltrated in the femora, tibiae and lymph nodes of the negative control mice (PBS). Extensive infiltration of the spinal cord was also seen in the control animals, likely accounting for the occurrence of hind-limb paralysis.[28] However, most of the surviving mice (5 out 6) that were treated with the nanomedicine using a 5 h interval (Cons 5h) were completely tumor-free. Furthermore, we used flow cytometry to quantitatively analyze residual lymphoma B-cells in the femoral bone marrow (BM) of mice (Figures 4.9B and 4.9C). Raji-luc cells harbor a dual reporter expressing both luciferase and green fluorescence protein (GFP).[22] We additionally stained the cells with an anti-human CD19 antibody[24] and analyzed the percentage of GFP^+ $CD19^+$ cells. Results showed that the negative control mice (PBS) harbored substantial amounts of Raji-luc cells in the bone marrow (average 6.4%). The mice treated with the nanomedicine using a 1 h interval (Cons 1h) demonstrated significant improvement (average 2.7%). In the group that was treated using optimized treatment conditions (Cons 5h), all mice, including 5 long-term survivors and 1 animal sacrificed on day 105 due to a large abdominal tumor, had 0% lymphoma B-cells in the bone marrow. Histopathological examination further confirmed that the long-term surviving mice were tumor-free and suggested no acute or chronic toxicity caused by drug-free macromolecular therapeutics in any of the tissues evaluated, which corresponded to a stable body weight growth. These results demonstrate excellent anti-NHL efficacy of the nanotherapeutics with the

two components (Fab'-MORF1 and P-MORF2) administered at an optimal interval of 5 h. A low dose (58 μg × 3) of the pretargeting agent with a 5× excess of effectors was able to completely eradicate lymphoma B-cells in mice and was not toxic to normal tissues.

4.3.6 Drug-Free Nanotherapeutic Showed Higher Potency than Rituximab in NHL Patient Specimens

To further evaluate the clinical potential of the designed nanomedicine, primary cells were isolated from 4 mantle cell lymphoma (MCL) patients. MCL is an aggressive and incurable subtype of B-cell NHL. We treated the cells consecutively with Fab'-MORF1 and P-MORF2, as well as rituximab (or 1F5 mAb) hyper-crosslinked with secondary antibodies. The purpose of using secondary antibodies is to reproduce the function of FcR^+ immune effector cells, which partly reflects the *in vivo* therapeutic efficacy of anti-CD20 mAbs.[12] Results showed that the designed nanomedicine effectively induced apoptosis of MCL cells from all 4 patients (Figure 4.10). The percent of apoptotic cells was increased by about 2 fold when compared to the untreated cells. When compared to mAbs, the nanomedicine demonstrated superior apoptosis-inducing activity to rituximab in all 4 patient samples, and to 1F5 mAb in 1 sample (patient 1). In patient 3, we observed an increase of apoptotic index with increasing concentration for all compounds tested. The efficacy of 1F5 and rituximab seemed maximized at 1 μM, whereas the nanomedicine reached maximal apoptosis induction at a lower concentration (0.5 μM). In patient 4, we employed two different time intervals (1 h and 5 h) between the treatments. Data showed that, when the time lag was increased from 1 h to 5 h, there was no change in efficacy for the nanomedicine. However, for both mAbs, the apoptosis-

inducing activity dropped when the longer time interval was used. This phenomenon can be attributed to Fc-mediated endocytosis of the mAb/CD20 complex, which was observed elsewhere by other investigators.[6] These results highlight the potential of drug-free macromolecular therapeutics as a novel and potent treatment against B-cell lymphomas.

4.4 Discussion

Data presented here validated the proposed concept and showed that the anti-lymphoma efficacy of the designed nanomedicine was significantly better than rituximab, the most frequently used anti-CD20 mAb in the clinic, while also being comparable to 1F5. In mice, the better efficacy of 1F5 (mouse mAb) when compared to rituximab (human/mouse hybrid mAb) was likely due to stronger binding of the Fc region of 1F5 by (mouse) immune effector cells.[33] It will be interesting to compare our approach with type II anti-CD20 mAbs (*e.g.*, obinutuzumab) that can also induce direct apoptosis.[34] It is worth noting that drug-free macromolecular therapeutics depleted tumors by a single, well-defined mechanism (apoptosis), whereas the efficacy of mAbs is related to apoptosis as well as other effector mechanisms, *e.g.*, ADCC and CDC.[31] We believe that the superior efficacy of our therapeutic results from the multivalent effect, *i.e.*, the P-MORF2 conjugate has multimeric interactions with targets, in contrast to mAbs with only two binding sites. Our laboratory has previously shown that the multivalency of anti-CD20 constructs can magnify binding affinity and apoptosis induction by several fold, when compared to their monovalent or divalent counterparts.[35–37] We have also reported that, in addition to valence, the polymer MW had a positive influence on CD20 clustering and

apoptosis.[37] Thus, it is possible to further improve the efficacy by using P-MORF2 with a higher valence and/or a larger polymer backbone, together with a higher dose of the pretargeting agent.

This research offers a unique new strategy in lymphoma treatment by direct apoptosis induction; no small-molecule toxic drug or immune activation is involved. This approach avoids the severe side effects associated with conventional chemo- and radiotherapy. It has potential to treat or sensitize chemoresistant malignancies.[38] Compared to immunotherapies using anti-CD20 mAbs, the designed nanomedicine kills B-cells without the need for effector cells. This allows us to target diseases that are not responsive to immunotherapy, which constitute about half of all NHL patients.[3] In the clinic, a large population of rituximab nonresponders harbors polymorphism in the IgG Fc receptor (FcR) gene,[4,5] resulting in failure of effector cells to hyper-crosslink ligated mAbs (*via* Fc–FcR binding). Many other cases of mAb nonresponsiveness or resistance are due to CD20 downregulation.[5–7] For instance, repeated treatment of mAbs may lead to CD20 internalization, which is mediated by the inhibitory FcR expressed on the target B-cells themselves.[6] In contrast, once the Fc region was removed, Fab' of the same antibody was found to be noninternalizing.[9] More recently, resistance to rituximab has been attributed to "trogocytosis" (shaving of CD20 antigens from the surfaces of B-cells by macrophages *via* the regulatory FcR).[7] It is noteworthy that all these mechanisms accounting for the nonresponsiveness/resistance are mediated by Fc–FcR recognition between mAbs and immune effector cells. Since our design does not contain Fc fragments, it may circumvent these mechanisms and benefit patients who do not respond to immunotherapy. Furthermore, our nano-sized therapeutic conjugates likely have better

mobility and more rapid tumor penetration when compared to immune effector cells, which is advantageous to target solid tumors that are commonly seen in lymphoma patients.

This preclinical study demonstrated the possibility of optimizing the designed two-step therapeutics based on PK and biodistribution of the pretargeting dose (Fab'-MORF1). The optimized time lag was 5 h after i.v. administration (in female SCID mice); at this time, most Fab'-MORF1 was cleared from the blood and reached a steady plasma concentration (Figure 4.5A) and was efficiently distributed to the tumors (Figure 4.5E). This approach, in combination with imaging methods or with predetermined clinical characteristics of individual patients, can potentially be applied for personalized therapy to enhance therapeutic efficacy. Studies have shown that the pharmacokinetic profile of rituximab differs between responders and nonresponders.[39] Therefore, a two-step pretargeted platform, which offers flexibility to individualize the PK of therapeutic effectors, may benefit patients with inadequate response to mAbs treatment by overcoming the pharmacokinetic limitations. For clinical application, the pretargeting parameters can be more precisely determined with the aid of mathematical modeling.[40] Our approach may constitute a novel personalized nanotherapy for lymphomas and potentially other cancers.

Our approach will ultimately require validation and confirmation in properly conducted clinical trials. Nonetheless, the selection of CD20 as a pharmacological target is validated by extensive prior experience. Our therapeutic effector P-MORF2 will likely result in prolonged B-cell depletion compared to mAbs, due to a long blood circulation time of the HPMA polymer backbone.[41,42] The plasma half-life of P-MORF2 can be

further increased using multiblock backbone degradable HPMA copolymers.[25,43,44] Before translation to the clinic, one major issue to be addressed is potential immunogenicity of the conjugates. Here, the preclinical evaluation was performed in SCID mice, which are severely immunocompromised. It will be important to conduct immunogenicity studies using immunocompetent animals. The HPMA polymer is nonimmunogenic.[45,46] Its safety has been proven in clinical trials.[47] Moreover, conjugation of immunogens to HPMA copolymers reduces the immunogenicity.[45] Therefore, we anticipate that the P-MORF2 conjugate will have a favorable safety profile. Indeed, in the animal experiment performed here, mice were administered three doses of the designed therapeutic containing a total of about 18 mg/kg P-MORF2, and no toxicity has been observed. In the reported system, we used Fab' from a mouse 1F5 mAb;[23] it is likely that when tested in humans, this system will trigger immune responses due to foreign, murine-derived protein fragments (*e.g.*, production of anti-mouse antibodies and the associated allergic or hypersensitivity reactions). Such concerns can be addressed by switching to a humanized anti-CD20 mAb, *e.g.*, ofatumumab, veltuzumab. Alternatively, we shall develop a humanized 1F5 mAb to address this issue.

Besides lymphomas, the therapeutic conjugates developed in this study can also be used for autoimmune diseases, such as rheumatoid arthritis, multiple sclerosis, and systemic lupus erythematosus, as well as chronic lymphocytic leukemia (CLL). All these diseases have been treated by anti-CD20 mAbs.[48,49] Recently, we evaluated the designed therapeutics in patient CLL cells, including high-risk patients with the 17p13 deletion.[50] Results showed that our treatment effectively induced apoptosis of CLL B-cells and led to subsequent cell death, and was more potent than 1F5 mAb. In summary, we have

developed a novel two-step pretargeted nanotherapy for treatments of B-cell malignancies. This approach is more direct and effective than type I anti-CD20 mAbs and possesses significant advantages over conventional chemo-, radio-, and immunotherapy.

4.5 References

1. R. Siegel, J. Ma, Z. Zou and A. Jemal, Cancer statistics, 2014, *CA Cancer J. Clin.*, 2014, **64**, 9–29.

2. D. G. Maloney, *et al.*, IDEC-C2B8 (rituximab) anti-CD20 monoclonal antibody therapy in patients with relapsed low-grade non-Hodgkin's lymphoma, *Blood*, 1997, **90**, 2188–2195.

3. A. Molina, A decade of rituximab: improving survival outcomes in non-Hodgkin's lymphoma, *Annu. Rev. Med.*, 2008, **59**, 237–250.

4. G. Cartron, *et al.*, Therapeutic activity of humanized anti-CD20 monoclonal antibody and polymorphism in IgG Fc receptor FcγRIIIa gene, *Blood*, 2002, **99**, 754–758.

5. M. R. Smith, Rituximab (monoclonal anti-CD20 antibody): mechanisms of action and resistance, *Oncogene*, 2003, **22**, 7359–7368.

6. I. Dransfield, Inhibitory FcγRIIb and CD20 internalization, *Blood*, 2014, **123**, 606–607.

7. T. Pham, P. Mero and J. W. Booth, Dynamics of macrophage trogocytosis of rituximab-coated B cells, *PloS One*, 2011, **6**, e14498.

8. P. Stashenko, L. M. Nadler, R. Hardy and S. F. Schlossman, Characterization of a human B lymphocyte-specific antigen, *J. Immunol.*, 1980, **125**, 1678–1685.

9. R. B. Michel and M. J. Mattes, Intracellular accumulation of the anti-CD20 antibody 1F5 in B-lymphoma cells, *Clin. Cancer Res.*, 2002, **8**, 2701–2713.

10. O. W. Press, A. G. Farr, K. I. Borroz, S. K. Anderson and P. J. Martin, Endocytosis and degradation of monoclonal antibodies targeting human B-cell malignancies, *Cancer Res.*, 1989, **49**, 4906–4912.

11. K. C. Anderson, *et al.*, Expression of human B cell-associated antigens on leukemias and lymphomas: a model of human B cell differentiation, *Blood*, 1984, **63**, 1424–1433.

12. D. Shan, J. A. Ledbetter and O. W. Press, Apoptosis of malignant human B cells by ligation of CD20 with monoclonal antibodies, *Blood*, 1998, **91**, 1644–1652.

13. J. P. Deans, H. Li and M. J. Polyak, CD20-mediated apoptosis: signalling through lipid rafts, *Immunology*, 2002, **107**, 176–182.

14. J. K. Hofmeister, D. Cooney and K. M. Coggeshall, Clustered CD20 induced apoptosis: src-family kinase, the proximal regulator of tyrosine phosphorylation, calcium influx, and caspase 3-dependent apoptosis, *Blood Cells. Mol. Dis.*, 2000, **26**, 133–143.

15. M.-A. Ghetie, H. Bright and E. S. Vitetta, Homodimers but not monomers of Rituxan (chimeric anti-CD20) induce apoptosis in human B-lymphoma cells and synergize with a chemotherapeutic agent and an immunotoxin, *Blood*, 2001, **97**, 1392–1398.

16. T.-W. Chu, J. Yang, R. Zhang, M. Sima and J. Kopeček, Cell surface self-assembly of hybrid nanoconjugates *via* oligonucleotide hybridization induces apoptosis, *ACS Nano*, 2014, **8**, 719–730.

17. K. Wu, J. Liu, R. N. Johnson, J. Yang and J. Kopeček, Drug-free macromolecular therapeutics: induction of apoptosis by coiled-coil-mediated cross-linking of antigens on the cell surface, *Angew. Chem. Int. Ed.*, 2010, **49**, 1451–1455.

18. T.-W. Chu and J. Kopeček, Drug-free macromolecular therapeutics – a new paradigm in polymeric nanomedicines, *Biomater. Sci*., 2015, doi: 10.1039/c4bm00442f.

19. D. A. Goodwin and C. F. Meares, Advances in pretargeting biotechnology, *Biotechnol. Adv.*, 2001, **19**, 435–450.

20. J. J. Mulvey, *et al.*, Self-assembly of carbon nanotubes and antibodies on tumours for targeted, amplified delivery, *Nat. Nanotechnol.*, 2013, **8**, 763–771.

21. J. Gunn, S. I. Park, O. Veiseh, O. W. Press and M. A. Zhang, Pretargeted nanoparticle system for tumor cell labeling, *Mol. Biosyst.*, 2011, **7**, 742–748.

22. M. P. Chao, *et al.*, Anti-CD47 antibody synergizes with rituximab to promote phagocytosis and eradicate non-Hodgkin lymphoma, *Cell*, 2010, **142**, 699–713.

23. O. W. Press, *et al.*, Monoclonal antibody 1F5 (anti-CD20) serotherapy of human B cell lymphomas, *Blood*, 1987, **69**, 584–591.

24. W. C. Chen, G. C. Completo, D. S. Sigal, P. R. Crocker, A. Saven and J. C. Paulson, *In vivo* targeting of B-cell lymphoma with glycan ligands of CD22, *Blood*, 2010, **115**, 4778–4786.

25. H. Pan, J. Yang, P. Kopečková and J. Kopeček, Backbone degradable multiblock *N*-(2-hydroxypropyl)methacrylamide copolymer conjugates *via* reversible addition-fragmentation chain transfer polymerization and thiol-ene coupling reaction, *Biomacromolecules*, 2011, **12**, 247–252.

26. D. G. Covell, J. Barbet, O. D. Holton, C. D. Black, R. J. Parker and J. N. Weinstein, Pharmacokinetics of monoclonal immunoglobulin G1, $F(ab')_2$, and Fab' in mice, *Cancer Res*., 1986, **46**, 3969–3678.

27. M. I. Bazin-Redureau, C. B. Renard and J. M. Scherrmann, Pharmacokinetics of heterologous and homologous immunoglobulin G, $F(ab')_2$ and Fab after intravenous administration in the rat, *J. Pharm. Pharmacol*., 1997, **49**, 277–281.

28. M. A. Ghetie, J. Richardson, T. Tucker, D. Jones, J. W. Uhr and E. S. Vitetta, Disseminated or localized growth of a human B-cell tumor (Daudi) in SCID mice, *Int. J. Cancer*, 1990, **45**, 481–485.

29. K. Wu, J. Yang, J. Liu and J. Kopeček, Coiled-coil based drug-free macromolecular therapeutics: *in vivo* efficacy, *J. Control. Release*., 2012, **157**, 126–131.

30. G. L. Griffiths, *et al.*, Cure of SCID mice bearing human B-lymphoma xenografts by an anti-CD74 antibody – anthracycline drug conjugate, *Clin. Cancer Res.*, 2003, **9**, 6567–6571.

31. M. Okroj, A. Österborg and A. M. Blom, Effector mechanisms of anti-CD20 monoclonal antibodies in B cell malignancies, *Cancer Treat. Rev.*, 2013, **39**, 632–639.

32. G. D. Roodman, Biology of osteoclast activation in cancer, *J. Clin. Oncol*., 2001, **19**, 3562–3571.

33. M. S. Cragg and M. J. Glennie, Antibody specificity controls *in vivo* effector mechanisms of anti-CD20 reagents, *Blood*, 2004, **103**, 2738–2743.

34. S. Herter, *et al.*, Preclinical activity of the type II CD20 antibody GA101 (obinutuzumab) compared with rituximab and ofatumumab *in vitro* and in xenograft models, *Mol. Cancer Ther.*, 2013, **12**, 2031–2042.

35. R. N. Johnson, P. Kopečková and J. Kopeček, Synthesis and evaluation of multivalent branched HPMA copolymer–Fab' conjugates targeted to the B-cell antigen CD20, *Bioconjug. Chem*., 2009, **20**, 129–137.

36. R. N. Johnson, P. Kopečková and J. Kopeček, Biological activity of anti-CD20 multivalent HPMA copolymer–Fab' conjugates. *Biomacromolecules*, 2012, **13**, 727–735.

37. T.-W. Chu, J. Yang and J. Kopeček, Anti-CD20 multivalent HPMA copolymer–Fab' conjugates for the direct induction of apoptosis, *Biomaterials*, 2012, **33**, 7174–7181.

38. L. E. van der Kolk, *et al.*, CD20-induced B cell death can bypass mitochondria and caspase activation, *Leukemia*, 2002, **16**, 1735–1744.

39. G. Cartron, H. Watier, J. Golay and P. Solal-Celigny, From the bench to the bedside: ways to improve rituximab efficacy, *Blood*, 2004, **104**, 2635–2642.

40. G. Liu and D. J. Hnatowich, A semiempirical model of tumor pretargeting, *Bioconjug. Chem*., 2008, **19**, 2095–2104.

41. K. Ulbrich and V. Šubr, Structural and chemical aspects of HPMA copolymers as drug carriers, *Adv. Drug Deliv. Rev.*, 2010, **62**, 150–166.

42. J. Zalevsky, *et al.*, Enhanced antibody half-life improves *in vivo* activity, *Nat. Biotechnol*., 2010, **28**, 157–159.

43. J. Yang, K. Luo, H. Pan, P. Kopečková and J. Kopeček, Synthesis of biodegradable multiblock copolymers by click coupling of RAFT-generated heterotelechelic polyHPMA conjugates, *React. Funct. Polym.*, 2011, **71**, 294–302.

44. R. Zhang, J. Yang, M. Sima, Y. Zhou and J. Kopeček, Sequential combination therapy of ovarian cancer with degradable *N*-(2-hydroxypropyl)methacrylamide copolymer paclitaxel and gemcitabine conjugates, *Proc. Natl. Acad. Sci. U.S.A*., 2014, **111**, 12181–12186.

45. B. Říhová and M. Kovář, Immunogenicity and immunomodulatory properties of HPMA-based polymers, *Adv. Drug Deliv. Rev*., 2010, **62**, 184–191.

46. M. Kverka, J. M. Hartley, T.-W. Chu, J. Yang, R. Heidchen and J. Kopeček, Immunogenicity of coiled-coil based drug-free macromolecular therapeutics, *Biomaterials*, 2014, **35**, 5886–5896.

47. P. A. Vasey, *et al.*, Phase I clinical and pharmacokinetic study of PK1 [*N*-(2-hydroxypropyl)methacrylamide copolymer doxorubicin]: first member of a new class of chemotherapeutic agents-drug-polymer conjugates. Cancer Research Campaign Phase I/II Committee, *Clin. Cancer Res.*, 1999, **5**, 83–94.

48. D. Dierickx, A. Delannoy, K. Saja, G. Verhoef and D. Provan, Anti-CD20 monoclonal antibodies and their use in adult autoimmune hematological disorders, *Am. J. Hematol*., 2011, **86**, 278–291.

49. P. Jain and S. O'Brien, Anti-CD20 monoclonal antibodies in chronic lymphocytic leukemia, *Expert Opin. Biol. Ther*., 2013, **13**, 169–182.

50. T.-W. Chu, K. M. Kosak, P. J. Shami and J. Kopeček, Drug-free macromolecular therapeutics induce apoptosis of patient chronic lymphocytic leukemia cells, *Drug Deliv. Transl. Res*., 2014, **4**, 389–394.

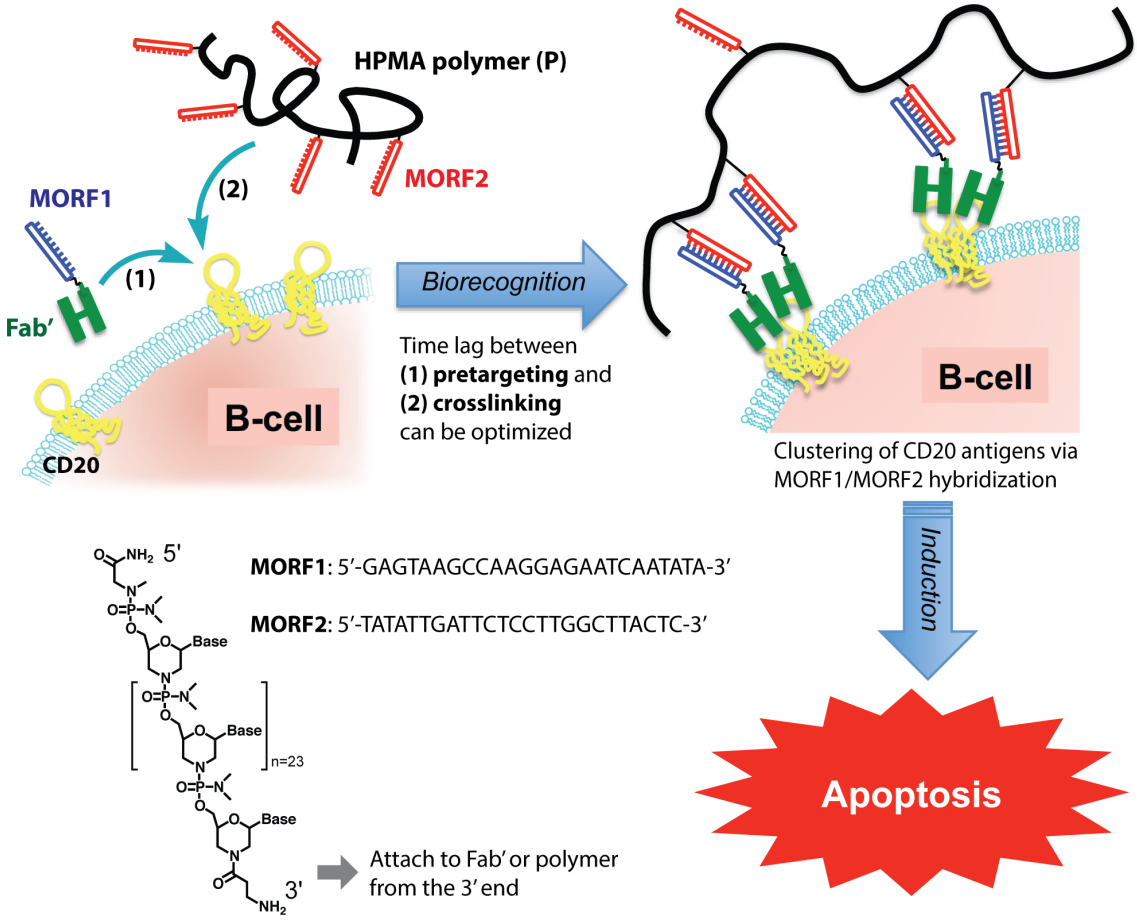

Figure 4.1 Drug-free macromolecular therapeutics by a two-step pretargeting approach. Two macromolecular conjugates, Fab'-MORF1 and P-MORF2, are administered consecutively as the pretargeting dose and the crosslinking dose to induce apoptosis of malignant B-cells.

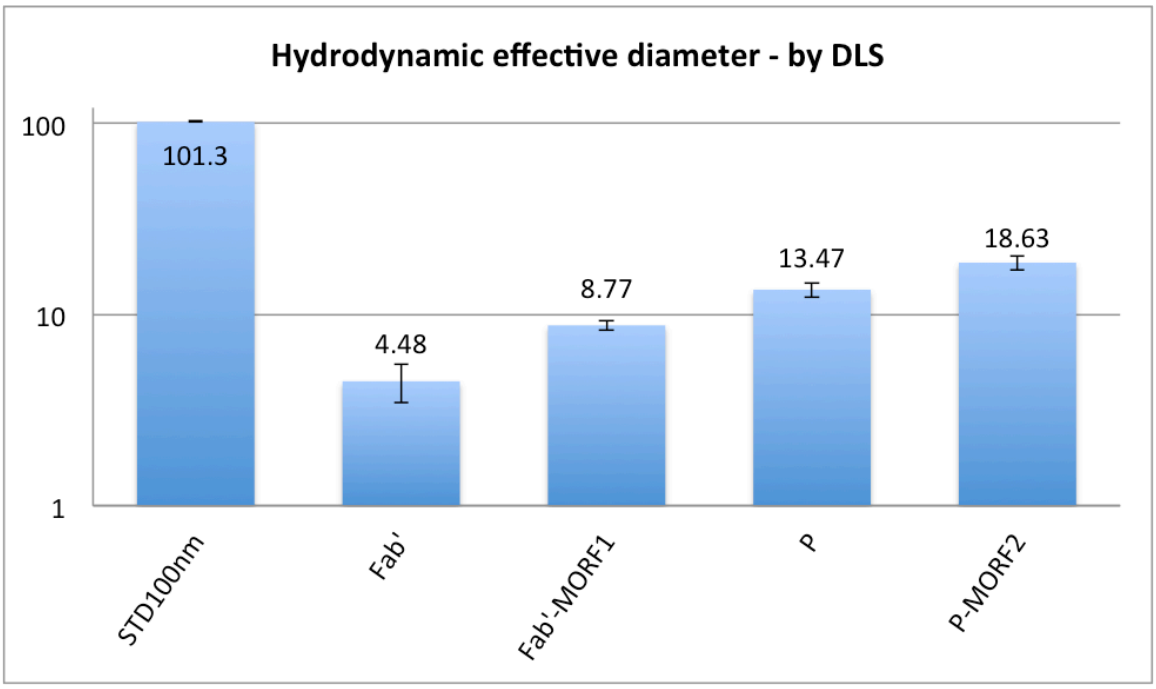

Figure 4.2 Hydrodynamic effective diameters of the two conjugates (Fab'-MORF1 and P-MORF2) and their precursors (Fab' and P) as characterized by DLS. Samples were dissolved in PBS (pH 7.4) and measured at room temperature. Nanosphere™ polystyrene beads with a diameter of 102 ± 3 nm (STD100 nm) were used as the size standard. Data are presented as mean ± SD (n = 3).

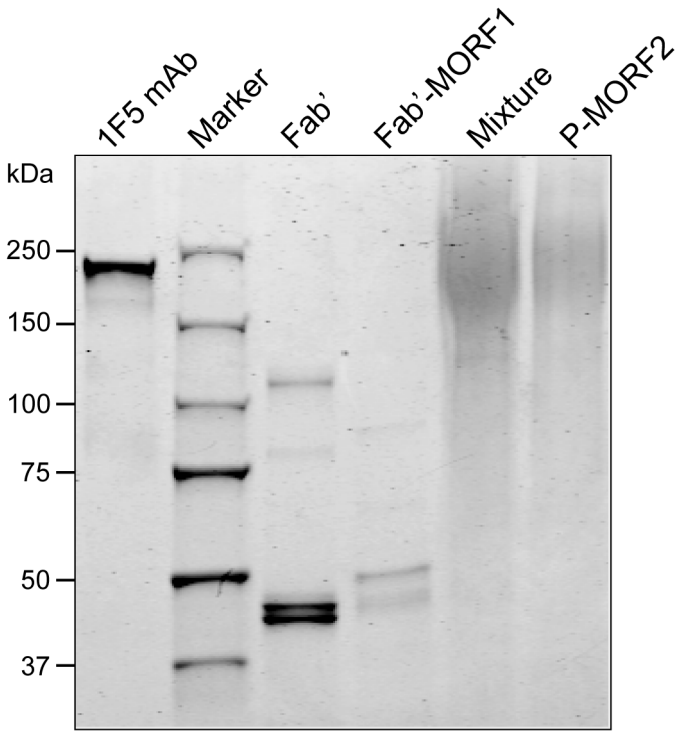

Figure 4.3 SDS-PAGE analysis of the two conjugates and their mixture. Lane 1, 1F5 mAb (1.5 μg). Lane 2, protein ladder. Lane 3, Fab' fragment of 1F5 (1.5 μg). Lane 4, Fab'-MORF1 conjugate (0.3 μg, 5 pmol). Lane 5, mixture of Fab'-MORF1 (5 pmol) and P-MORF2 (5 pmol MORF2 equivalent). Lane 6, P-MORF2 conjugate (5 pmol MORF2 equivalent). Samples were incubated with 1× Laemmli buffer without reducing reagents at 37 °C for 30 min prior to loading; 8–16% polyacrylamide gel. Fab'-MORF1 and P-MORF2 were mixed in PBS (pH 7.4) at room temperature for 1 h. When mixed, the Fab'-MORF1 band completely disappeared from the gel, indicating an efficient binding between the two conjugates.

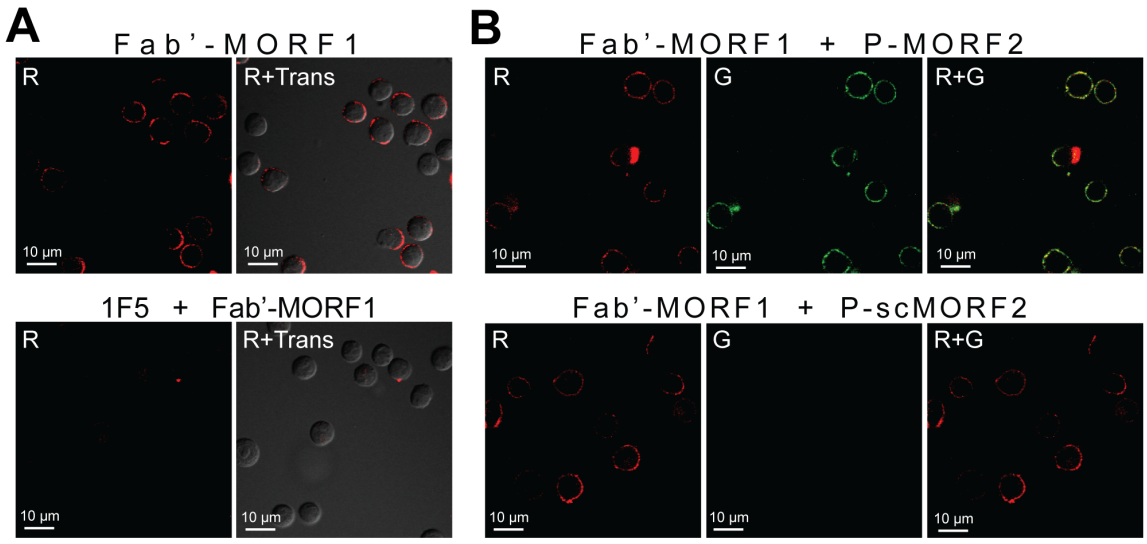

Figure 4.4 Biorecognition of Fab'-MORF1 and P-MORF2 at the surface of Raji B-cells. Fab'-MORF1 was labeled with rhodamine (red) and P-MORF2 with FITC (green). Trans: images under transmitted light, R: red channel, G: green channel. (A) Top panel, Fab'-MORF1 (1 µM) bound to the surfaces of B-cells. Bottom panel, pretreatment with 1F5 mAb (10 µM) followed by Fab'-MORF1 (1 µM). (B) Top panel, consecutive exposure to Fab'-MORF1 (1 µM) and P-MORF2 (1 µM; MORF eqv.). Bottom panel, polymer grafted with scrambled MORF2 (P-scMORF2; 5 µM MORF eqv.) failed to bind to the surfaces of the MORF1-decorated cells; scMORF2: 5'-GTATCCTTATTCCACGTTCATTTGT-3'. Note: P-MORF2 and P-scMORF2 used in this experiment only contained ~5 oligonucleotides per chain.

Figure 4.5 Optimization of tumor pretargeting time lag by PK and biodistribution. (A) The blood radioactivity–time profile of ^{125}I-labeled Fab'-MORF1 in healthy SCID mice (n = 5). The closed circles represent the mean radioactivity, expressed as the percentage of the injected dose per gram of blood (% ID/g). (B) Two-compartment plasma pharmacokinetic (PK) parameters of Fab'-MORF1 in mice. $T_{1/2, \alpha}$, initial half-life; $T_{1/2, \beta}$, terminal half-life; AUC, total area under the blood concentration versus time curve; CL, total body clearance; MRT, mean residence time; Vss, steady-state volume of distribution. (C) Biodistribution of Fab'-MORF1 in healthy SCID mice (no tumor) and SCID mice bearing human B-cell lymphoma xenografts (n = 4 per group). Raji cells were injected from the tail vein of mice 7 days prior to the study. Mice were sacrificed at 1 h or 5 h after i.v. injection of ^{125}I-Fab'-MORF1. (D) Fluorescence molecular tomography (FMT) analysis of lymphoma B-cells dissemination in mice. Four million Raji cells were stained with the DiR dye and injected *via* the tail vein to SCID mice (n = 4). At 24 h after tumor inoculation, organs were harvested for *ex vivo* imaging. L.N., lymph node. (E) Tumor-specific uptake of Fab'-MORF1. Mean radioactivity in each organ of healthy mice (no tumor; n = 4) is defined as the background. Tumor-specific uptake was analyzed by subtracting the background from the radioactivity of corresponding organs of the tumor-bearing mice (n = 4 per group). Negative values are shown as zero. All data are presented as mean ± SD. Statistics were performed with Student's t-test of unpaired samples (* p < 0.05).

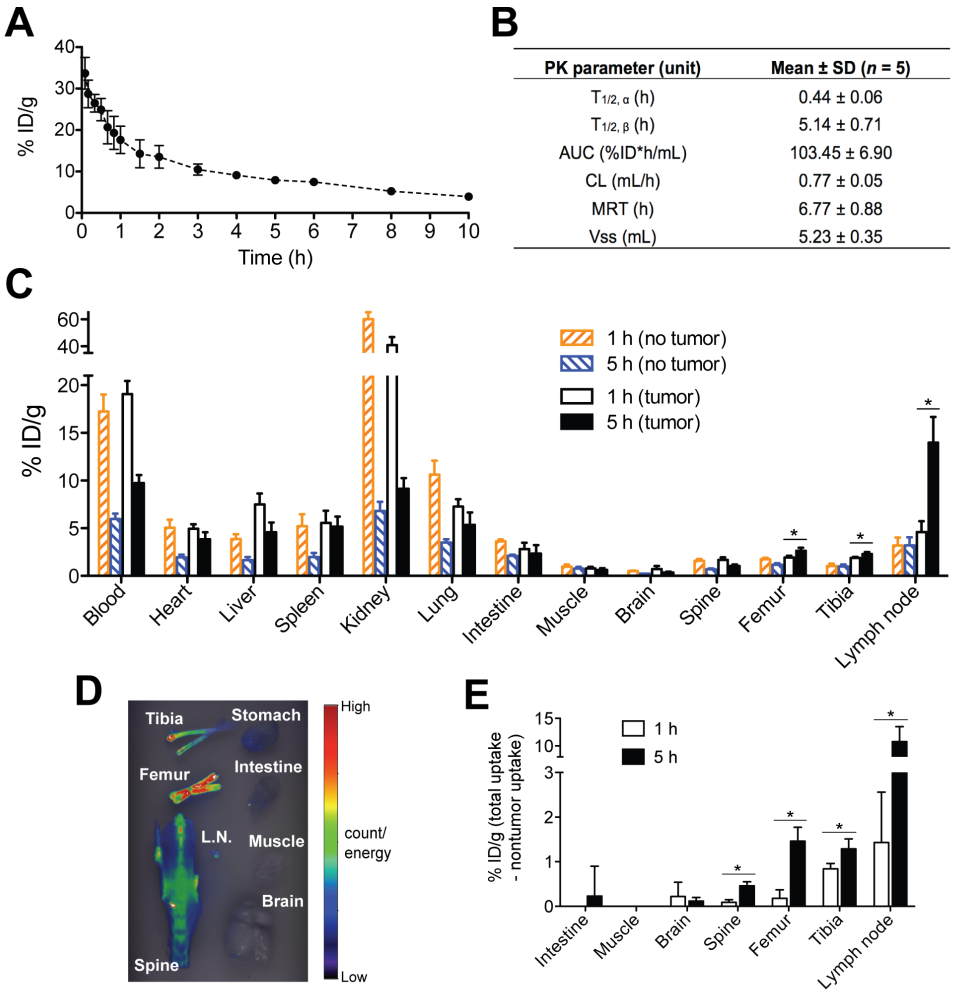
A
% ID/g
Time (h)
B
PK parameter (unit) | Mean ± SD (n = 5)
T1/2, α (h) | 0.44 ± 0.06
T1/2, β (h) | 5.14 ± 0.71
AUC (%ID*h/mL) | 103.45 ± 6.90
CL (mL/h) | 0.77 ± 0.05
MRT (h) | 6.77 ± 0.88
Vss (mL) | 5.23 ± 0.35
C
% ID/g
1 h (no tumor)
5 h (no tumor)
1 h (tumor)
5 h (tumor)
Blood
Heart
Liver
Spleen
Kidney
Lung
Intestine
Muscle
Brain
Spine
Femur
Tibia
Lymph node
D
Tibia
Stomach
Femur
Intestine
L.N.
Muscle
Brain
Spine
High
count/
energy
Low
E
% ID/g (total uptake
- nontumor uptake)
1 h
5 h
Intestine
Muscle
Brain
Spine
Femur
Tibia
Lymph node

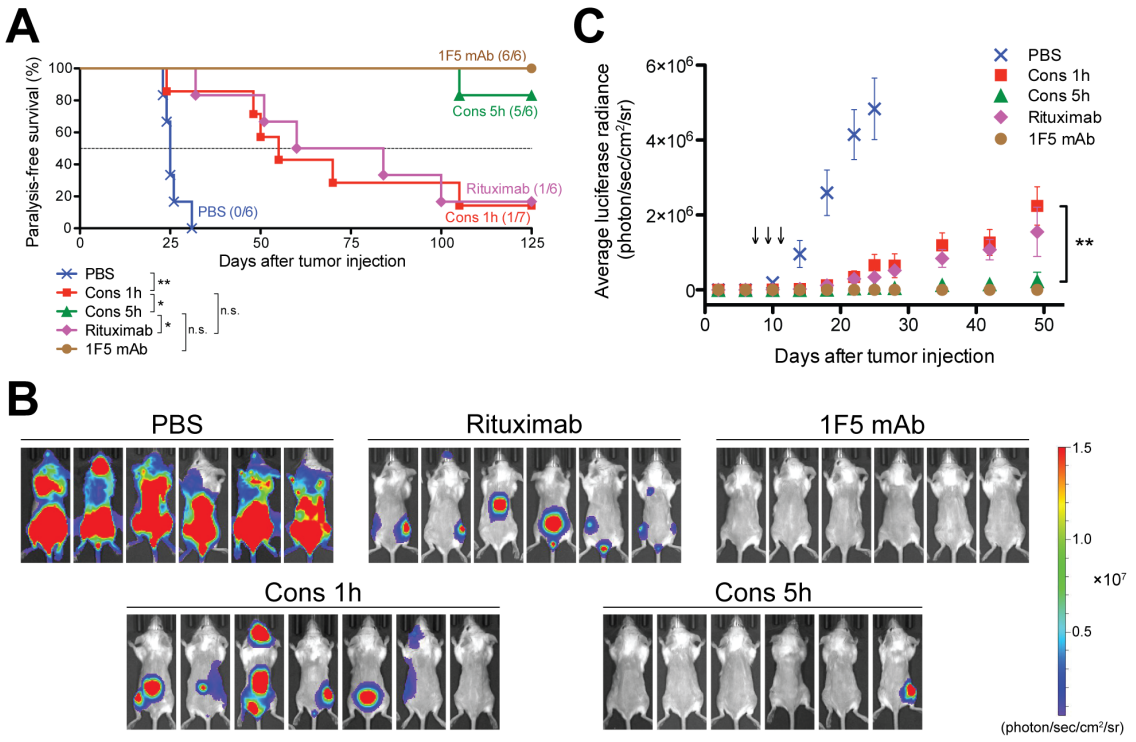

Figure 4.6 *In vivo* therapeutic efficacy against systemic B-cell lymphoma. SCID mice were injected with luciferase-expressing Raji cells (4×10^6) *via* the tail vein on day 0. Three doses of each treatment were administered on days 7, 9, and 11. *PBS*: mice injected with PBS ($n = 6$); *Cons 1h*: consecutive treatment of Fab'-MORF1 and P-MORF2, 1 h interval ($n = 7$); *Cons 5h*: consecutive treatment of Fab'-MORF1 and P-MORF2, 5 h interval ($n = 6$); *Rituximab* ($n = 6$); *1F5 mAb* ($n = 6$). (A) Paralysis-free survival of mice presented in a Kaplan-Meier plot. Numbers of long-term survivors in each group are indicated. Statistics were performed with log-rank test (* $p < 0.05$; ** $p < 0.005$; n.s., no significant difference). (B) *In vivo* bioluminescence images at 25 days after tumor injection. Mice were intraperitoneally injected with 3 mg firefly D-luciferin 15 min prior to imaging. (C) Whole-body bioluminescence intensity of mice. Data are shown as mean ± SEM ($n = 6$ or 7). Statistics were performed by Student's *t*-test (** $p < 0.005$). Black arrow: dose administration.

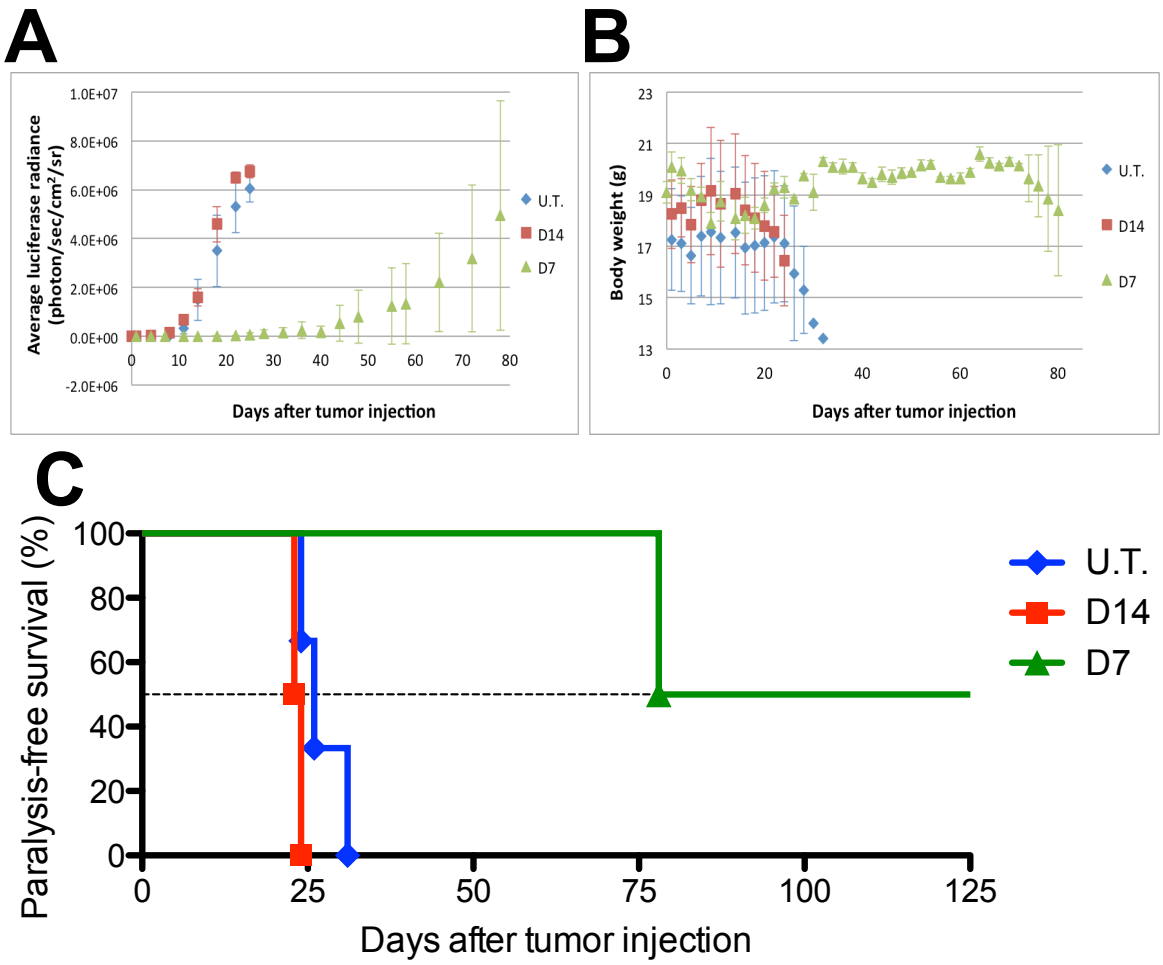

Figure 4.7 Preliminary *in vivo* therapy experiments. SCID mice were injected with luciferase-expressing Raji cells (4×10^6) *via* the tail vein on day 0. Fab'-MORF1 (57.5 μg/20 g; 1 nmol) and P-MORF2 (119 μg/20 g; 5 nmol MORF2) were i.v. administered consecutively, using a 1 h interval. *U.T.*: Untreated mice (n = 3). *D14*: Mice given three doses of treatments on days 14, 16, and 18 (n = 2). *D7*: Mice given three doses of treatments on days 7, 9, and 11 (n = 2). (A) Whole-body bioluminescence intensity of mice. Mice were intraperitoneally injected with 3 mg firefly D-luciferin 15 min prior to imaging. Data are shown as mean ± SD. (B) Body weight charts. Data are shown as mean ± SD. (C) Kaplan-Meier analysis of animal survival. Incidence of hind-limb paralysis or survival of mice was monitored until day 125.

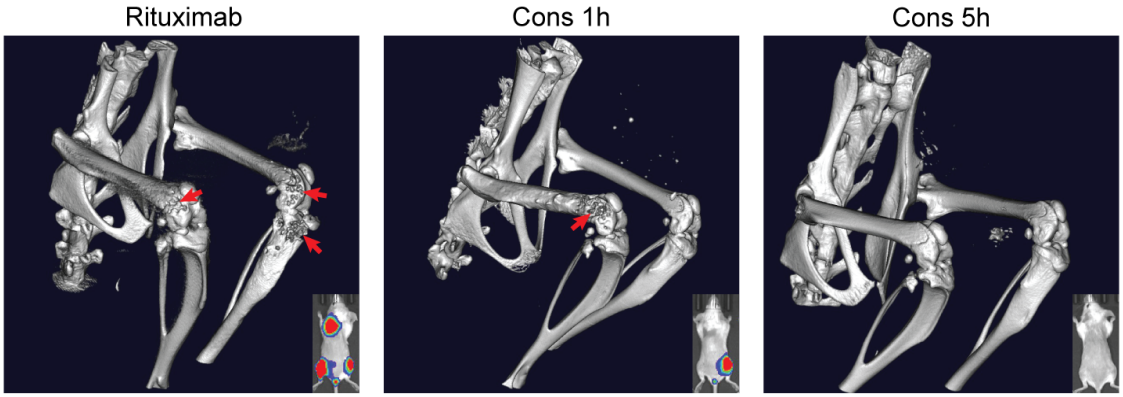

Figure 4.8 Three-dimensional microcomputed tomography (microCT) analysis. Mice were intravenously injected with Raji-luc cells and exposed to different treatments as in Figure 4.6. Imaging was performed on day 70 and focused on the lumbar spine and hind limbs (n = 2 per group). Bone destruction, as a result of lymphoma metastasis, is indicated by the red arrow. Bioluminescence images (day 35) of the same mice are shown in the bottom right corner for comparison.

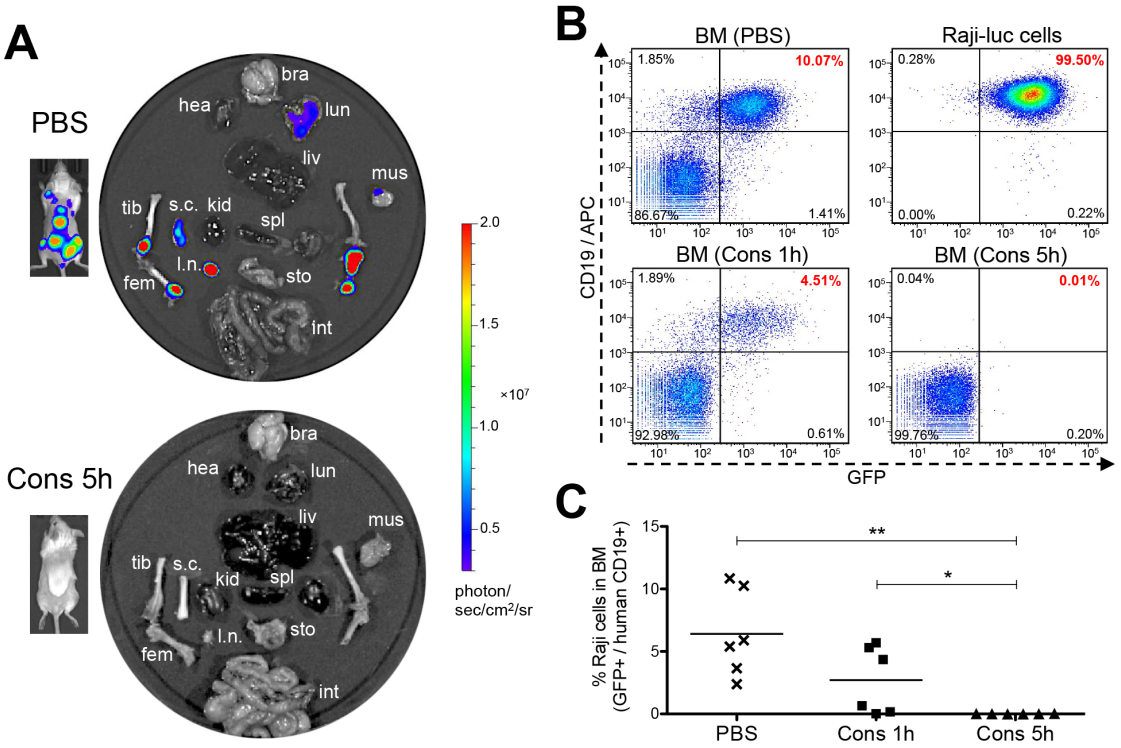

Figure 4.9 Eradication of lymphoma B-cells by drug-free macromolecular therapeutics. Mice i.v. injected with Raji-luc cells were exposed to different treatments as indicated in Figure 4.6. (A) Representative *ex vivo* bioluminescent images of the control mice (PBS) and the mice treated consecutively with Fab'-MORF1 and P-MORF2 using 5 h as an interval (Cons 5h). *In vivo* images of the same mice are shown alongside. *bra*: brain, *hea*: heart, *lun*: lung, *liv*: liver, *spl*: spleen, *kid*: kidney, *s.c.*: spinal cord, *l.n.*: lymph node, *tib*: tibia, *fem*: femur, *mus*: muscle, *sto*: stomach, *int*: intestine. (B) Flow cytometry analysis of residual Raji-luc cells in the bone marrow (BM) of mice. BM cells isolated from mouse femur and Raji-luc cells (with GFP expression) from culture flasks were stained with an APC-labeled mouse anti-human CD19 antibody. (C) Comparison of % lymphoma cells in the bone marrow of control mice (PBS) and the nanomedicine-treated mice (Cons 1h and Cons 5h) as analyzed by flow cytometry. Each data point represents an individual mouse (n = 6 per group); mean % is indicated. Statistics were performed with Student's t-test of unpaired samples (* $p < 0.05$, ** $p < 0.005$).

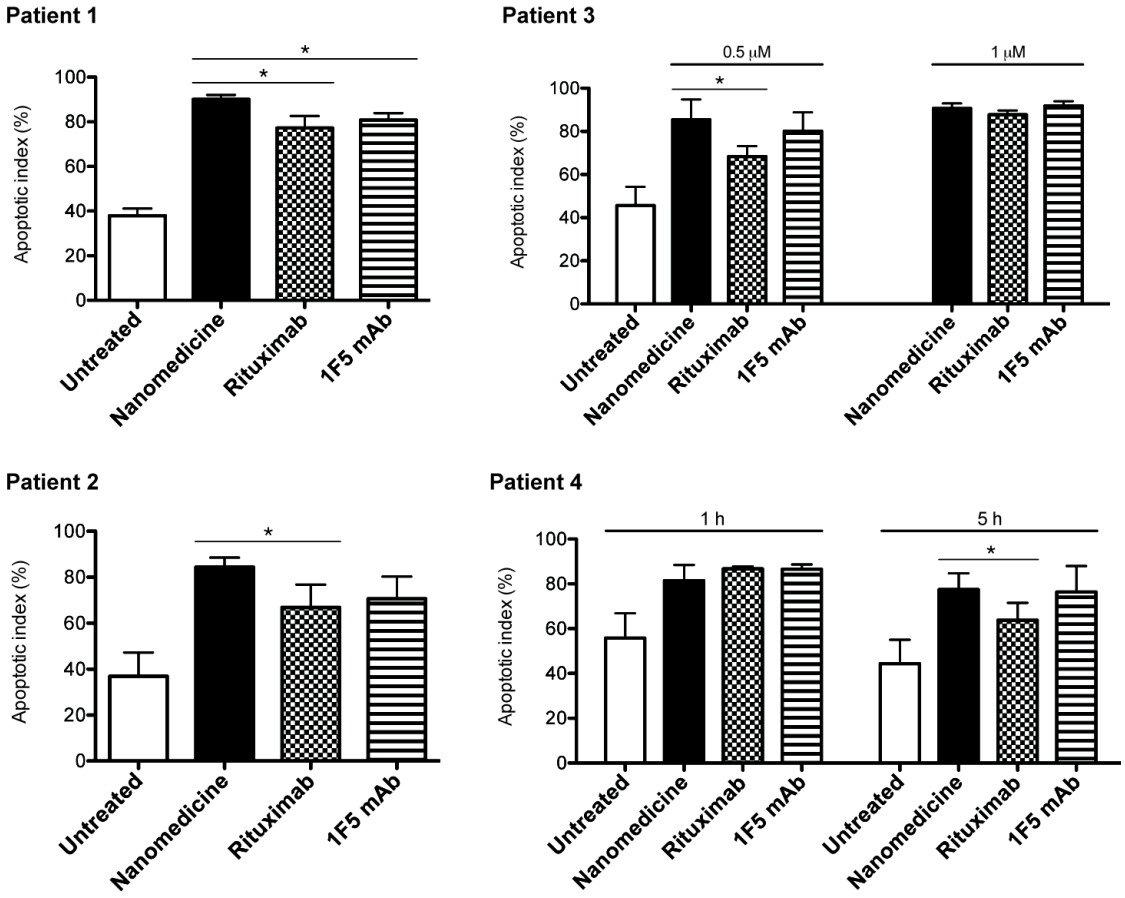

Figure 4.10 Drug-free macromolecular therapeutics induce apoptosis of patient MCL cells. Two samples were from lymph node biopsies (patients 1 and 2) and two from the peripheral blood (patients 3 and 4). Percent apoptotic cells was analyzed by annexin V binding and quantified with flow cytometry. *Nanomedicine*, Fab'-MORF1 followed by P-MORF2; *Rituximab*, rituximab followed by goat anti-mouse secondary Ab; *1F5 mAb*, 1F5 followed by goat anti-mouse secondary Ab. Time interval between treatments was 1 h (unless otherwise indicated). Incubation time was 24 h. Fab' equivalent concentrations of treatments were 0.5 μM (for patients 1, 2 and 3) and 1 μM (for patients 3 and 4). Data are presented as mean ± SD (n = 2 or 3, independent replicates). Statistics were performed by Student's t-test (* $p < 0.05$). All treatment groups had significantly higher apoptotic indices when compared to the untreated cells.

CHAPTER 5

DRUG-FREE MACROMOLECULAR THERAPEUTICS INDUCE APOPTOSIS OF PATIENT CHRONIC LYMPHOCYTIC LEUKEMIA CELLS[1]

A new drug-free nanotherapeutic approach for B-cell malignancies was developed. Exposure of B-cells to an anti-CD20 Fab'-morpholino oligonucleotide1 (MORF1) conjugate decorated the cell surface with MORF1; further exposure of the decorated cells to multivalent polymer-oligonucleotide2 conjugates (P-MORF2) resulted in CD20 clustering at the cell surface with induction of apoptosis. In this chapter, we evaluate this concept in primary chronic lymphocytic leukemia (CLL) cells isolated from 10 patients. Apoptosis and cytotoxicity were observed in eight samples, including two samples with the 17p13 deletion, which suggested a p53-independent mechanism of apoptosis induction. When compared to an anti-CD20 monoclonal antibody (mAb), the nanotherapeutic showed significantly more potent apoptosis-inducing activity and cytotoxicity. This was due to the multivalency effect (8 binding sites per polymer chain) of our design in comparison to the divalent mAb. In summary, we have developed a novel and potent therapeutic system against CLL and other B-cell malignancies with

[1]With kind permission from Springer Science+Business Media this chapter is adapted from the following publication: Drug-free macromolecular therapeutics induce apoptosis of patient chronic lymphocytic leukemia cells. *Drug Deliv Transl Res*. 2014; 4(5–6): 389–394.

significant advantages over conventional chemo-immunotherapy.

5.1 Background

B-cell malignancies are prevalent cancers worldwide.[1] Crosslinking of CD20 receptors at the surface of B-cells initiates apoptosis.[2–4] Based on this mechanism, we designed a therapeutic system composed of two hybrid macromolecules: (1) a conjugate of the Fab' fragment of anti-CD20 1F5 monoclonal antibody (mAb) with a morpholino oligonucleotide MORF1; (2) a linear *N*-(2-hydroxypropyl)methacrylamide (HPMA) copolymer grafted with multiple copies of the complementary oligonucleotide MORF2 (P-MORF2).[5] Exposure of a B-cell non-Hodgkin lymphoma line (Raji) to the anti-CD20 **Fab'-MORF1** conjugate decorated the cell surface with MORF1. Further exposure of the decorated cells to **P-MORF2** resulted in MORF1/MORF2 hybridization, which initiated CD20 crosslinking and triggered apoptosis *in vitro* and *in vivo*.[5] In this design, the morpholino oligonucleotide pair serves as a physical crosslinker to cluster CD20 antigens at the cell surface. Extracellular hybridization of MORF1/MORF2 translates into innate biological responses, *i.e.*, apoptosis. This "drug-free macromolecular therapeutic" involves no cytotoxic drug, and the individual parts of the system do not have apoptosis-inducing activity. The two nanoscale conjugates (Fab'-MORF1 and P-MORF2) can be administered consecutively (for pretargeting approaches) or as a premixture.

Here, we evaluated the efficacy of drug-free macromolecular therapeutics on primary chronic lymphocytic leukemia (CLL) cells isolated from patients. We hypothesized that this CD20 receptor crosslinking system is cytotoxic to CLL cells and could constitute a new nanomedicine for CLL and other B-cell malignancies.

5.2 Materials and Methods

5.2.1 Patient Samples and Treatments

Peripheral blood mononuclear cells were isolated from 10 untreated CLL patients (clinical details summarized in Table 5.1). All samples expressed dim CD20, a typical phenotype of CLL. Specimens were collected after informed consent under a protocol approved by the University of Utah Institutional Review Board. Cells were suspended in RPMI-1640 medium (Sigma, St. Louis, MO) supplemented with 10% fetal bovine serum (Hyclone, Logan, UT). Incubation was carried out at 37 °C in a humidified atmosphere with 5% CO2. Cells were treated with Fab'-MORF1 and P-MORF2 (at equimolar MORF1/MORF2 concentrations), either consecutively (1 h interval) or as a premixture (1 h, 37 °C). Fab'-MORF1 and P-MORF2 were prepared as previously described.[5]

5.2.2 Cytotoxicity and Apoptosis Assays

In all experiments, an anti-CD20 mAb (1F5)[6] hypercrosslinked with a goat anti-mouse (GAM) secondary antibody (KPL, Gaithersburg, MD) was used as a positive control (molar ratio 1F5:GAM = 2:1). Untreated cells were used as negative controls. All experiments were conducted in duplicate or triplicate wells.

5.2.2.1 Cytotoxicity

Viability of cells was determined by Trypan blue staining at the indicated time points. Alternatively, cells were stained with propidium idodie (PI) and the percentage of PI-positive cells was quantified by flow cytometry.

5.2.2.2 Annexin V Binding

Two hundred thousand cells were suspended in 0.4 mL medium for different treatments. Cells were harvested at the indicated time intervals, washed twice with PBS prior to staining by propidium iodide and FITC-conjugated annexin V. Staining was performed following the RAPID™ protocol provided by the manufacturer (Oncogene Research Products, Boston, MA).

5.2.2.3 Caspase-3 Activity

Two hundred thousand cells were suspended in 0.4 mL medium for different treatments. Cells were harvested at the indicated time intervals and washed twice with PBS. A PhiPhiLux® kit was used to assay caspase-3 activity using the manufacturer's protocol (OncoImmunin, Gaithersburg, MD).

5.2.2.4 TUNEL Assay

One million cells were suspended in 0.5 mL medium for different treatments. At the indicated time points, cells were fixed with 1% paraformaldehyde in PBS (1 h, 4 °C) and permeabilized in 70% ethanol overnight at -20 °C. An Apo Direct TUNEL kit was used to assay apoptosis using the manufacturer's protocol (Phoenix Flow Systems, San Diego, CA).

5.2.3 Cell Cycle Analysis

Cells were washed twice with PBS after the indicated treatments and permeabilized in 70% ethanol overnight at -20 °C. Cells were stained with an excess of

PI in PBS, and DNA content was determined by flow cytometry.

5.2.4 Statistical Analysis

All experiments were at least duplicated. Data are presented as mean ± standard deviation (SD). Differences were considered significant for p values < 0.05 using the Student's *t*-test.

5.3 Results and Discussion

To evaluate the potential of drug-free macromolecular therapeutics for the treatment of chronic lymphocytic leukemia (CLL), cells from 10 patients were obtained (Table 5.1). As shown in Table 5.1, these patients fell into different prognostic categories, including 2 with the 17p13 deletion.

The isolated cells were treated with conjugates Fab'-MORF1 (58.5 kDa; equimolar MORF1/Fab') and P-MORF2 (P: 136 kDa; 8 MORF2 per chain), either consecutively or as a premixture. The experimental conditions and results of apoptosis and cytotoxicity assays are summarized in Tables 5.2 and 5.3, respectively. Results showed that both treatment regimens (consecutive and premixed) effectively induced apoptosis of CLL cells. Data from 8 patient samples (P1, P2, P4, P6-P10) showed significantly higher apoptotic and/or cytotoxic indices in the nanomedicine groups when compared to the nontreated cells. A trend of apoptosis induction was also observed in P3 and P5; however, the changes with the latter samples were not statistically significant. Interestingly, the treatment showed activity against the two samples with the 17p13 deletion (P7 and P8). Deletions of 17p are associated with the loss of one allele of *P53*

and portend a worse prognosis.[7] Our results suggest that apoptosis induction by drug-free macromolecular therapeutics is p53-independent. It has been reported that the CD20-crosslinking-mediated B-cell death is a distinct pathway that can bypass mitochondria and caspase activation, which could be an advantage in the treatment of chemoresistant malignancies.[8] This indicates that what we propose has significant advantages over conventional chemo- and radiotherapy approaches, especially for high-risk patients with the 17p deletion whose disease is particularly difficult to treat. More mechanistic studies are needed to further elucidate the pathway(s) leading to apoptosis induction by drug-free macromolecular therapeutics.

In our experiments, an anti-CD20 mAb hypercrosslinked with a goat anti-mouse secondary Ab was used as a positive control in order to reproduce the function of immune effector cells.[9] This control partly reproduces the therapeutic efficacy of anti-CD20 mAbs that are used in the clinic (*e.g.*, rituximab). Our drug-free macromolecular approach is more effective at apoptosis induction in CLL cells than the mAb control. As shown in Tables 5.2 and 5.3, five patient samples (P1, P2, P6, P7 and P9) showed significantly higher apoptotic and/or cytotoxic indices in the nanomedicine group when compared to the positive control (mAb + 2° Ab). This was likely due to multivalency of the P-MORF2 conjugate (8 binding sites per chain) in comparison to the divalent mAb. Our lab[10,11] and others[12, 13] have previously shown that the multivalency of anti-CD20 constructs can increase binding affinity and apoptosis-inducing efficiency by several fold, when compared to their monovalent or divalent counterparts. We have also reported that, in addition to valence, the polymer length (*i.e.*, MW) had a positive influence on CD20 clustering and apoptosis.[4] Therefore, it is possible to further improve the efficacy of this

design by using a P-MORF2 conjugate with a higher valence and/or a larger polymer backbone. For instance, multiblock backbone degradable HPMA copolymers can be synthesized.[14–16] This approach can produce P-MORF2 with substantially increased MW and valence.

We evaluated apoptosis and cytotoxicity from multiple aspects: plasma membrane rupture (Figures 5.1A–5.1E), caspase-3 activation (Figure 5.1F), and genomic DNA fragmentation (Figures 5.1G and 5.1H). Results consistently showed that the designed nanomedicine was effective at inducing apoptosis in CLL cells. In contrast, single-component treatments with either Fab'-MORF1 or P-MORF2 alone failed to induce apoptosis (Figure 5.1E), confirming the necessity to crosslink CD20 in order to trigger apoptosis. The effects of the nanomedicine were dose- (Figure 5.1B) and time-dependent (Figures 5.1C, 5.1D and 5.1G). In some cases, the mAb does not demonstrate apoptosis-inducing activity, *e.g.*, in P1, P3, P6 and P8 (as shown in Table 5.2 and Figure 5.1B), whereas the nanomedicine is effective. This observation suggests a higher potency of drug-free macromolecular therapeutics when compared to mAb treatment.

The field of CLL therapy has entered a period of significant change with the recent approval of two agents, ibrutinib and idelasilib, targeting the Bruton tyrosine kinase and phosphatidylinositide 3-kinase-δ, respectively.[17] Mechanistically, both targets are related to the B-cell receptor signaling pathway. The drug-free nanotherapeutic approach constitutes yet another novel therapeutic approach. It induces apoptosis in the malignant cells without the need for cytotoxic compounds or immune system activation. It will be interesting to determine whether this strategy synergizes with the new, targeted agents. Furthermore, the proposed two-step (consecutive) approach allows the use of

pretargeting[18,19] For example, the timing of administration of P-MORF2 can be optimized in individual patients based on pharmacokinetics and biodistribution of Fab'-MORF1, in order to enable more efficient treatment while limiting potential side effects associated with off-target binding. We have currently validated this concept in mice bearing B-cell lymphoma xenografts (see *Chapter 4*). With the use of an optimized time lag, a two-step pretargeting approach was employed to achieve favorable tumor-to-tissue accumulation, which resulted in significantly improved *in vivo* anticancer efficacy.

In summary, we have developed a novel and potent drug-free nanotherapeutic approach for the treatment of CLL and other B-cell malignancies. This approach has significant advantages over current cytotoxic therapies and immunotherapies. The clinical development of our strategy will likely contribute to the ongoing revolution in the treatment of these diseases.

5.4 References

1. R. Siegel, J. Ma, Z. Zou and A. Jemal, Cancer statistics, 2014, *CA Cancer J. Clin.*, 2014, **64**, 9–29.

2. J. K. Hofmeister, D. Cooney and K. M. Coggeshall, Clustered CD20 induced apoptosis: src-family kinase, the proximal regulator of tyrosine phosphorylation, calcium influx, and caspase 3-dependent apoptosis, *Blood Cells. Mol. Dis.*, 2000, **26**, 133–143.

3. N. Zhang, L. A. Khawli, P. Hu and A. L. Epstein, Generation of rituximab polymer may cause hyper-cross-linking–induced apoptosis in non-Hodgkin's lymphomas, *Clin. Cancer Res*., 2005, **11**, 5971–5980.

4. T.-W. Chu, J. Yang and J. Kopeček, Anti-CD20 multivalent HPMA copolymer–Fab' conjugates for the direct induction of apoptosis, *Biomaterials*, 2012, **33**, 7174–7181.

5. T.-W. Chu, J. Yang, R. Zhang, M. Sima and J. Kopeček, Cell surface self-assembly of hybrid nanoconjugates *via* oligonucleotide hybridization induces apoptosis, *ACS Nano*, 2014, **8**, 719–730.

6. O. W. Press, *et al.*, Monoclonal antibody 1F5 (anti-CD20) serotherapy of human B cell lymphomas, *Blood*, 1987, **69**, 584–591.

7. J. C. Byrd, J. J. Jones, J. A. Woyach, A. J. Johnson and J. M. Flynn, Entering the era of targeted therapy for chronic lymphocytic leukemia: impact on the practicing clinician, *J. Clin. Oncol*., 2014, **32**, 3039–3047.

8. L. E. van der Kolk, *et al.*, CD20-induced B cell death can bypass mitochondria and caspase activation, *Leukemia*, 2002, **16**, 1735–1744.

9. D. Shan, J. A. Ledbetter and O. W. Press, Apoptosis of malignant human B cells by ligation of CD20 with monoclonal antibodies, *Blood*, 1998, **91**, 1644–1652.

10. R. N. Johnson, P. Kopečková and J. Kopeček, Synthesis and evaluation of multivalent branched HPMA copolymer–Fab' conjugates targeted to the B-cell antigen CD20, *Bioconjug. Chem*., 2009, **20**, 129–137.

11. R. N. Johnson, P. Kopečková and J. Kopeček, Biological activity of anti-CD20 multivalent HPMA copolymer–Fab' conjugates. *Biomacromolecules*, 2012, **13**, 727–735.

12. S. R. Aluri, *et al*., A hybrid protein-polymer nanoworm potentiates apoptosis better than a monoclonal antibody, *ACS Nano*, 2014, **8**, 2064–2076.

13. Z. Zhang, *et al.*, DNA-scaffolded multivalent ligands to modulate cell function, *Chembiochem*, 2014, **15**, 1268–1273.

14. H. Pan, J. Yang, P. Kopečková and J. Kopeček, Backbone degradable multiblock *N*-(2-hydroxypropyl)methacrylamide copolymer conjugates *via* reversible addition-fragmentation chain transfer polymerization and thiol-ene coupling reaction, *Biomacromolecules*, 2011, **12**, 247–252.

15. J. Yang, K. Luo, H. Pan, P. Kopečková and J. Kopeček, Synthesis of biodegradable multiblock copolymers by click coupling of RAFT-generated heterotelechelic polyHPMA conjugates, *React. Funct. Polym.*, 2011, **71**, 294–302.

16. R. Zhang, J. Yang, M. Sima, Y. Zhou and J. Kopeček, Sequential combination therapy of ovarian cancer with degradable *N*-(2-hydroxypropyl)methacrylamide copolymer paclitaxel and gemcitabine conjugates, *Proc. Natl. Acad. Sci. U.S.A*., 2014, **111**, 12181–12186.

17. A. V. Danilov, Targeted therapy in chronic lymphocytic leukemia: past, present, and future, *Clin. Ther*., 2013, **35**, 1258−1270.

18. D. A. Goodwin and C. F. Meares, Advances in pretargeting biotechnology, *Biotechnol. Adv.*, 2001, **19**, 435–450.

19. J. Gunn, S. I. Park, O. Veiseh, O. W. Press and M. A. Zhang, Pretargeted nanoparticle system for tumor cell labeling, *Mol. Biosyst.*, 2011, **7**, 742–748.

Figure 5.1 Drug-free macromolecular therapeutics induce apoptosis of patient CLL cells. (A) Representative flow cytometric analysis of cells exposed to different treatments and stained by propidium iodide (PI) and FITC-labeled annexin V. *Nontreated*: cells in culture medium; *Consecutive*: Fab'-MORF1 (0.5 μM) followed (1 h later) by P-MORF2 (0.5 μM; MORF2-eqv.). Incubation time was 20 h. Data from patient sample #2. (B) Dose-dependent apoptosis induction. Percentage of early apoptotic cells (annexin V^+/PI^-) was quantified by flow cytometry. *mAb + 2° Ab*: 1F5 mAb followed (1 h later) by goat anti-mouse secondary Ab; *Consecutive*: Fab'-MORF1 followed (1 h later) by P-MORF2; Premixed: premixture of Fab'-MORF1 and P-MORF2. Incubation time was 30 h. Data from patient sample #8. (C) Time-dependent apoptosis induction. Fab'-equivalent concentration was 0.5 μM (applied to D-H). Data from patient sample #6. (D) Time-dependent cytotoxicity as determined by PI binding. Data from patient sample #6. (E) Cell viability as determined by Trypan blue staining. Incubation time was 20 h. *Fab'-MORF1*: single-component control at 0.5 μM; *P-MORF2*: single-component control at 0.5 μM (MORF2-eqv.). Data from patient sample #1. (F) Representative flow cytometric analysis of cells exposed to different treatments and stained by FITC-labeled anti-active caspase-3 Ab. Incubation time was 6 h. Data from patient sample #10. (G) Apoptosis as analyzed by TUNEL assay. FITC-labeled anti-bromodeoxyuridine (BrdU) Ab stains apoptotic cells. Data from patient sample #6. (H) Cell cycle analysis. Cells were permeabilized and stained by PI to measure DNA content. SubG1 phase represents apoptotic cells. Incubation time was 30 h. Data from patient sample #7. In B-E and G, data are presented as mean + SD (n = 2 or 3). Statistics in E and G, unless otherwise indicated, were performed by comparing each group with nontreated (** $p < 0.005$; * $p < 0.05$; n.s., no significant difference; Student's t-test).

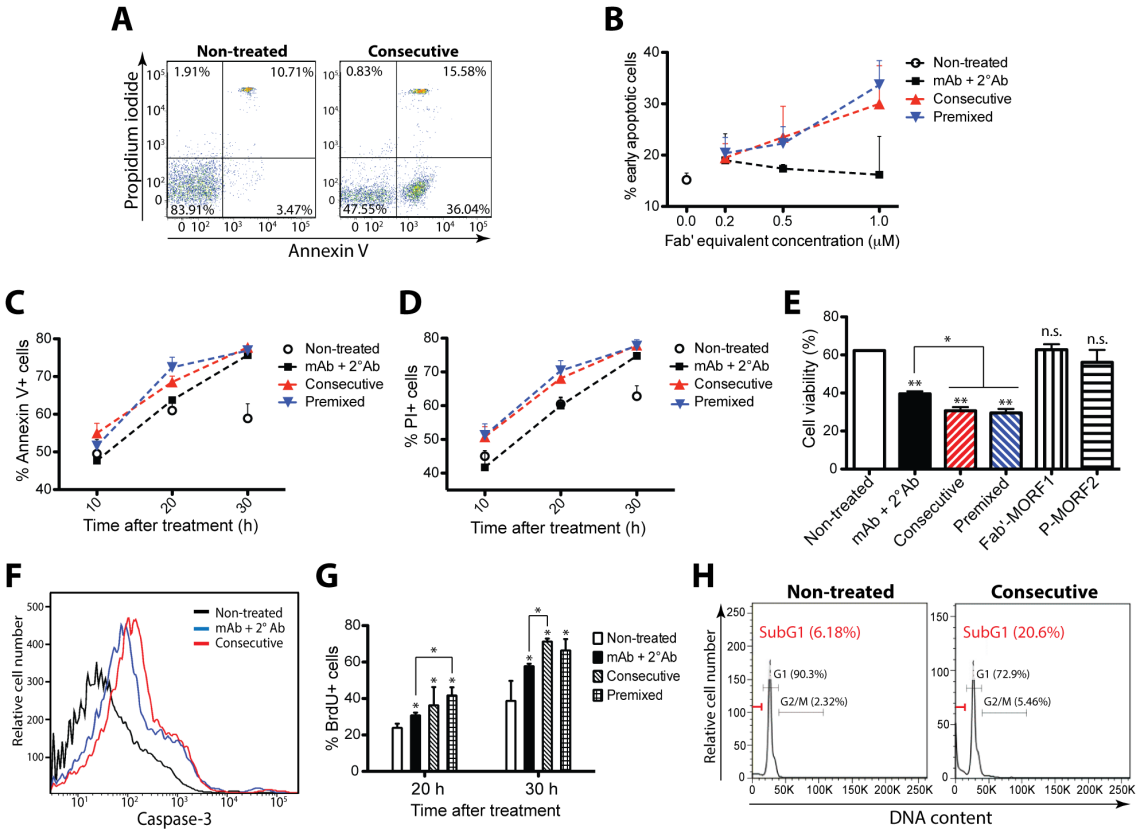
A
Non-treated
Consecutive
Propidium iodide
Annexin V
1.91%
10.71%
83.91%
3.47%
0.83%
15.58%
47.55%
36.04%
B
% early apoptotic cells
Fab' equivalent concentration (μM)
Non-treated
mAb + 2°Ab
Consecutive
Premixed
C
% Annexin V+ cells
Time after treatment (h)
D
% PI+ cells
Time after treatment (h)
E
Cell viability (%)
n.s.
Non-treated
mAb + 2°Ab
Consecutive
Premixed
Fab'-MORF1
P-MORF2
F
Relative cell number
Caspase-3
G
% BrdU+ cells
20 h
30 h
Time after treatment
H
Non-treated
Consecutive
SubG1 (6.18%)
G1 (90.3%)
G2/M (2.32%)
SubG1 (20.6%)
G1 (72.9%)
G2/M (5.46%)
DNA content

Table 5.1 Clinical characteristics of CLL patients.

Patient #	Age (y)	[a]Sex	Rai Stage	[b]IgV_H Mutation	CD38	ZAP70	FISH Cytogenetics
P1	83	F	I	n/a	neg	n/a	n/a
P2	76	M	I	M	neg	n/a	13q−
P3	52	M	I	U	neg	pos	normal
P4	80	F	II	n/a	pos	n/a	ts12
P5	67	M	I	n/a	neg	pos	13q−
P6	59	M	II	U	neg	pos	13q−
P7	72	M	I	U	n/a	pos	17p−/11q−/ts12
P8	60	M	I	U	neg	pos	17p−/13q−
P9	49	F	0	n/a	pos	neg	13q−
P10	72	F	0	U	neg	int	13q−

IgV_H, immunoglobulin heavy variable chain; ZAP70, ζ-chain-associated protein kinase 70; FISH, fluorescence *in situ* hybridization; n/a, not available; neg, negative; pos, positive; int, intermediate; ts12, trisomy 12.

[a]M, male; F, female.

[b]U, unmutated; M, mutated.

Table 5.2 Experimental conditions and results of apoptosis assays.

Patient #	Treatment Time	Dose	Assay	Apoptotic Index (%)			
				Non-treated	**mAb + 2° Ab**	**Cons-ecutive**	**Pre-mixed**
P1	20 h	0.5 μM	Annexin V	30 ± 0.6	27 ± 2.1	**48 ± 9.6**	‡**49 ± 3.3**
P2	20 h	0.5 μM	Annexin V	27 ± 1.4	37 ± 4.4	‡**52 ± 0.8**	‡**58 ± 0.6**
P3	20 h	0.5 μM	Annexin V	28 ± 4.6	25 ± 3.6	**34 ± 6.8**	**32 ± 7.9**
P4	20 h	0.5 μM	Annexin V	34 ± 4.6	†54 ± 5.4	†**54 ± 5.9**	†**59 ± 2.8**
P5	20 h	0.5 μM 1 μM	Annexin V	25 ± 8.9	40 ± 3.0 39 ± 0.2	**38 ± 0.1** **43 ± 1.5**	**38 ± 0.1** **40 ± 2.3**
P6	20 h 30 h	0.5 μM	Annexin V	61 ± 2.8 59 ± 3.9	64 ± 0.3 †76 ± 0.3	‡**69 ± 1.6** ‡**78 ± 0.8**	‡**72 ± 2.6** †**77 ± 0.7**
	20 h 30 h	0.5 μM	TUNEL	24 ± 2.3 39 ± 11.0	†31 ± 1.5 †58 ± 1.3	†**36 ± 9.9** ‡**71 ± 1.6**	‡**42 ± 4.5** †**66 ± 6.2**
P7	30 h	0.5 μM	Annexin V	41 ± 1.7	†52 ± 1.4	‡**66 ± 0.3**	‡**62 ± 1.1**
P8	30 h	0.5 μM 1 μM	Annexin V	15 ± 1.4	17 ± 0.8 16 ± 7.5	**23 ± 6.0** †**30 ± 7.4**	**22 ± 3.3** †**34 ± 4.7**
P9	48 h	0.5 μM	Annexin V	46 ± 7.2	†77 ± 1.0	‡**82 ± 0.1**	†**78 ± 2.8**
P10	6 h	0.5 μM	Caspase-3	10 ± 0.1	17 ± 4.2	†**23 ± 3.5**	†**21 ± 4.6**

†Significantly higher than nontreated ($p < 0.05$; Student's *t*-test).

‡Significantly higher than nontreated and mAb + 2° Ab ($p < 0.05$; Student's *t*-test).

Table 5.3 Experimental conditions and results of cytotoxicity assays.

Patient #	Treatment Time	Dose	Assay	Cytotoxicity Index (%)			
				Non-treated	**mAb + 2° Ab**	**Cons-ecutive**	**Pre-mixed**
P1	20 h	0.5 μM	Trypan Blue	38 ± 0.3	†60 ± 1.3	‡**69 ± 1.9**	‡**71 ± 2.1**
P2	20 h	0.5 μM	Trypan Blue	59 ± 5.3	†88 ± 5.0	†**82 ± 5.4**	†**91 ± 0.9**
P4	20 h	0.5 μM	Trypan Blue	52 ± 6.0	63 ± 4.6	**76 ± 7.1**	†**76 ± 3.9**
			PI	49 ± 1.1	53 ± 6.0	†**60 ± 2.8**	†**61 ± 1.3**
P6	20 h	0.5 μM	PI	60 ± 1.8	60 ± 2.5	‡**68 ± 0.6**	‡**70 ± 3.0**
	30 h			63 ± 3.1	†75 ± 0.3	‡**78 ± 0.4**	†**78 ± 1.8**
P7	30 h	0.5 μM	PI	22 ± 6.8	43 ± 2.5	‡**52 ± 1.1**	†**45 ± 0.7**
P9	48 h	0.5 μM	PI	44 ± 0.2	†67 ± 1.4	†**69 ± 0.3**	†**66 ± 0.1**

†Significantly higher than nontreated ($p < 0.05$; Student's *t*-test).

‡Significantly higher than nontreated and mAb + 2° Ab ($p < 0.05$; Student's *t*-test).

CHAPTER 6

CONCLUSIONS AND BEYOND[1]

Adverse side effects and resistance remain major clinical obstacles for cancer chemo-immunotherapy. This dissertation proposes a nanomedicine approach that is "drug-free" and "immune-independent" to tackle these problems simultaneously. This approach utilizes multivalent cell surface receptor crosslinking constructs to trigger apoptosis of cancers specifically and effectively. The designs of two therapeutic platforms have been shown. In the first design, multiple targeting moieties (Fab' fragments) are tethered to a synthetic polymer for direct apoptosis induction (*Chapter 2*). In the second design, the treatment is two-step. First, cancer cells are marked for death by a pretargeting dose; then, the therapeutically active, multivalent effector is administered (*Chapters 3–5*). This two-step strategy allows optimization of the therapy for individual subjects. We have shown in a mouse model that the optimized therapy is more efficacious than rituximab, a clinically used immunotherapy drug for B-cell lymphomas (*Chapter 4*). This is striking evidence that the anticancer efficacy of receptor-crosslinking-mediated apoptosis alone may be superior to immunotherapy. We have also demonstrated the potential application on other diseases such as leukemias (*Chapter 5*).

---

[1]This chapter is adapted from the following publication: T.-W. Chu and J. Kopeček. Drug-free macromolecular therapeutics – a new paradigm in polymeric nanomedicines. *Biomater Sci.* 2015; 3(7): 908–922. Adapted by permission of The Royal Society of Chemistry.

One of the most important features of drug-free macromolecular therapeutics is the lack of low-MW cytotoxic compounds and, thus, the absence of nonspecific toxicities. The apoptosis induction is highly specific against the targeted cells, which will likely result in a better adverse effects profile when compared to conventional chemo- and radiotherapies. The mechanism of receptor crosslinking is unique. For instance, the CD20-clustering-mediated B-cell death has been identified as a distinct pathway that can bypass mitochondria and caspase activation, which offers the opportunity to treat chemoresistant malignancies.[1] Besides the drug-free feature, other favorable aspects of our design are: (1) the immune-independent feature addresses the concern of mAbs nonresponiveness or resistance; (2) multivalency of the polymer conjugates has potential to improve therapeutic performance; (3) as mentioned above, the proposed two-step treatment is suitable for pretargeting.

Distinct from mAb-based immunotherapy, drug-free macromolecular therapeutics directly induce apoptosis in diseased cells without the need for immune activation. Successful treatment with mAbs requires FcR-expressing immune effector cells (macrophages, neutrophils, natural killer cells, *etc.*) to recognize the Fc region of ligated antibodies and trigger immune responses such as ADCC or CDC.[2,3] However, a common clinical failure of immunotherapy is the inactivation of these effector mechanisms.[4,5] For instance, many rituximab nonresponders harbor polymorphism in the IgG FcR gene, which leads to the inability of effector cells to hypercrosslink mAbs that are bound to the surfaces of B-cells.[4] In the drug-free design, we used synthetic effectors to reproduce and enhance the function of immune effector cells. High-fidelity biorecognition pairs are introduced externally to replace the Fc–FcR binding. This approach may benefit patients

who do not respond to immunotherapies, which constitute about half of all B-NHLs.[6] In addition, the Fab' conjugates (without Fc) are used for pretargeting. This is advantageous because various reported mechanisms attributed to the mAb resistance are directly or partly mediated by the Fc–FcR recognition, for example, CD20 downregulation,[7,8] internalization,[9,10] and "trogocytosis" (shaving of receptors from cell surfaces by macrophages).[11] The designed Fc-independent apoptosis induction may circumvent these mechanisms, resulting in a potential to target mAb-resistant diseases. Michel and Mattes have shown that the 1F5 mAb/CD20 complex becomes noninternalizing when the Fc region of the mAb is removed.[10] This observation further strengthens our point of view. Moreover, mAb therapies may "over-activate" the immune responses, which results in adverse side reactions, *e.g.*, hypersensitivity due to complement activation that requires discontinuation of treatment and administration of corticosteroids.[12] These side effects are sometimes fatal (*e.g.*, cytokine storm[13] and rituximab-associated lung injury[14,15]). In contrast, our direct apoptosis induction strategy does not rely on immune functions; this may ease such concerns. We have demonstrated that, at equivalent doses, the MORF1/MORF2 hybridization-mediated drug-free design possesses superior or comparable anti-lymphoma efficacies to type I anti-CD20 mAbs (see *Chapters 4* and *5*). These data suggest significant advantages of the drug-free therapeutics paradigm over conventional immunotherapies. Mechanistic studies to compare drug-free macromolecular therapeutics with Type II mAbs (*e.g.*, obinutuzumab), which may also induce direct apoptosis,[16,17] will provide further evaluation of the clinical potential.

Several previous platforms for CD20 crosslinking and apoptosis induction of B-cells have been developed.[18–24] One strategy is to construct multivalent mAbs or

polymer-mAb conjugates. For instance, multimeric rituximab bound to activated dextran[18] or lipid nanoparticles[19] have been synthesized. In *Chapter 2*, we describe multivalent HPMA copolymer – anti-CD20 Fab' conjugates, which successfully induced apoptosis of malignant B-cells *in vitro*. The advantage of such approaches[18–22] is the more straightforward one-step treatment, likely resulting in better patient compliance. However, due to the large size of the antibodies or their fragments, it is difficult to synthesize such constructs with high valency (due to steric hindrance). This undesirable feature may severely limit the therapeutic efficiency. We have attempted to increase the valency by synthesizing branched HPMA copolymer backbones.[20] A small amount of tetraethyleneglycol dimethacrylate was used as the crosslinker, and copolymers with high polydispersity were produced. Consequently, fractionation was required to prepare narrowly dispersed copolymers. Other researchers used biological polymers such as DNA[21] or polypeptides[22] as scaffolds to attach antibodies or the smaller size single-chain variable fragments (scFv). These polyvalent constructs indeed achieved better efficacies than their monovalent counterparts. However, one fundamental difference between these single-treatment designs and the "binary system" is that the binary systems have the advantage of performing pretargeting. Previously our laboratory has designed and developed a pilot "binary" anti-CD20 drug-free macromolecular therapeutic system using a pair of pentaheptad peptides (CCE and CCK) that formed antiparallel coiled-coil heterodimers as the biorecognition moieties.[23,24] When compared to this previous design using peptides, the MORF oligos clearly demonstrated faster binding kinetics as well as more efficient self-assembly (equimolar MORF1/MORF2 reached binding saturation *in vitro*), therefore resulting in superior apoptosis induction and *in vivo* anti-lymphoma

efficacy (see *Chapter 3, Table 3.1*). This is because the individual peptide sequences do not have a pronounced secondary structure at the physiological pH.[25] Fab'-CCE and P-CCK interact first *via* hydrophobic and electrostatic interactions, and then, the oligopeptides fold into a strong antiparallel coiled-coil heterodimer. Therefore, we aimed to identify a biorecognition pair that would bind efficiently at the 1:1 molar ratio. Morpholino oligonucleotides were selected due to their fast hybridization, excellent binding affinity and stability in plasma, as well as water-solubility.[26]

The results of our study warrant further clinical evaluation of the morpholino oligonucleotide mediated drug-free therapeutic system. The selection of the CD20 target in this system is validated by extensive prior clinical experience; anti-CD20 "B-cell depletion" therapy has been used in the clinic for over 15 years. Before translation to the clinic, potential toxicity and/or immunogenicity of the conjugates needs to be carefully studied. Note that, here, the preclinical evaluation was performed in SCID mice. It is important to follow up immunogenicity studies using immunocompetent animals. Properly designed *in vivo* toxicity experiments with dose escalation also need to be done. In addition, in the proposed system, Fab' from a mouse mAb (1F5) is used; therefore, in humans, these foreign, murine-derived protein fragments may trigger immune responses, *e.g.*, production of anti-mouse antibodies and the associated allergic or hypersensitivity reactions. In the future, such issues can be further addressed by producing the 1F5 mAb with humanized amino acid sequences or by directly switching to other humanized anti-CD20 mAbs (ofatumumab, veltuzumab, *etc.*).

In summary, drug-free macromolecular therapeutics constitute a new paradigm of polymer-based nanomedicines that are free of toxins and immune activation. Cell surface

biorecognition of hybrid nanomaterials translates into innate biological responses, *i.e.*, apoptosis. The apoptosis induction is direct (without the help of effector cells) and specific (targeted to certain receptors) and suitable for the design of precisely pretargeted nanotherapies. This novel approach has significant advantages over conventional chemo-, radio-, and immunotherapies. These promising perspectives warrant further developments within the same pipeline and may stimulate other designs. Here, we suggest potential future directions and provide supporting literature for each direction:

- *Targeting moieties*: peptide ligands identified by combinatorial methods,[27,28] oligosaccharides,[29,30] and oligonucleotide aptamers.[31,32] An aptamer for the B-cell receptor has been identified.[31] Bifunctional nucleic acids can be produced that contain aptamers (targeting moieties) and crosslinkers (binding motifs) on each end of one molecule.[32]
- *Binding motifs*: different sequences and lengths (*e.g.*, longer motifs with spacers may result in less steric hindrance of binding[33]), other types of binders such as peptide nucleic acids (PNA),[34,35] locked nucleic acids (LNA),[31,36] and 2'-*O*-methyloligoribonucleotides (2'-OMe-RNA).[36]
- *Polymer backbones (or other carriers)*: liposomes,[37] carbon nanotubes,[38] or genetically engineered biopolymers (*e.g.*, polypeptides,[22] poly-DNA[21]). Mobility and biodistribution of carriers should be characterized. Flexible backbones are generally preferred for receptor crosslinking.
- *Different diseases*: CD20 crosslinking and B-cell depletion can be used for autoimmune disorders such as rheumatoid arthritis,[39] multiple sclerosis,[40] and systemic lupus erythematosus.[41] The same approach can potentially be used for

antirejection treatment of organ transplants, *e.g.*, rituximab is used off-label for kidney transplant recipients.[42]

- *Cell receptors*: potentially any non- or slowly internalizing cell surface antigen can be a target, such as CD45 (T-cell, B-cell, macrophage),[43] death receptor 4 (breast and colon cancers, *etc.*),[44] prostate stem cell antigen (prostate cancer),[45] and carcinoembryonic antigen (many tumor types, but not on normal cells).[46,47] The crosslinking of these antigens can induce cell apoptosis.
- *Other directions*: crosslinking two different receptors simultaneously to achieve synergistic effects (*e.g.*, CD20/CD40,[48] CD20/FGFR3,[49] CD37/CD20 or CD37/CD19[37]), and designed as a switch for ON-OFF regulation of cellular events.[44,50]

For further translation into the clinic, the drug-free therapeutic approach will ultimately require validation and confirmation in properly conducted clinical trials, as well as carefully designed *in vivo* biocompatibility/toxicity studies. For applications in cancer, the tumor penetration capability of each of the therapy components shall be evaluated. It will be interesting to compare the mobility of the nanosized therapeutic conjugates with that of the immune effector cells, which have limited penetration into solid tumors. In conclusion, we anticipate more designs and research in this exciting new field of polymeric nanomedicines.

6.1 References

1. L. E. van der Kolk, *et al.*, CD20-induced B cell death can bypass mitochondria and caspase activation, *Leukemia*, 2002, **16**, 1735–1744.

2. P. Boross and J. H. W. Leusen, Mechanisms of action of CD20 antibodies, *Am. J. Cancer Res.*, 2012, **2**, 676–690.

3. M. Okroj, A. Österborg and A. M. Blom, Effector mechanisms of anti-CD20 monoclonal antibodies in B cell malignancies, *Cancer Treat. Rev.*, 2013, **39**, 632–639.

4. G. Cartron, *et al.*, Therapeutic activity of humanized anti-CD20 monoclonal antibody and polymorphism in IgG Fc receptor FcγRIIIa gene, *Blood*, 2002, **99**, 754–758.

5. M. R. Smith, Rituximab (monoclonal anti-CD20 antibody): mechanisms of action and resistance, *Oncogene*, 2003, **22**, 7359–7368.

6. A. Molina, A decade of rituximab: improving survival outcomes in non-Hodgkin's lymphoma, *Annu. Rev. Med.*, 2008, **59**, 237–250.

7. T. A. Davis, D. K. Czerwinski and R. Levy, Therapy of B-cell lymphoma with anti-CD20 antibodies can result in the loss of CD20 antigen expression, *Clin. Cancer Res.*, 1999, **5**, 611–615.

8. P.-C. Tsai, F. J. Hernandez-Ilizaliturri, N. Bangia, S. H. Olejniczak and M. S. Czuczman, Regulation of CD20 in rituximab-resistant cell lines and B-cell non-Hodgkin lymphoma, *Clin. Cancer Res.*, 2012, **18**, 1039–1050.

9. I. Dransfield, Inhibitory FcγRIIb and CD20 internalization, *Blood*, 2014, **123**, 606–607.

10. R. B. Michel and M. J. Mattes, Intracellular accumulation of the anti-CD20 antibody 1F5 in B-lymphoma cells, *Clin. Cancer Res.*, 2002, **8**, 2701–2713.

11. T. Pham, P. Mero and J. W. Booth, Dynamics of macrophage trogocytosis of rituximab-coated B cells, *PloS One*, 2011, **6**, e14498.

12. L. E. van der Kolk, A. J. Grillo-López, J. W. Baars, C. E. Hack and M. H. van Oers, Complement activation plays a key role in the side-effects of rituximab treatment, *Br. J. Haematol.*, 2001, **115**, 807–811.

13. R. Ponce, Adverse consequences of immunostimulation, *J. Immunotoxicol.*, 2008, **5**, 33–41.

14. L. C. Lands, New therapies, new concerns: rituximab-associated lung injury, *Pediatr. Nephrol.*, 2010, **25**, 1001–1003.

15. M.-C. Chaumais, *et al.*, Fatal pulmonary fibrosis after rituximab administration, *Pediatr. Nephrol.*, 2009, **24**, 1753–1755.

16. E. Mössner, *et al.*, Increasing the efficacy of CD20 antibody therapy through the engineering of a new type II anti-CD20 antibody with enhanced direct and immune effector cell–mediated B-cell cytotoxicity, *Blood*, 2010, **115**, 4393–4402.

17. S. Herter, *et al.*, Preclinical activity of the type II CD20 antibody GA101 (obinutuzumab) compared with rituximab and ofatumumab *in vitro* and in xenograft models, *Mol. Cancer Ther.*, 2013, **12**, 2031–2042.

18. N. Zhang, L. A. Khawli, P. Hu and A. L. Epstein, Generation of rituximab polymer may cause hyper-cross-linking–induced apoptosis in non-Hodgkin's lymphomas, *Clin. Cancer Res*., 2005, **11**, 5971–5980.

19. J. Popov, *et al*., Multivalent rituximab lipid nanoparticles as improved lymphoma therapies: indirect mechanisms of action and *in vivo* activity, *Nanomed*., 2011, **6**, 1575–1591.

20. R. N. Johnson, P. Kopečková and J. Kopeček, Synthesis and evaluation of multivalent branched HPMA copolymer–Fab' conjugates targeted to the B-cell antigen CD20, *Bioconjug. Chem*., 2009, **20**, 129–137.

21. Z. Zhang, *et al.*, DNA-scaffolded multivalent ligands to modulate cell function, *Chembiochem*, 2014, **15**, 1268–1273.

22. S. R. Aluri, *et al*., A hybrid protein-polymer nanoworm potentiates apoptosis better than a monoclonal antibody, *ACS Nano*, 2014, **8**, 2064–2076.

23. K. Wu, J. Liu, R. N. Johnson, J. Yang and J. Kopeček, Drug-free macromolecular therapeutics: induction of apoptosis by coiled-coil-mediated cross-linking of antigens on the cell surface, *Angew. Chem. Int. Ed*., 2010, **49**, 1451–1455.

24. K. Wu, J. Yang, J. Liu and J. Kopeček, Coiled-coil based drug-free macromolecular therapeutics: *in vivo* efficacy, *J. Control. Release*., 2012, **157**, 126–131.

25. J. Yang, C. Xu, C. Wang and J. Kopeček, Refolding hydrogels self-assembled from *N*-(2-hydroxypropyl)methacrylamide graft copolymers by antiparallel coiled-coil formation, *Biomacromolecules*, 2006, **7**, 1187–1195.

26. J. Summerton and D. Weller, Morpholino antisense oligomers: design, preparation, and properties, *Antisense Nucleic Acid Drug Dev*., 1997, **7**, 187–195.

27. H. Ding, W. M. Prodinger and J. Kopeček, Identification of CD21-binding peptides with phage display and investigation of binding properties of HPMA copolymer-peptide conjugates, *Bioconjug. Chem.*, 2006, **17**, 514–523.

28. H. Ding, W. M. Prodinger and J. Kopeček, Two-step fluorescence screening of CD21-binding peptides with one-bead one-compound library and investigation of binding properties of *N*-(2-hydroxypropyl)methacrylamide copolymer-peptide conjugates, *Biomacromolecules*, 2006, **7**, 3037–3046.

29. A. David, P. Kopečková, A. Rubinstein and J. Kopeček, Enhanced biorecognition and internalization of HPMA copolymers containing multiple or multivalent carbohydrate side-chains by human hepatocarcinoma cells, *Bioconjug. Chem.*, 2001, **12**, 890–899.

30. A. David, P. Kopečková, T. Minko, A. Rubinstein and J. Kopeček, Design of a multivalent galactoside ligand for selective targeting of HPMA copolymer-doxorubicin conjugates to human colon cancer cells, *Eur. J. Cancer*, 2004, **40**, 148–157.

31. P. R. Mallikaratchy, *et al.*, A multivalent DNA aptamer specific for the B-cell receptor on human lymphoma and leukemia, *Nucleic Acids Res.*, 2011, **39**, 2458–2469.

32. J. Zhou, B. Soontornworajit, M. P. Snipes and Y. Wang, Development of a novel pretargeting system with bifunctional nucleic acid molecules, *Biochem. Biophys. Res. Commun.*, 2009, **386**, 521–525.

33. Z. Peng, M. Sima, M. E. Salama, P. Kopečková and J. Kopeček, Spacer length impacts the efficacy of targeted docetaxel conjugates in prostate-specific membrane antigen expressing prostate cancer, *J. Drug Target.*, 2013, **21**, 968–980.

34. M. Rusckowski, T. Qu, F. Chang and D. J. Hnatowich, Pretargeting using peptide nucleic acid, *Cancer*, 1997, **80**, 2699–2705.

35. Y. Wang, *et al.*, Pretargeting with amplification using polymeric peptide nucleic acid, *Bioconjug. Chem.*, 2001, **12**, 807–816.

36. P. R. Mallikaratchy, *et al.*, A self-assembling short oligonucleotide duplex suitable for pretargeting, *Nucleic Acid Ther.*, 2013, **23**, 289–299.

37. B. Yu, *et al.*, Targeted drug delivery and cross-linking induced apoptosis with anti-CD37 based dual-ligand immunoliposomes in B chronic lymphocytic leukemia cells, *Biomaterials*, 2013, **34**, 6185–6193.

38. J. J. Mulvey, *et al.*, Self-assembly of carbon nanotubes and antibodies on tumours for targeted, amplified delivery, *Nat. Nanotechnol.*, 2013, **8**, 763–771.

39. Y. Yazici, Rheumatoid arthritis: when should we use rituximab to treat RA? *Nat. Rev. Rheumatol.*, 2011, **7**, 379–380.

40. S. L. Hauser, *et al.*, B-cell depletion with rituximab in relapsing-remitting multiple sclerosis, *N. Engl. J. Med.*, 2008, **358**, 676–688.

41. V. S.-F. Chan, H. H.-L. Tsang, R. C.-Y. Tam, L. Lu and C.-S. Lau, B-cell-targeted therapies in systemic lupus erythematosus, *Cell. Mol. Immunol.*, 2013, **10**, 133–142.

42. V. Ramanath, R. Nistala and K. Chaudhary, Update on the role of rituximab in kidney diseases and transplant, *Expert Opin. Biol. Ther.*, 2012, **12**, 223–233.

43. Y.-J. Huang, *et al.*, Multivalent structure of galectin-1-nanogold complex serves as potential therapeutics for rheumatoid arthritis by enhancing receptor clustering, *Eur. Cell. Mater.*, 2012, **23**, 170–181.

44. M. H. Cho, *et al.*, A magnetic switch for the control of cell death signalling in *in vitro* and *in vivo* systems, *Nat. Mater.*, 2012, **11**, 1038–1043.

45. Z. Gu, J. Yamashiro, E. Kono and R. E. Reiter, Anti-prostate stem cell antigen monoclonal antibody 1G8 induces cell death *in vitro* and inhibits tumor growth *in vivo via* a Fc-independent mechanism, *Cancer Res.*, 2005, **65**, 9495–9500.

46. T. Wirth, E. Soeth, F. Czubayko and H. Juhl, Inhibition of endogenous carcinoembryonic antigen (CEA) increases the apoptotic rate of colon cancer cells and inhibits metastatic tumor growth, *Clin. Exp. Metastasis*, 2002, **19**, 155–160.

47. L. Santoro, *et al.*, Noninternalizing monoclonal antibodies are suitable candidates for ^{125}I radioimmunotherapy of small-volume peritoneal carcinomatosis, *J. Nucl. Med.*, 2009, **50**, 2033–2041.

48. L. Al-Zoobi, *et al.*, Enhancement of Rituximab-induced cell death by the physical association of CD20 with CD40 molecules on the cell surface, *Int. Immunol.*, 2014, **26**, 451–465.

49. N. Kotani, Y. Ishiura, R. Yamashita, T. Ohnishi and K. Honke, Fibroblast growth factor receptor 3 (FGFR3) associated with the CD20 antigen regulates the rituximab-induced proliferation inhibition in B-cell lymphoma cells, *J. Biol. Chem.*, 2012, **287**, 37109–37118.

50. M. Karlsson, *et al.*, Pharmacologically controlled protein switch for ON-OFF regulation of growth factor activity, *Sci. Rep.*, 2013, **3**, 2716.